

*Handwritten notes:*  
1/11  
Nov 3 1996

**FINAL REPORT**

**NASA GRANT NAG5 - 1049**

**August 1993 - December 1996**

**Submitted by**

**Raj C. Yalamanchili**

**February 1997**

**DEPARTMENT OF ELECTRICAL ENGINEERING  
SCHOOL OF ENGINEERING  
HOWARD UNIVERSITY  
WASHINGTON, D.C.**



## **TABLE OF CONTENTS**

**I. Introduction**

**II. List of Master's Theses**

**III. Headings and Abstracts of the Master's Theses**

**IV. List of Publication**

**V. Copies of Published Papers**

**VI. Copy of Technical Paper Presented in Brazil**



## I. INTRODUCTION

This Final Report covers the period from August 1993 to December 1996.

During this time three Master's degrees were awarded to the students who were supported by the NASA Grant. A fourth student who was supported partially by this Grant will be submitting his Master's Thesis by April 1997.

A visiting Professor from China was awarded a Post Doctoral Fellowship under this Grant for two years. One of the Master's degree holders has completed all course requirements for his Ph.D. and is working toward his Dissertation. This dissertation is expected to be submitted to the Graduate School at Howard University by March 1998. This student was also given financial help under this Grant.

Five papers were sent for publication. One of these was published in the IEEE - MTT's Proceedings and three were published in the International Journal of Electronics. The fifth one was sent to reviewers for evaluation.

The lists of Master's Theses, their headings and their Abstracts are given in the following pages. Also are given the lists of Publications and their copies.



## **II. List of Master's Theses**

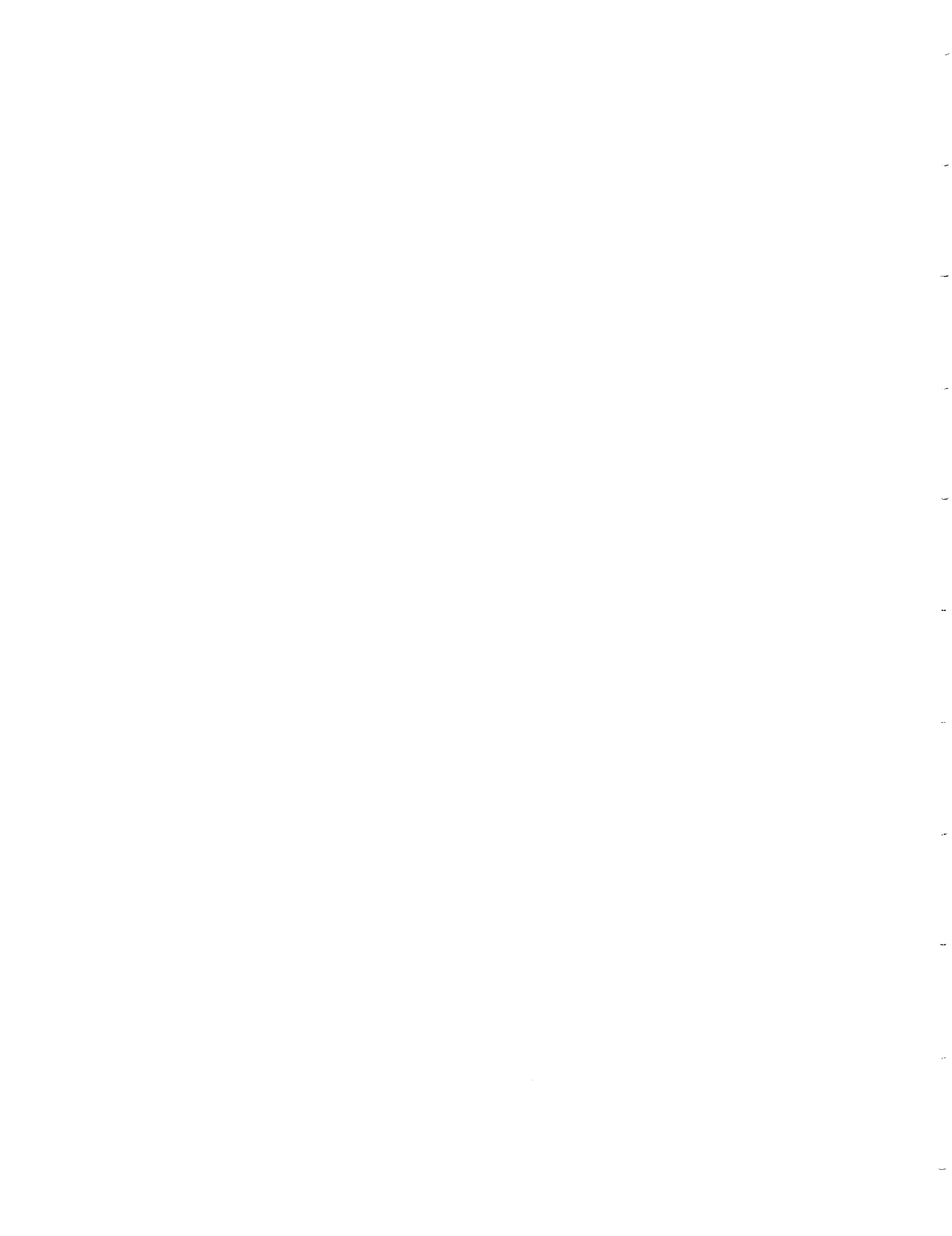
1. "Coupling single-mode fiber to uniform an dtapered thin-film Waveguide"  
Gadi Jagannath, December 1994.
2. "A weakly guiding approximation for the propagation characteristic of single and double-clad optical fibers".  
Trevor Correia, August 1994.
3. "Rectangular patch microstrip antenna - analysis and design"  
James Wesley Hall, July 1994.

A fourth Master's Thesis will be submitted in April 1997.

A Ph.D. Dissertation will be submitted in March 1998.



**III. Headings and copies of abstracts of the Master's theses.**



HOWARD UNIVERSITY

Coupling Single-mode Fiber to Uniform  
and Tapered Thin-film waveguide.

\*

A Thesis Submitted to the Faculty of the  
Graduate School of Arts and Sciences

of

HOWARD UNIVERSITY

in partial fulfillment of the requirement for the degree of

Master of Engineering

by

Jagannath V. Gadi

Washington, D.C.  
December, 1994.

## ABSTRACT

Theoretical derivations, computer analysis and test data are provided to demonstrate that the cavity model is a feasible one to analyze thin-substrate, rectangular-patch microstrip antennas. Seven separate antennas were tested .

Most of the antennas were designed to resonate at L-band frequencies (1-2 GHz). One antenna was designed to resonate at an S-band (2-4 GHz) frequency of 2.025 GHz. All dielectric substrates were made of Duroid, and were of varying thicknesses and relative dielectric constant values.

Theoretical derivations to calculate radiated free space electromagnetic fields and antenna input impedance were performed. MATHEMATICA 2.2 software was used to generate Smith Chart input impedance plots, normalized relative power radiation plots and to perform other numerical manipulations. Network Analyzer tests were used to verify the data from the computer programming (such as input impedance and VSWR) . Finally, tests were performed in an anechoic chamber to measure receive-mode polar power patterns in the E and H planes.

Agreement between computer analysis and test data is presented . The antenna with the thickest substrate ( $\epsilon_r = 2.33$  , 62 mils thick) showed the worst match to theoretical impedance data. This is anticipated due to the fact that the cavity model generally loses accuracy when the dielectric substrate thickness exceeds 5% of the antenna's free space wavelength [ 1, 2 , 3] . A method of reducing computer execution time for impedance calculations is also presented.

HOWARD UNIVERSITY

A WEAKLY GUIDING APPROXIMATION FOR THE  
PROPAGATION CHARACTERISTICS OF  
SINGLE AND DOUBLE-CLAD OPTICAL FIBERS

\*

A Thesis  
Submitted to the Faculty of the  
Graduate School of Arts and Sciences

of

HOWARD UNIVERSITY

in partial fulfillment of  
the requirements for the  
degree of

MASTER OF ENGINEERING

Department of Electrical Engineering

by

Trevor C. Correia

\*

Washington, D. C.  
August 1994

## ABSTRACT

Recent advances in optical fiber technology have made it possible to develop optical communication systems with very large bandwidths and very low loss. Optical systems are routinely tested and installed with repeaterless spacings of several hundred kilometers, a fact that attests to the very low loss inherent to the transmission media. Although there is a manufacturing capability for producing high performance optical fibers, there is no concise method of accurately predicting their propagation characteristics. For the simplest form of fiber, the standard single-clad step-index profile, relatively simple analytical procedures give accurate results. However, for the high performance modified structures, exact analytical solutions do not exist so their analysis relies on approximate solutions. Because of the rigors associated with accurately analyzing optical fibers with modified characteristics, new mathematical procedures are constantly being developed to simplify the analysis, and, when all else fails, the procedures turn to empirical methods.

In this Thesis, an approximation method, known as the weakly guiding approximation, is utilized to find the propagation characteristics of single and double-clad optical fibers. Using a combination of numerical and graphical solutions, data are provided to compare the results from this method with those achieved by other methods. It is shown here that, without the complexities associated with other procedures, this method gives fairly accurate results.

HOWARD UNIVERSITY

RECTANGULAR-PATCH MICROSTRIP  
ANTENNA ANALYSIS AND DESIGN

\*

A Thesis  
Submitted to the Faculty of the  
Graduate School of Arts and Sciences

of

HOWARD UNIVERSITY

in partial fulfillment of  
the requirements for the  
degree of

MASTER OF ENGINEERING

Department of Electrical Engineering

by

James Wesley Hall

\*

Washington, D.C.  
August 1994

## ABSTRACT

Theoretical derivations, computer analysis and test data are provided to demonstrate that the cavity model is a feasible one to analyze thin-substrate, rectangular-patch microstrip antennas. Seven separate antennas were tested .

Most of the antennas were designed to resonate at L-band frequencies (1-2 GHz). One antenna was designed to resonate at an S-band (2-4 GHz) frequency of 2.025 GHz. All dielectric substrates were made of Duroid, and were of varying thicknesses and relative dielectric constant values.

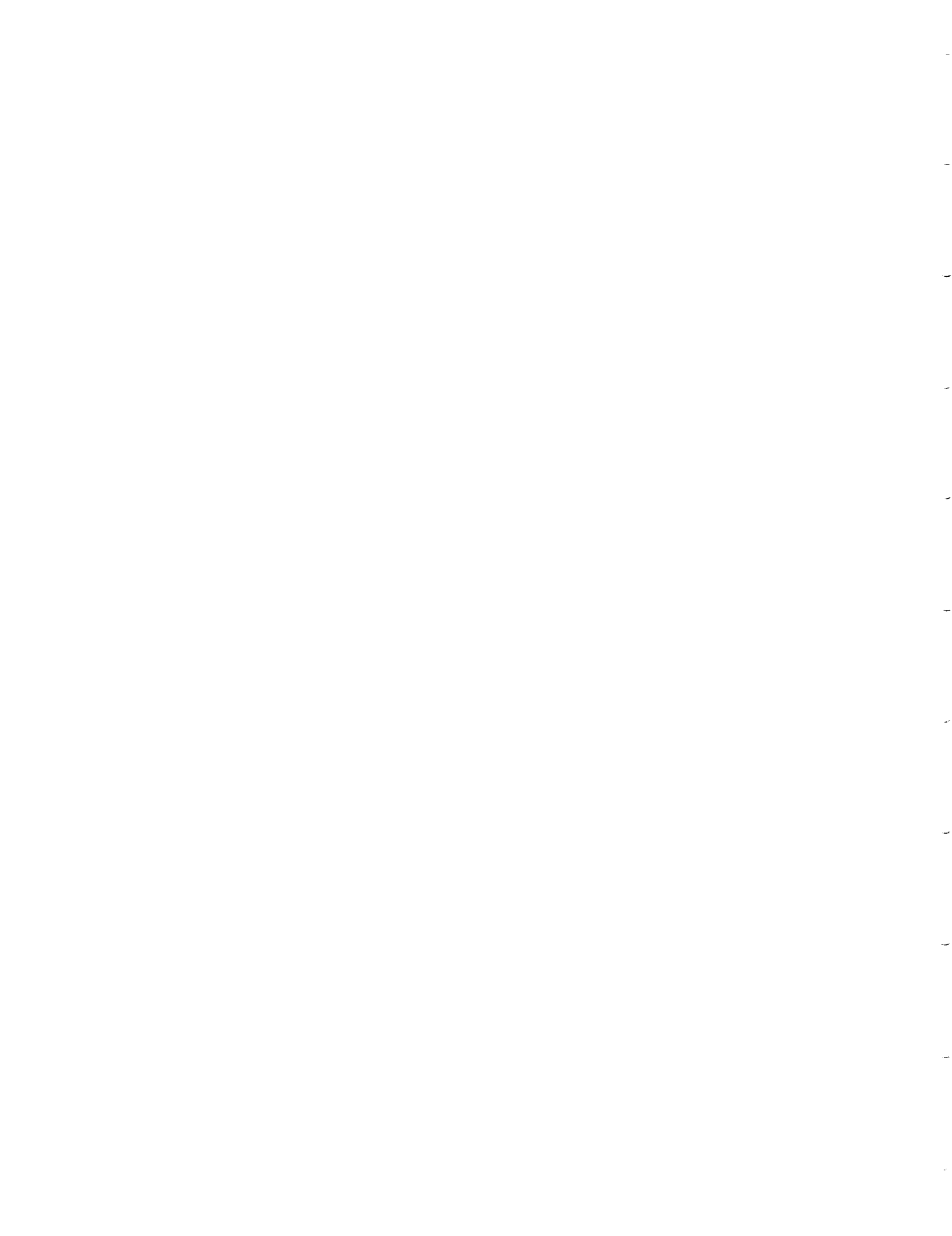
Theoretical derivations to calculate radiated free space electromagnetic fields and antenna input impedance were performed. MATHEMATICA 2.2 software was used to generate Smith Chart input impedance plots, normalized relative power radiation plots and to perform other numerical manipulations. Network Analyzer tests were used to verify the data from the computer programming (such as input impedance and VSWR) . Finally, tests were performed in an anechoic chamber to measure receive-mode polar power patterns in the E and H planes.

Agreement between computer analysis and test data is presented . The antenna with the thickest substrate ( $\epsilon_r = 2.33$  , 62 mils thick) showed the worst match to theoretical impedance data. This is anticipated due to the fact that the cavity model generally loses accuracy when the dielectric substrate thickness exceeds 5% of the antenna's free space wavelength [ 1, 2 , 3] . A method of reducing computer execution time for impedance calculations is also presented.

#### **IV. List of Publications**

1. "Coupling Single-Mode Fiber to Uniform and Symmetrically Tapered Thin-Film Waveguide Structures using Gadolinium Gallium Garnet". Gadi, Yalamanchili and Shahid, SBMO/ IEEE MTT-s 1995 Proceedings, pp 926-931.
2. "Rectangular Waveguides With Two Conventional and Two Superconducting Walls". Yalamanchili, Qiu and Wang. International Journal of Electronics, 1995.
3. "Scattering by the Transition Junction Between Conventional and a High-Temperature Superconducting Waveguide". Yalamanchili, Qiu and Wang. International Journal of Electronics, Vol. 76, No. 6, pp 1173 - 1180, 1994.
4. "Meissner Model of Superconducting Rectangular Waveguides". Wang, Qiu and Yalamanchili. International Journal of Electronics, Vol. 76, No. 6, pp 1151 - 1171, 1994.
- \*5. "Single Index Summation Procedure for Calculating Antenna Input Impedance". Yalamanchili and Hall. 1996.

\* This paper has been sent to reviewers for evaluation.



## **V. Copies of Published Papers**



# COUPLING SINGLE-MODE FIBER TO UNIFORM AND SYMMETRICALLY TAPERED THIN-FILM WAVEGUIDE STRUCTURES USING GADOLINIUM GALLIUM GARNET

Jagannath Gadi, Raj Yalamanchili and Mohammad Shahid  
Howard University  
Department of Electrical Engineering  
2300, 6 th Street, N.W  
Washington, DC 20059

## Abstract

The need for high efficiency components has grown significantly due to the expanding role of fiber optic communications for various applications. Integrated optics is in a state of metamorphosis and there are many problems awaiting solutions. One of the main problems being the lack of a simple and efficient method of coupling single-mode fibers to thin-film devices for integrated optics. In this paper, optical coupling between a single-mode fiber and a uniform and tapered thin-film waveguide is theoretically modeled and analyzed. A novel tapered structure presented in this paper is shown to produce perfect match for power transfer.

## 1. INTRODUCTION

Integrated Optics has come a long way since early 1970's. It is poised at the threshold of making a big impact in everyday world. Integrated optics has drawn into several disciplines, such as computers and microwave integrated circuit technology resulting in new fabrication technologies. The field is now in a state of flux and there are still many problems awaiting solutions. One of the main problems being the lack of a simple and efficient method of coupling optical fiber to thin-film devices for integrated optics. Although a number of connectors are available in the market, the efficiency and reproducibility are low. In this paper, a novel uniform and symmetrically tapered structure are analyzed mathematically and the results presented.

There are certain papers published by researchers in the area of thin-film couplers that are worthy of note, in that they provide the background for the development of the proposed work and point towards issues raised by shortcomings of the previous work. Louisell [1] investigated broadband bi-directional couplers in which he showed that the phase constants and coupling coefficients vary with distance along two coupled transmission lines. Ulrich [2] has shown by analysis how light can be coupled into a thin-film by means of a prism-film coupler. Akira Ihaya [3] presented a mathematical model of a thin-film optical directional coupler consisting of a three-layered deposited glass films on the substrate, with coupling occurring between the first and the third film. Wilson and Teh[4] have shown a mathematical modeling of a tapered velocity directional coupler. Nelson [5] has theoretically

examined the coupling of single-mode optical waveguides through the use of expanding and contracting tapers. Juichi Noda et al.[6] have shown a connection between single mode fiber coupler to a Ti diffused LiNo<sub>3</sub> strip waveguide. The authors Y.Cai et al.[7]., have analyzed the coupling characteristics of a uniform structure.

## 2. THEORETICAL BACKGROUND

In this paper, we present a novel method of coupling light from a single mode fiber to two structures : Uniform and symmetrically tapered thin-film couplers. The model presented is an improved version of the uniform five layered structure presented by Y. Cai et al [7]. If a fiber is directly connected to the thin-film, as shown by Y.Cai et al [7]., it leads to a large mismatch of the field profiles at the interface and as a result, leads to loss of optical power. To overcome this optical reflection and radiation losses, they proposed a five layered structure which is shown in Figure 1. This consists of a coupling waveguide, buffer layers, thin-film layer and the substrate. To avoid mismatch of the fiber core and the coupling waveguide field profiles at the interface, the coupling waveguide dimensions are designed as 2aX2a, where 'a' is the radius of the fiber core. Guttman et al[8]., have shown that the field distributions of the fundamental mode of the cylindrical fiber core and the garnet material waveguide differ slightly if the refractive index differences are smaller. Solgel solution is used at the interface such that any slight refractive index mismatch between the fiber core and the coupling waveguide is minimized. The buffer layer serves the purpose of coupling optical power to the thin-film waveguide of lower refractive index. Gadolinium Gallium Garnet material was used as the thin-film material because of the properties exhibited by the material. The buffer layers and the coupling waveguide are silica doped materials. The required refractive index of buffer and coupling waveguides is obtained by doping TiO<sub>2</sub> with SiO<sub>2</sub>.

The eigen mode equations of the five layered structure developed ( Figure 1 ) can be obtained by solving with  $w=g=2a$ , where :  $w$ = the height of the coupling waveguide,  $a$ = radius of the fiber core,  $n_g$ =refractive index of the coupling waveguide ( Garnet material ),  $n_b$ =refractive index of the buffer layer,  $n_w$  = refractive index of the thin-film material,  $\lambda$ =wavelength of the wave ( 1.3 $\mu$ m ) and  $W$ = height of the thin-film coupling waveguide. The eigenmode equations developed by Y.Cai et al[9].are :

$$Q_a = n_a^2 K_{gx} \tan(K_{gx} \cdot W / 2) \quad \text{--- (1)}$$

$$Q_a = \sqrt{(2\pi / \lambda)^2 (n_g^2 - n_a^2) - K_{gx}^2} \quad \text{--- (2)}$$

$$Q_t = \frac{K_{gx} \{-1 + \sqrt{\tan^2(g \cdot K_{gx}) + 1}\}}{\tan(g K_{gx})} \quad \text{--- (3)}$$

$$Q_t = \sqrt{(2\pi / \lambda)^2 (n_w^2 - n_a^2) - K_{gx}^2} \quad \text{--- (4)}$$

The parameters  $k_{gx}$ ,  $Q_x$  and  $k_{gy}$ ,  $Q_y$  are the x and y components of the wavenumbers.  $K_{gx}$  and  $K_{gy}$  represent the sinusoidal variation in the x and y directions. The propagation constant of the coupling waveguide can be determined by solving equations ( 1 to 4 ).

$$\beta_{gg}^2 = \omega^2 \mu_o \epsilon_o n_{gg}^2 - K_{gx}^2 - K_{gy}^2 \quad \text{---- ( 5 )}$$

The propagation constant  $\beta_w$  of the thin-film waveguide is obtained by replacing  $n_{gg}$  with  $n_w$ ,  $w$  with  $W1$  and  $\beta_{gg}$  with  $\beta_w$  in equations( 1to5 ). The value of  $W1$  for the thin-film is so chosen such that highest power coupling occurs between the coupling waveguide and the thin-film at this value. The optimum value  $W1$  is chosen such that  $\beta_{gx} = \beta_w$  for no mismatch. The thickness of the buffer layer has a direct bearing on the power coupled from the coupling waveguide to the thin-film waveguide and an optimum value is chosen such that there is a maximum power transfer from the coupling waveguide to the thin-film waveguide. The propagation constant of the thin-film varies because of the change in value of  $w$  along the  $z$  direction. Therefore the mismatch,  $M$  depends

$$\text{on the propagation constant difference given by } M(z) = \frac{\beta_{gg} - \beta_w(z)}{2C} \quad \text{---- ( 6 )}$$

and the maximum fraction of power transferred between the coupling waveguide and the thin-film waveguide with a fixed mismatch  $M$ , is given by  $F^2 = ( 1 + M^2 )^{-1}$  ---- ( 7 )

Application of the theory developed by Snyder et al[10] and Snyder [11], to the model analyzed in Figure 1, gives the power coupled into the thin-film for a uniform coupler as

$$P' = P F^2 \text{Sin}^2 \int_0^z (C / F) dz \quad \text{---- ( 8 )}$$

where  $P$  is the total power introduced,  $C$  the coupling coefficient between the center of the coupling waveguide and the center of the thin-film waveguide. In this paper, we present a novel uniform and symmetrically tapered structure ( Figure 2 ) where the modes of a uniform waveguide form a complete set and can propagate independently from one another, while the tapered modes are coupled together and adjust their characteristics to suit the varying transverse properties of the guiding structure as they are moving along the taper. During the process of coupling the light from the uniform coupling waveguide to the thin-film waveguide, the wave is kept in the lowest order mode. For the shape shown in this paper.( Winn and Harris [12]),the power coupled at the

$$\text{narrow end is given by } P_o = P' ( 1 - F^2 \text{Sin}^2 \int_0^z (C / F) dz ) \quad \text{---- ( 9 )}$$

In this paper while analyzing the theoretical model of the uniform and tapered coupler we made the assumption that the materials used are lossless and therefore there are no Fresnel's reflections at the interfaces and that there are no lossess at the interface of the fiber core and the coupling waveguide.

### 3. RESULTS AND DISCUSSION

The material used for the analysis of uniform and tapered couplers is Gadolinium Gallium Garnet (GGG). The coupling waveguide material used is GGG. Buffer layer material is spun silica which is doped with TiO<sub>2</sub>. Thin-film material is polymerized solgel solution of SiO<sub>2</sub> and TiO<sub>2</sub>. The refractive index of coupling waveguide,  $n_{wg} = 1.9389$  @  $\lambda = 1.3\mu\text{m}$ . The refractive index of the buffer layers is chosen, as  $n_b = 1.9340$  and the refractive index of the thin-film material,  $n_w = 1.9450$ . Figure 3 shows the plot of C versus d, where C is the coupling coefficient and d is the distance from the center of the coupling waveguide to the center of the thin-film. This equation given by Snyder [11], is

$$C = \left( \frac{V\Delta}{2\pi} \right)^{1/2} \frac{d}{\rho^2} \exp \left\{ \frac{-Vd^2}{4\rho^2} \right\} \quad \text{--- (10)}$$

The refractive index of GGG versus wavelength is shown in Figure 4. The expression used to calculate the

$$\text{refractive index is } n^2 - 1 = \sum_{i=1}^3 \frac{A_i \lambda^2}{(\lambda^2 - L_i^2)} \quad \text{--- (11)}$$

where  $A_i$  and  $L_i$  are the sellmeier coefficients, given by Wood and Nassau [13].

By solving the equations (1to5) with  $w=2a=g$ , the propagation constant  $\beta_{wg} = 9.3253804 \mu\text{m}^{-1}$  was obtained.

Figure 5 shows the propagation constant for the thin-film as a function of the film thickness  $W1$ . The propagation constant of the thin-film equals the propagation constant of the coupling waveguide when the thickness  $W1=0.886\mu\text{m}$ . The maximum coupling power is attained at  $\beta_{wg} = \beta_w = 9.3253804 \mu\text{m}^{-1}$ . Figure 6 shows the plot of coupled power versus the propagation distance for the uniform coupler of different d's for perfectly matching constants  $\beta_{wg} = \beta_w$  at thickness of thin-film  $w=0.886 \mu\text{m}$ . Figure 7 shows the power coupled for uniform and tapered couplers with respect to the distance z and the taper starts at length  $L1= 700\mu\text{m}$ , with slopes (K) of the symmetrical taper at 0.0001, 0.00009 and 0.00002. Figure 8 shows the effect of the thickness of the thin-film and the role played by the taper in the power output.

### 4. CONCLUSION

The novel structure (Figure 2) exhibits broad-bandwidth coupling characteristics and it is easy to manufacture since it does not put serious constraints on the accuracy of the coupling length of the coupler. The taper has the distinctive advantage of confining the power within the taper such that the output stays approximately near the value of the power introduced at the start of the taper. The outstanding feature of the taper is the higher efficiency as compared to the more conventional devices.

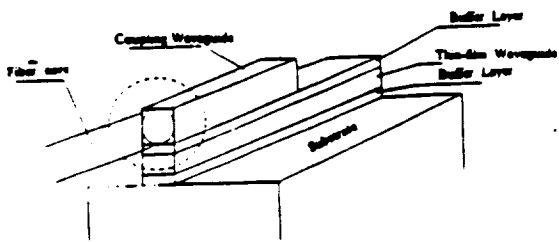


Figure 1. Schematic diagram of Single-mode fiber to thin-film waveguide using a coupling waveguide

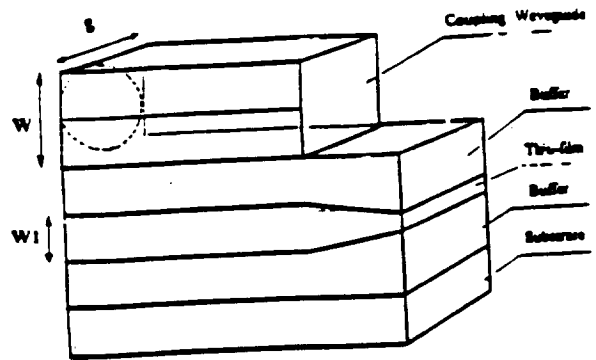


Figure 2. Schematic diagram of the proposed novel tapered structure.

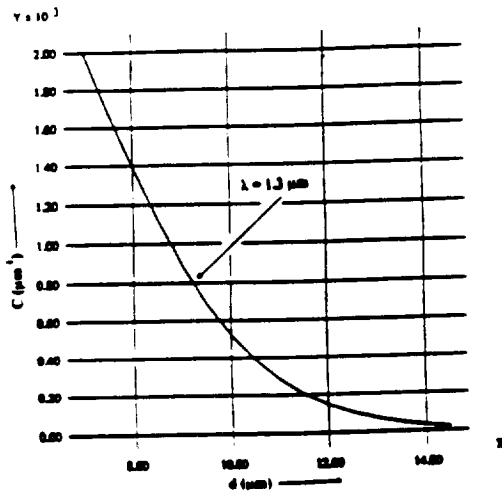


Figure 3. Coupling coefficient versus separation distance between center of coupling waveguide to center of thin-film waveguide.

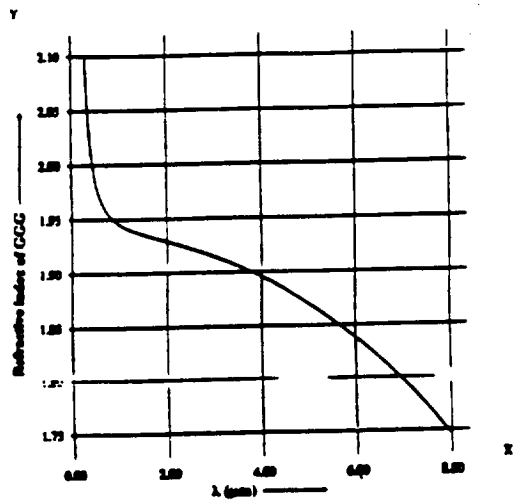


Figure 4. Refractive index of gallium garnet as a function of wavelength.

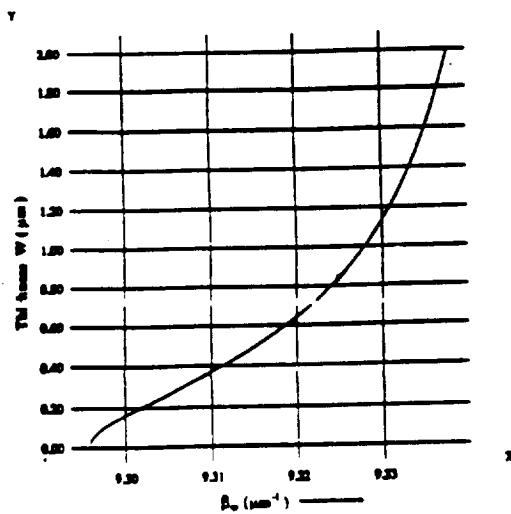


Figure 5. Propagation constants versus thickness of thin-film.

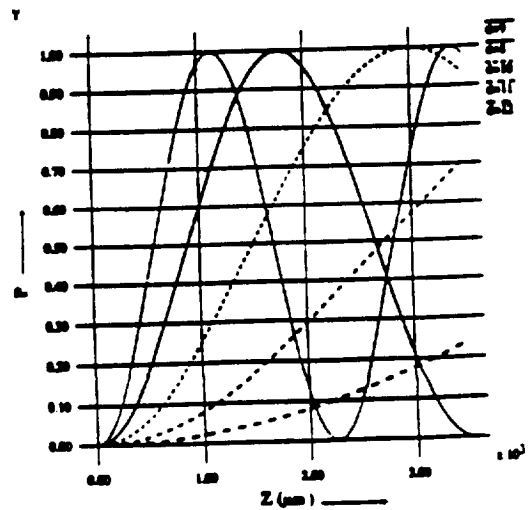


Figure 6. Plot of power coupled into thin-film versus length for various values of d.

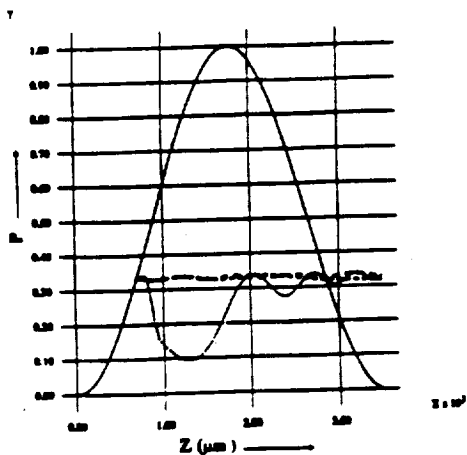


Figure 7. Comparison of uniform power and tapered power coupled into thin-film with taper at  $L_1=700 \mu\text{m}$  for different cases of  $K$  for a thin-film thickness of  $W_1=0.886 \mu\text{m}$ .

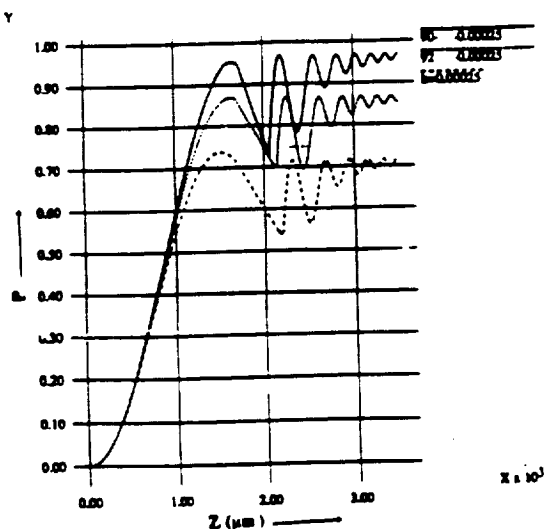


Figure 8. Plot of coupled power versus propagation distance for a taper structure with  $L_1=1700 \mu\text{m}$  and a slope  $K=0.00025$  for different thickness of thin-film.

## 5. REFERENCES

- [1]. W.H.Louisell, "Analysis of the single tapered mode coupler." The Bell system Technical Journal, pp 853-870, July 1955.
- [2]. R.Ulrich, "Theory of the prism-film coupler by plane-wave analysis", Journal of the Optical Society of America, Vol.60, No.10, pp 1337 - 1350, October 1970.
- [3]. Akira Ihaya, Hirosuka Furuta, Hideki Noda, "Thin-film optical directional coupler," Proceedings of the IEEE, pp 470-471, April 1972.
- [4]. Michael G.F.Wilson and G.A. Teh, "Tapered optical directional coupler," IEEE transactions on microwave theory and Techniques, Vol. MTT-23, No.1, pp 85-92, January 1975.
- [5]. A.R. Nelson, "Coupling Optical Waveguides by tapers", Applied Optics, Vol.14, No 12, December 1975.
- [6]. Juichi Noda, Osamu Mikami, Makoto Minaketa, and Masaharu Fukuma, "Single-mode optical-waveguide fiber coupler," Applied optics, Vol.17, No.13, pp 2092-2096, July 1978.
- [7]. Yuanmin Cai, Tetsuya Mizumoto, and Yoshiyuki Naito, "An Effective method for coupling Single-mode fiber to Thin-film Waveguide," Vol.9, No.5, May 1991.
- [8]. J.Guttman, O.Krumpholz and E. Pfeiffer, "Optical Fiber-Stripline-Coupler", Applied Optics, Vol.14, No.5, pp 1225-1227, May 1975.
- [9]. Yuanmin Cai, Tetsuya Mizumoto, and Yoshiyuki Naito, "Analysis of the coupling waveguide system," Journal of Lightwave technology, Vol.8, No.1, pp 90 - 98, January 1990.
- [10]. A.W.Snyder and A. Ankiewicz, "Fiber couplers composed of unequal cores," Electronics letters, Vol.22, No.23, pp 1237-1238, November 1986.
- [11]. Snyder and Love, "Optical Waveguide Theory", Chapman, New York, 1988.
- [12]. Robert K. Winn and Jay H. Harris, "Coupling from multimode to single-mode linear waveguides using Horn-shaped structures," IEEE Transactions on Microwave Theory and Techniques, Vol. MTT-23, No.1, January 1975.
- [13]. Darwin L.Wood and Kurt Nassau, "Optical properties of Gadolinium Gallium Garnet", Applied Optics, Vol. 29, No.5, September 1990.

## Rectangular waveguides with two conventional and two superconducting walls

RAJ YALAMANCHILI†, ZHENG AN QUI† and  
YEN-CHU WANG†

The propagation properties of  $TE^{pm}$  modes and their dispersion relations in rectangular waveguides with two conventional and two superconducting walls, derived by using the Meissner boundary conditions on the superconducting walls, are presented. In addition to recovering some previously known results, some novel results have been obtained: the cut-off wavelength of the dominant  $TE^{10}$  mode is greater than that of the conventional  $TE_{10}$  mode, and the tangential electric field and normal magnetic field for the dominant mode  $TE^{10}$  exist on the superconducting surfaces. Expressions for electromagnetic components, surface currents, attenuation coefficient, maximum transmitted power, dispersion and wave impedance are also presented.

### 1. Introduction

Over several years there has been considerable progress in the development of superconducting devices in the microwave and millimetre wave bands, for example, low- and high-temperature superconducting microwave filters, resonators, antennas, phase shifters, etc. Many superconducting electronic devices have been sought at liquid nitrogen temperatures (Nisenoff 1988, Van Duzer and Tuner 1981). The discovery of high- $T_c$  superconductors (HTS) has fundamentally changed the prospects of superconductive electronics. The low surface resistance of superconducting materials makes possible microwave devices and circuits with very high  $Q$ , low insert loss and dispersion. Superconducting waveguides have been studied as low  $T_c$  superconductors ( $< 18$  K) (Alaux and Wybouw 1976, Rohner 1978, Zepp *et al.* 1977, Fabre *et al.* 1981). Experimental and theoretical results have shown that HTS waveguides and transmission lines exhibit significantly better performance than that of their identical metallic counterparts (Wang *et al.* 1994, Yalamanchili *et al.* 1992).

The propagation properties of transverse electric (TE) modes in high- $T_c$  ( $T_c > 30$  K) superconductor rectangular waveguides have recently been studied using HTS electromagnetic theory and Meissner boundary conditions which are consistent with the two-fluid model (Wang *et al.* 1994). The new boundary conditions give rise to different field solutions, hence new waveguide characteristics. This paper describes the propagation properties of TE modes in rectangular waveguides with two conventional and two superconducting walls (WGCSW) based on the theory established by Wang *et al.* (1994). This kind of waveguide has different characteristics from either HTS waveguides or conventional waveguides. The attenuation and dispersion are smaller than that of conventional waveguides. The dominant mode in the WGCSW is the  $TE^{10}$  mode, which is the same as conventional waveguides. An interesting property is that the cut-off wavelength of the dominant mode is greater

---

Received 18 June 1994; accepted 27 October 1994.

†Department of Electrical Engineering, Howard University, Washington, DC 20059, U.S.A.

than that of conventional waveguides. Therefore, it is easier to excite the dominant mode in the WGCSW. Since the WGCSW has two conventional broad walls and two superconducting walls (two simply-connected superconductors), it is easier to fabricate than a four-wall superconducting waveguide.

In section 2, the most important dispersion relation of WGCSW is derived along the  $x$ -direction from the wave equation and the Meissner boundary conditions on two walls ( $x=0$ ,  $x=a$ ). Expressions for electromagnetic field components and surface currents, including the surface superconducting current  $J_{\parallel}$  and the surface normal current  $J_{\perp}$ , based on two-fluid theory are given. Various parameters of the WGCSW are analysed and compared with conventional waveguides.

## 2. Theory

### 2.1. Wave equation and numerical solutions of cut-off wavelength

This section analyses a WGCSW with two narrow superconducting walls ( $x=0$  and  $x=a$ ) and two broad perfect or good conductor walls ( $y=0$  and  $y=b$ ), as shown in Fig. 1. A rigorous formulation based on Maxwell's equations and Meissner boundary conditions is used to obtain the new electromagnetic field properties in the WGCSW.

The governing wave equation (Helmholtz equation) and the Meissner boundary conditions for the longitudinal magnetic field  $H_z$  of the TE mode in an air-filled WGCSW are:

$$\nabla_{\perp}^2 H_z + k_c^2 H_z = 0 \quad (1)$$

$$\frac{\partial H_z}{\partial n} - \frac{1}{\lambda_L} H_z = 0 \quad \text{at } x=0, x=a \quad (2a)$$

$$\frac{\partial H_z}{\partial n} = 0 \quad \text{at } y=0, y=b \quad (2b)$$

where the operator  $\nabla_{\perp}^2$  is the Laplacian operator in the transverse plane (i.e.  $xy$ -plane). Propagation in the  $z$ -direction is assumed. The parameters  $a$  and  $b$  are the

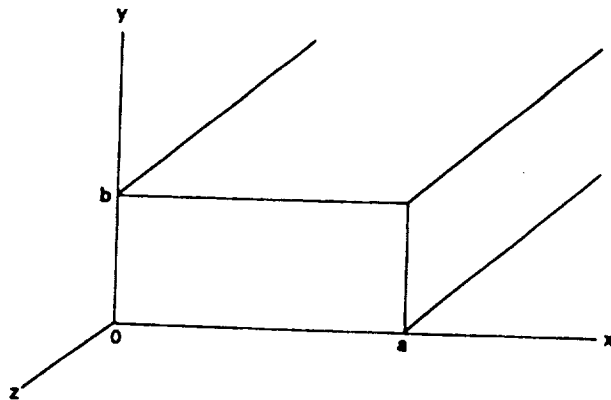


Figure 1. WGCSW with two narrow superconducting walls ( $x=0$ ,  $x=a$ ) and two broad perfect or good conductor walls ( $y=0$ ,  $y=b$ ).

width and height of the WGCSW, respectively,  $k_c$  is the cut-off wavenumber, and  $\lambda_L$  is London penetration depth is for HTS this value varies from  $10^{-8}$  m to  $10^{-7}$  m (Burns 1992). Equation (2a) is the Meissner boundary condition; (2b) is the boundary condition for the conventional wall. The important Meissner effect is that the fields do not vanish abruptly from the surface of a bulk superconductor, rather, they decay exponentially into the bulk. The penetration depth  $\lambda_L$  is the characteristic decay length of the magnetic field into a superconductor. It is obvious that when  $\lambda_L \rightarrow \infty$ , the second term of the Meissner boundary condition approaches zero, (2a) reduces to the boundary condition  $(\partial H_z / \partial n) = 0$  for the conventional waveguide. Therefore, the first term of (2a) is related to the properties of the WGCSW. Thus, the Meissner boundary conditions are relevant to the two-fluid superconducting model.

It is assumed that the general solution of the governing equation is

$$H_z = (C_1 \sin k_x x + C_2 \sin k_x x) \cos k_y y \quad (3)$$

where  $C_1$  and  $C_2$  are unknown coefficients; both cannot be equal to zero at the same time;  $k_x$  and  $k_y$  are the known wavenumbers along the  $x$  and  $y$  axes, respectively.

Substituting (3) into (2a) and (2b) obtains two sets of equations for  $k_x$  and  $k_y$ :

$$\left( k_x \sin k_x a - \frac{\cos k_x a}{\lambda_L} \right) C_1 - \left( k_x \cos k_x a + \frac{\sin k_x a}{\lambda_L} \right) C_2 = 0 \quad (4a)$$

$$\frac{1}{\lambda_L} C_1 - k_x C_2 = 0 \quad (4b)$$

and

$$k_y = \frac{m\pi}{b}, \quad m = 0, 1, 2, 3, \dots \quad (5)$$

For non-trivial solution conditions, the determinant of the coefficient matrix of (4a) and (4b) has to be equal to zero:

$$\begin{vmatrix} \frac{1}{\lambda_L} & -k_x \\ k_x \sin k_x a - \frac{\cos k_x a}{\lambda_L} & -k_x \cos k_x a - \frac{\sin k_x a}{\lambda_L} \end{vmatrix} = 0 \quad (6)$$

Therefore, the one important dispersion relation in the transcendental equation is obtained from the above determinant as

$$\tan k_x a = \frac{2\lambda_L k_x}{(k_x \lambda_L)^2 - 1} \quad (7)$$

The non-integer roots of this equation describe the dispersion relations along the  $x$ -axis as a function of London penetration depth and the dimensions of the WGCSW. A graphical method is used for the solution, as shown in Fig. 2, from which the cut-off features are obtained.

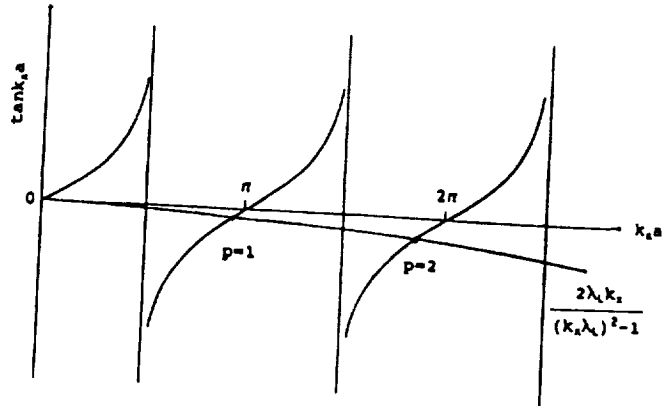


Figure 2. Graphical method of solving (7) to obtain the cut-off features ( $p=1$  is the first root).

Substituting (4a) into (3),

$$H_z = C_1 \left( \cos k_x x + \frac{1}{k_x \lambda_L} \sin k_x x \right) \cos k_y y \quad (8)$$

or

$$H_z = C_2 (k_x \lambda_L \cos k_x x + \sin k_x x) \cos k_y y \quad (9)$$

It is obvious from (9) that  $k_x \neq 0$ , otherwise the solution becomes trivial. It is worth noting that owing to the non-integral nature, the mode indexes are determined by solving (7), which is derived from the Meissner boundary conditions on the two walls.

To avoid risk of confusion with the commonly used  $TE_{nm}$ , the superscripts  $pm$  (the index  $p$  is related to the superconducting walls) are used to designate the modes in the WGCSW. In this case, the dominant mode is designated  $TE^{10}$  ( $p=1$  does not mean integer index along the  $x$ -axis, instead it is the first root of (7)). The above formula, however, does cover conventional waveguides in which  $H_z \propto \cos k_x x \cos k_y y$  when  $\lambda_L \rightarrow \infty$ , as is evident from (8). There are no  $TE^{0m}$  modes in the WGCSW, in which property it is quite different from conventional waveguides.

Substituting (3) into (1),

$$k_c^2 = k_x^2 + k_y^2 \quad (10)$$

Therefore, the cut-off wavelength  $\lambda_c$  is obtained as

$$\lambda_c = \frac{2\pi}{k_c} \quad (11)$$

The numerical results of cut-off wavelengths for some  $TE^{pm}$  modes are listed in the Table. These results demonstrate that the cut-off wavelength of the dominant mode in the WGCSW ( $\lambda_c^{10} \approx 4.06$  mm for  $a=2$  mm) is greater than that of  $TE_{10}$  in a conventional waveguide with the same dimensions by a factor of 1.013, and the bandwidth is greater than an octave.

## 2.2. Field components and surface current distributions

Field component expressions for the TE mode can be determined from the axial magnetic field  $H_z$  by means of the relations between the transverse and axial components as follows.

From (9), let  $B_0 = k_x \lambda_L$  and  $H_0 = C_2$  for simplicity. Then the axial magnetic field component  $H_z$  becomes

$$H_z = H_0 (B_0 \cos k_x x + \sin k_x x) \cos k_y y \quad (12)$$

where  $H_0$  is an unknown coefficient depending on excitations,  $B_0$  is a proportionality parameter which varies for different modes and penetration depths. The wave factor in the form of  $\exp(j\omega t - \gamma z)$  is assumed. The real part  $\alpha$  of the propagation constant  $\gamma$  is the attenuation constant, the imaginary part  $\beta$  is the phase constant and  $\omega$  is the angular frequency. Other field components can be expressed as

$$H_x = \frac{j\beta k_x}{k_c^2} H_0 (B_0 \sin k_x x - \cos k_x x) \cos k_y y \quad (13 a)$$

$$H_y = \frac{j\beta k_y}{k_c^2} H_0 (B_0 \cos k_x x + \sin k_x x) \sin k_y y \quad (13 b)$$

$$E_x = \frac{j\omega \mu_0 k_y}{k_c^2} H_0 (B_0 \cos k_x x + \sin k_x x) \sin k_y y \quad (13 c)$$

$$E_y = \frac{j\omega \mu_0 k_x}{k_c^2} H_0 (B_0 \sin k_x x - \cos k_x x) \cos k_y y \quad (13 d)$$

where  $\mu_0$  is the permeability of the material, assumed to be that of free space.

The wave impedance  $Z_h$  of the WGCSW is defined as

$$Z_h = \frac{E_x}{H_y} = -\frac{E_y}{H_x} = \frac{\omega \mu_0}{\beta} \quad (14)$$

Modes	Cut-off wavelength (mm)			
	$a=1$	$a=2$	$a=4$	$a=8$
TE <sup>10</sup>	2.05 (2.0)**	4.06 (4.0)	8.07 (8.0)	16.09 (16.0)
TE <sup>20</sup>	1.02 (1.0)	2.04 (2.0)	4.07 (4.0)	8.04 (8.0)
TE <sup>11</sup>	0.90 (0.89)	1.79 (1.78)	3.58 (3.58)	7.16 (7.15)
TE <sup>21</sup>	0.70 (0.70)	1.42 (1.41)	2.83 (2.82)	5.66 (5.65)
TE <sup>30</sup>	0.67 (0.48)	1.34 (0.97)	2.67 (1.94)	5.34 (3.88)
TE <sup>31</sup>	0.56 (0.44)	1.11 (0.89)	2.22 (1.79)	4.44 (3.58)

\*For  $\lambda_L = 10^{-8}$  m there is little difference in values.

\*\*Values in parentheses are the corresponding cut-off wavelengths for the first six TE<sub>nm</sub> modes in conventional waveguides.

Cut-off wavelengths for some TE<sup>pm</sup> modes ( $\lambda_L = 10^{-7}$  m,  $a = 2b$ )\*.

The instantaneous field expressions for the dominant TE<sup>10</sup> mode in the WGCSW can be obtained as:

$$H_z = H_0(B_0 \cos k_x x + \sin k_x x) \cos(\omega t - \beta z) \quad (15 a)$$

$$H_x = \frac{\beta k_x}{k_c^2} H_0(B_0 \sin k_x x - \cos k_x x) \sin(\omega t - \beta z) \quad (15 b)$$

$$E_y = \frac{\omega \mu_0 k_x}{k_c^2} H_0(-B_0 \sin k_x x + \cos k_x x) \sin(\omega t - \beta z) \quad (15 c)$$

where,  $\beta = 2\pi/\lambda_g$  is the phase constant of the TE<sup>10</sup> mode, and  $\lambda_g$  is the waveguide wavelength of the TE<sup>10</sup> mode. There are three field components in the WGCSW, as in conventional waveguides. Note that the superscript '10' for the dominant mode is omitted from here on unless otherwise stated.

From the above discussion, (15 c) demonstrates clearly that, due to  $B_0$  being very small, the space distribution of the electric field  $E_y$  of the TE<sup>10</sup> mode is proportional, significantly, to  $\cos k_x x$  along the  $x$ -direction. This means that tangential electric fields exist on the superconducting surfaces ( $x=0$  and  $x=a$ ) of the WGCSW. This novel property is completely different from that of a perfectly conducting conventional waveguide since, for  $H_z \neq 0$  and for a finite surface impedance at microwave and millimetre wavelengths, the tangential components of  $E$  on the superconducting walls are finite. The space distribution along the  $y$ -direction is the same as for conventional waveguides. For details of the field distributions see Fig. 3.

Equation (15 b) demonstrates that the space distribution of the magnetic field  $H_x$  is largely proportional to  $\cos k_x x$ , which means that normal magnetic fields exist on the surfaces ( $x=0$  and  $x=a$ ) (see Fig. 3). The above results demonstrate that the magnetic field lines are not continuous in the WGCSW (Orlando and Delin 1991), which is in agreement with the Meissner effect, but the magnetic flux density  $B$  is continuous in and out of the WGCSW walls because  $B = \mu_0(H + M)$  ( $M$  is the magnetization density in the walls and is not equal to zero). This also is a new property in the WGCSW, which does not exist in conventional waveguides.

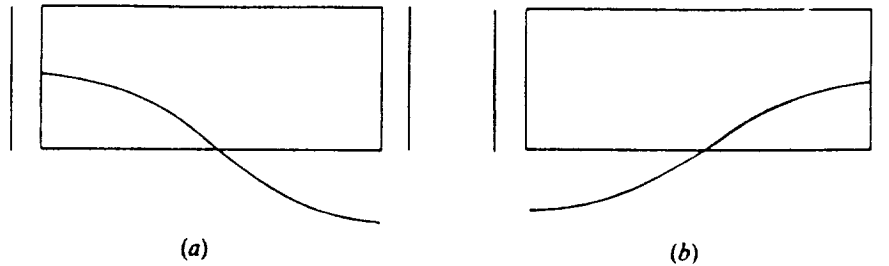


Figure 3. (a) Distribution of the electric field  $E_y$ ; (b) distribution of the magnetic field  $H_x$ , for the TE<sup>10</sup> mode.

London's equations and the two-fluid model are used to investigate the current distribution on the surfaces ( $x=0$  and  $x=a$ ). The total conduction current density consists of the superconducting current density  $J_s$  and the normal electron density  $J_n$  based on the two-fluid model. This model assumes that the conducting electrons in the WGCSW walls are divided into two categories. We use a different method to describe their distribution. The surface superconducting current  $J_{ss}$  due to super-electrons is calculated based on the London relation and appropriate boundary condition first. Then the normal surface current  $J_{sn}$  due to normal electrons and the losses is calculated using the approximate resistive boundary condition and the perturbation approach.

The superconducting current  $J_s$  in two isolated walls in which each wall is considered as a simply-connected superconductor using a thin-film substrate is given as

$$J_s = -\frac{1}{\Lambda} A \quad (16)$$

This is London's relation, where  $\Lambda = \mu_0 \lambda_L^2$ , and  $A$  (in Tm) is the vector potential in the WGCSW. Let the vector potential inside the air-filled hollow region in the waveguide be  $A_a$  (subscript  $a$  indicates the air-filled WGCSW). This satisfies the following equations:

$$\nabla + A_a = B \quad (17)$$

$$E = \frac{k^2 A_a + \nabla \nabla \cdot A_a}{j\omega \mu_0 \epsilon_0} \quad (18)$$

where  $\epsilon_0$  is the permittivity of the material.

Thus, the London relation guarantees that the vector potential is a 'real field' that is completely specified. Equation (18) is called Lorentz's gauge, which gives rise to the relation between the electric field  $E$  and the vector potential  $A_a$  in the air region.

Before solving the current distribution problem, it is important to determine the boundary condition at a boundary between the two media (here, the superconducting medium and air for walls  $x=0$  and  $x=a$ ; the perfect conductor and air for walls  $y=0$  and  $y=b$ ). The boundary condition on the tangential components of fields ( $J_s$  and  $A_a$ ) for the simply-connected superconductor is

$$J_{st} = -\frac{1}{\Lambda} A_{at} \quad (19)$$

where the subscript 'at' denotes the component tangential to the boundary in the air or the applied field region; 'st' denotes the component of supercurrent density tangential to the boundary in the HTS. Note that  $J_{st}$  is the bulk current. Once  $A_a$  is known, the current density  $J_{st}$  and the surface supercurrent density  $J_{sst}$  are readily calculated. The solution satisfying (17) and (18) is obtained from  $B$  as follows:

$$A_{xz} = A_0(B_0 \sin k_x x + \cos k_x x) \sin k_y y \quad (20 a)$$

$$A_{yx} = \frac{jA_0 k_x}{\beta} H_0(B_0 \cos k_x x - \sin k_x x) \sin k_y y$$

$$- \frac{\mu_0 k_y}{k_c^2} H_0(B_0 \cos k_x x + \sin k_x x) \sin k_y y \quad (20 b)$$

$$A_{zy} = \frac{jA_0 k_y}{\beta} (B_0 \sin k_x x + \cos k_x x) \cos k_y y$$

$$+ \frac{\mu_0 k_x}{k_c^2} H_0(B_0 \sin k_x x - \cos k_x x) \cos k_y y \quad (20 c)$$

The surface supercurrent distributions on the isolated walls ( $x=0$  and  $x=a$ ) are obtained from (19) as follows:

( $x=0$  plane)

$$J_{su1} = J_{su1y} a_y + J_{su1z} a_z$$

$$\approx \frac{\lambda_L}{\Lambda} \left[ \frac{\mu_0 k_x}{k_c^2} H_0 \cos k_y y - \frac{jA_0 k_y}{\beta} \cos k_y y \right] a_y - \frac{A_0 \lambda}{\Lambda} \sin k_y y a_z \quad (21 a)$$

( $x=a$  plane)

$$J_{su1} = J_{su1y} a_y + J_{su1z} a_z$$

$$\approx \frac{\lambda_L}{\Lambda} \left[ \frac{\mu_0 k_x}{k_c^2} H_0 \cos k_y y - \frac{jA_0 k_y}{\beta} \cos k_y y \right] a_y + \frac{A_0 \lambda}{\Lambda} \sin k_y y a_z \quad (21 b)$$

where  $J_{su1y}$  and  $J_{su1z}$  are the surface supercurrent magnitudes on the walls along the  $y$ - and  $z$ -directions, respectively. Consider, here, that the superconducting current decays exponentially in the walls, so the current is mainly carried by the superconductor surface adjacent to the air in the WGCSW. It is easy to see that the surface supercurrent and bulk current are very large because the amplitude of  $J_{su1}$  is proportional to  $1/\lambda_L$  ( $\Lambda = \mu_0 \lambda_L^2$ ), which is of the order of  $10^7$ .

All high- $T_c$  materials are type II superconductors. In the Meissner phase, it is assumed that the critical field  $H_{c1} \approx 7.7$  to  $385 \text{ A m}^{-1}$  (depending on temperature) for a HTS sample of  $\text{YBa}_2\text{Cu}_3\text{O}_y$  (88.2 K,  $H_c^{\perp}$  axis) (Wu and Sridhar 1990), so if  $H_0 \approx 13$  to  $660 \text{ A m}^{-1}$ , then the theoretical values of supercurrent density are estimated to be about  $10^{6-8} \text{ A cm}^{-2}$  which is in excellent agreement with other data (Burns 1992, Heinen *et al.* 1991, Miranda *et al.* 1991, Levenson *et al.* 1991). The distributions of surface supercurrent and normal current on the  $x=0$  and  $x=a$

planes of the WGCSW are shown in Fig. 4. (Note that the distributions of the real and imaginary parts of the surface supercurrent of the WGCSW are the same.)

The surface normal current distribution at its boundaries can be obtained using the approximate resistive boundary condition  $\mathbf{n} \times \mathbf{H} = \mathbf{J}_{sn}$  (Senior 1975) as given by

(on the  $y=0$  plane)

$$\begin{aligned} \mathbf{J}_{sn} &= J_{snx} \mathbf{a}_x + J_{snz} \mathbf{a}_z \\ &= H_0 (B_0 \cos k_x x + \sin k_x x) \mathbf{a}_x - \frac{j\beta k_x}{k_c^2} H_0 (B_0 \sin k_x x - \cos k_x x) \mathbf{a}_z \end{aligned} \quad (22 a)$$

(on the  $y=b$  plane)

$$\begin{aligned} \mathbf{J}_{sn} &= J_{snx} \mathbf{a}_x + J_{snz} \mathbf{a}_z \\ &= -H_0 \cos k_y b (B_0 \cos k_x x + \sin k_x x) \mathbf{a}_x \\ &\quad + \frac{j\beta k_x}{k_c^2} H_0 \cos k_y b (B_0 \sin k_x x - \cos k_x x) \mathbf{a}_z \end{aligned} \quad (22 b)$$

(on the  $x=0$  plane)

$$\mathbf{J}_{sn} = J_{sny} \mathbf{a}_y + J_{snz} \mathbf{a}_z = H_0 B_0 \cos k_y a \mathbf{a}_y - \frac{j\beta k_y}{k_c^2} H_0 B_0 \sin k_y a \mathbf{a}_z \quad (22 c)$$

(on the  $x=a$  plane)

$$\begin{aligned} \mathbf{J}_{sn} &= J_{sny} \mathbf{a}_y + J_{snz} \mathbf{a}_z \\ &= -H_0 (B_0 \cos k_x a + \sin k_x a) \cos k_y a \mathbf{a}_y \\ &\quad + \frac{j\beta k_y}{k_c^2} H_0 (B_0 \cos k_x a - \sin k_x a) \sin k_y a \mathbf{a}_z \end{aligned} \quad (22 d)$$

where  $J_{sny}$  and  $J_{snz}$  are the surface normal current magnitudes on the walls along the  $y$ - and  $z$ -directions, respectively. It is easy to see that the distributions of the surface normal currents on the walls  $x=0$  and  $x=a$  are the same as those of the surface supercurrents on the walls, which is the result of the two-fluid model. But the distributions of current on the  $y=0$  and  $y=a$  surfaces differ from conventional waveguides due to different electromagnetic field distributions. The losses of the WGCSW come from the surface normal current flowing through the small surface

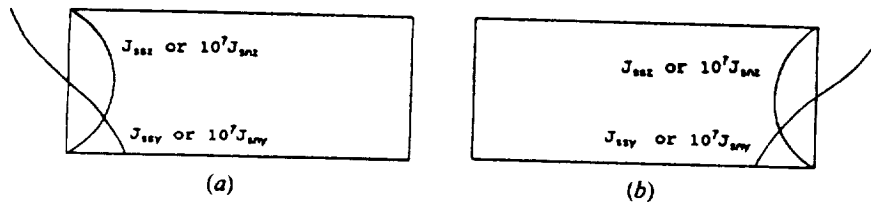


Figure 4. Distribution of surface supercurrent and surface normal current for the  $TE_{10}$  mode on the walls (a)  $x=0$ , (b)  $x=a$ .

impedance. It is predictable that the losses are small because  $B_0$  is very small. The distributions of surface current on the WGCSW planes  $y=0$  and  $y=b$  are shown in Fig. 5.

### 2.3. Attenuation coefficient

The attenuation caused by two superconducting walls and two conventional walls can be calculated by the perturbation technique as given approximately by

$$\alpha^{10} \approx 3.07 \times 10^{-7} \frac{f_c \left[ R_s \left( \frac{f_c}{f} \right)^2 + R_n \right]}{\left[ 1 - \left( \frac{f_c}{f} \right)^2 \right]^{1/2}} \text{ dB km}^{-1} \quad (23)$$

where  $f_c$  is the cut-off frequency of the TE<sup>10</sup> mode,  $R_s$  and  $R_n$  are the surface resistances of HTS and metal walls, respectively, and  $\lambda_L$  is in millimetres. Note that the attenuation is not only proportional to  $f_c^2$  because  $R_s \propto f^2$  (Romanofsky and Bhasin 1992), but also proportional to  $\lambda_L^2$  ( $R_n \propto f^{1/2}$ ). The curve of attenuation coefficient  $\alpha$  versus frequency  $f$  is shown in Fig. 6 in which  $R_s \approx 5.0 \times 10^{-28} f^2 \Omega$ ,  $R_n \approx 2.6 \times 10^{-7} f^{1/2} \Omega$  (Cu), and  $a=2b=2$  mm. As far as the attenuation is concerned, it is greater than that of high- $T_c$  superconducting waveguides, but smaller than that of conventional waveguides.

Losses in the WGCSW are generated from three sources: superconductor loss, metal loss and dielectric loss. A typical superconducting waveguide used in microwave and millimetre-wave circuits uses low-loss dielectrics or free space, so the dominant loss mechanisms are the superconductor loss and metal loss.

The superconductor loss is caused by the current of normal electrons in the superconducting walls based on the two-fluid model theory. The paired superconducting electrons are dissipationless because they cannot be scattered without breaking pairs. The microwave surface resistance of superconducting films has been found to be as low as a few microohms. These surface resistance values are lower than those for copper at the same temperature by a factor of several tens. Such a surface resistance gives a small power loss. If the penetration depth  $\lambda_L = 3.6 \times 10^{-7}$  m for the case of conduction along the c-axis and the surface resistance is equal to 10.3 m $\Omega$  (60 K) at 14.567 GHz (How *et al.* 1992), the attenuation coefficient is found to be about 0.9 dB m<sup>-1</sup> for  $R_n \approx 30$  m $\Omega$ . The metal loss is the same as for conventional waveguides.

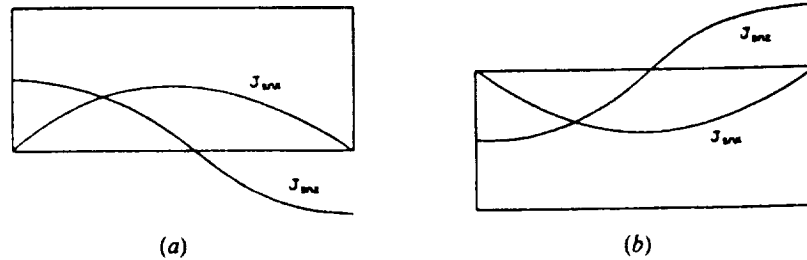


Figure 5. Distribution of surface current for the TE<sup>10</sup> mode on the walls (a)  $y=0$ , (b)  $y=b$ .

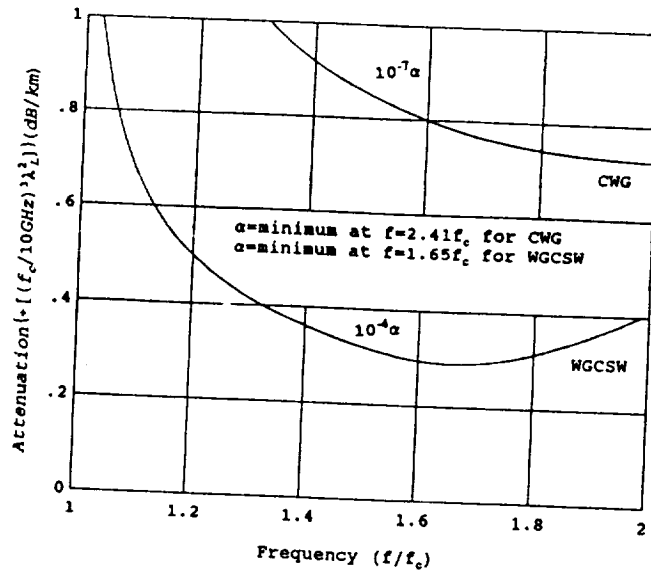


Figure 6. Attenuation due to wall losses versus frequency ( $\lambda_L = 10^{-7}$  m). CWG, conventional waveguide; WGCSW, waveguide with two conventional and two superconducting walls.

#### 2.4. Phase velocity, group velocity and phase dispersion

Superconductors have a frequency-independent penetration depth in the terahertz range, which determines field penetration into the material, rather than a frequency-dependent skin depth as for normal conductors. This means that superconductors introduce practically no dispersion into a microwave circuit. Dispersion in the WGCSW, if any, is due to the frequency dependence of the attenuation caused by the two broad walls. Dispersion caused by the frequency dependence of the phase velocity is almost the same as for conventional waveguides. The phase velocity  $v_p$  and the group velocity  $v_g$  of the  $TE^{10}$  mode can be shown to be given by

$$v_p = \frac{\omega}{\beta} = \frac{c}{\left[1 - \left(\frac{f_c}{f}\right)^2\right]^{1/2}} \quad (24)$$

$$v_g = \frac{d\omega}{d\beta} = c \left(1 - \left(\frac{f_c}{f}\right)^2\right)^{1/2} \quad (25)$$

where  $c$  is the speed of light in free space.

Our work shows that the phase velocity (group velocity) of the WGCSW for the dominant  $TE^{10}$  mode is smaller (greater) (by about 1.4%) than that of conventional waveguides with the same dimensions and frequency because  $f_c$  is smaller than that for conventional waveguides. Therefore, the dispersion produced for the same geometry is small. In summary, the signal distortion due to dispersion in the WGCSW is reduced dramatically by two superconducting walls.

### 2.5. Maximum transmitted power (dominant mode)

The maximum transmitted power in the WGCSW is given by

$$P_{\max} = \frac{ab}{4\eta_0} |E_{\max}| \left[ 1 - \left( \frac{f_c}{f} \right)^2 \right]^{1/2} \quad (26)$$

where  $\eta_0$  is the intrinsic impedance of the medium inside the waveguide, and the magnitude of the electric field intensity  $|E_{\max}|$  is given from (15c) as

$$|E_{\max}| = |H_0| \frac{\omega\mu_0}{k_c} \quad (27)$$

In the Meissner phase, the maximum electric field intensity and power in the WGCSW are smaller than that of conventional waveguides (29 kV cm<sup>-1</sup> and 11 kW) because  $H_0$  is very small. For example, they are about 60 V cm<sup>-1</sup> and 26 mW for  $H_{c1} \approx 77$  mA cm<sup>-1</sup>, and 3 kV cm<sup>-1</sup>, 64 W for  $H_{c1} \approx 3.85$  A cm<sup>-1</sup>, respectively. It is clear from (26) and (27) that the transmitted power and maximum electric field are dependent on the London penetration depth ( $k_c \propto 1/\lambda_L$ ). The larger the London penetration depth, the larger is the transmitted power and maximum electric field. It should be noted that the penetration depth also increases with temperature, which means that more power is carried by the WGCSW.

### 3. Conclusions

A theoretical analysis for a waveguide with two conventional and two superconducting walls has been presented. It is based on high- $T_c$  superconducting electromagnetic theory and Meissner boundary conditions. The important implications of this paper are:

- (a) the bandwidth of the WGCSW is greater than that of conventional metallic waveguides with the same dimensions;
- (b) the tangential electric field and normal magnetic field of the TE<sup>10</sup> mode are finite on the inner surfaces of the walls ( $x=0$  and  $x=a$ ), which is in agreement with Wang *et al.* (1994);
- (c) the magnetic field lines are not continuous in the WGCSW, which is the result of Meissner effect;
- (d) the surface supercurrents are very large and the surface normal currents are very small, so the attenuation coefficient of the WGCSW is smaller than that of conventional waveguides by about 10<sup>2</sup> to 10<sup>3</sup> times for different surface resistance and penetration depth—the main loss mechanism is metal loss due to the two broad walls;
- (e) in the Meissner phase, the maximum electric field intensity and transmitted power are smaller than those of conventional waveguides because the critical field  $H_{c1}$  is very small;
- (f) dispersion is small compared with conventional waveguides;
- (g) the wave impedance  $Z_b$  of the WGCSW has the same expression as for conventional waveguides.

## ACKNOWLEDGMENT

This work was supported by NASA NAG5-1049.

## REFERENCES

- ALAUX, A., and WYBOUW, M., 1976, Propagation of even (EH) mode in superconducting elliptic waveguide. *Canadian Journal of Physics*, **54**, 1488-1492.
- BURNS, G., 1992, *High-Temperature Superconductivity, An Introduction* (New York: Academic Press).
- FABRE, G., WICK, A., and ZEPP, G., 1981, Propagation of an electromagnetic wave on the surface of a conductor or superconductor with a circular cross-section. *Canadian Journal of Physics*, **59**, 902-913.
- HEINEN, V. O., BHASIN, K. B., and LONG, K. J., 1991, Emerging applications of high-temperature superconductors for space communications. *Third Annual Digest, Solid State Technology Branch of NASA Lewis Research Center*, pp. 101-109.
- HOW, H., SEED, R. G., VITTORIA, C., CHRISEY, D. B., HORWITZ, J. S., CAROSELLA, C., and FOLEN, V., 1992, Microwave characteristics of high  $T_c$  superconducting coplanar waveguide resonator. *IEEE Transactions on Microwave Theory and Technology*, **40**, 1668-1672.
- LEVENSON, L. L., STAN, M., and BHASIN, K. B., 1991, Properties of large area  $\text{ErBa}_2\text{Cu}_3\text{O}_{7-x}$  thin films deposited by ionized cluster beams. *Third Annual Digest, Solid State Technology Branch of NASA Lewis Research Center*, pp. 127-130.
- MIRANDA, F. A., GORDON, W. L., BHASIN, K. B., and WARNER, J. D., 1991, Millimeter-wave surface resistance of laser-ablated  $\text{YBa}_2\text{Cu}_3\text{O}_{7-x}$  superconducting films. *Third Annual Digest, Solid State Technology Branch of NASA Lewis Research Center*, pp. 149-151.
- NISENOFF, M., 1988, Superconducting electronics: current status and future prospects. *Cryogenics*, **28**, 47-56.
- ORLANDO, T. P., and DELIN, K. A., 1991, *Foundations of Applied Superconductivity* (Addison-Wesley).
- ROHNER, P. G., 1978, Possibility of low loss transmitting of RF-power with superconducting waveguide cables. *Kerntechnik*, **20**, 489-493.
- ROMANOVSKY, R. R., and BHASIN, K. B., 1992, High temperature superconductor analog electronics for millimeter-wavelength communications. *Fourth Annual Digest, Solid State Technology Branch of NASA Lewis Research Center*, pp. 137-142.
- SENIOR, T. B. A., 1975, Half plane edge diffraction. *Radio Science*, **10**, 645-650.
- VAN DUZER, T., and TURNER, C. W., 1981, *Principles of Superconductive Devices and Circuits* (New York: Elsevier).
- WANG, Y.-C., QIU, Z. A., and YALAMANCHILI, R., 1994, Meissner model of superconducting rectangular waveguides. *International Journal of Electronics*, to be published.
- WU, D. H., and SRIDHAR, S., 1990, Pinning forces and lower critical fields in  $\text{YBa}_2\text{Cu}_3\text{O}_x$  crystals: temperature dependence and anisotropy. *Physics Review Letters*, **65**, 2074-2077.
- YALAMANCHILI, R., QIU, Z. A., and WANG, Y.-C., 1992, Review of microwave distributed superconducting vortex-flow transistor amplifier. *International Journal of Electronics*, **73**, 585-604.
- ZEPP, G., WICK, A., and FABRE, G., 1977, Influence of curvature in superconducting waveguides with circular cross-section. *Canadian Journal of Physics*, **55**, 1551-1560.



## Scattering by the transition junction between a conventional and a high-temperature superconducting waveguide

RAJ. YALAMANCHILI<sup>†</sup>, ZHENG AN QIU<sup>†</sup>  
and YEN-CHU WANG<sup>†</sup>

TE<sub>10</sub> mode scattering during the transition from a conventional to a superconducting rectangular waveguide is investigated based on the Meissner model. The reflection coefficient, input impedance and equivalent inductance are calculated in cm-wave bands when the TE<sub>10</sub> mode is incident on the discontinuity from the conventional (or non-superconducting) waveguide.

### 1. Introduction

Recently there has been considerable progress in the development of superconducting devices in the microwave and millimetre-wave band, for example, low- and high-temperature superconducting microwave filters, resonators, antennas, phase shifters etc. The transmission properties of high-T<sub>c</sub> superconductor waveguide (HTSWG) have been studied recently (Wang *et al.* 1994). In that paper, the propagating TE modes in HTSWG are obtained based on Meissner boundary condition (i.e.  $\partial H_z / \partial n - H_z / \lambda_L = 0$  on the walls, where  $H_z$  is the axial component of magnetic field,  $\lambda_L$  is the London penetration depth).

Since a HTSWG must be connected to its external world, it is important to investigate the EM transition from a conventional waveguide (CWG) to HTSWG. The physical configuration of the problem under study is shown in Fig. 1. It is assumed that the incident wave is the dominant mode, namely, TE<sub>10</sub> mode.

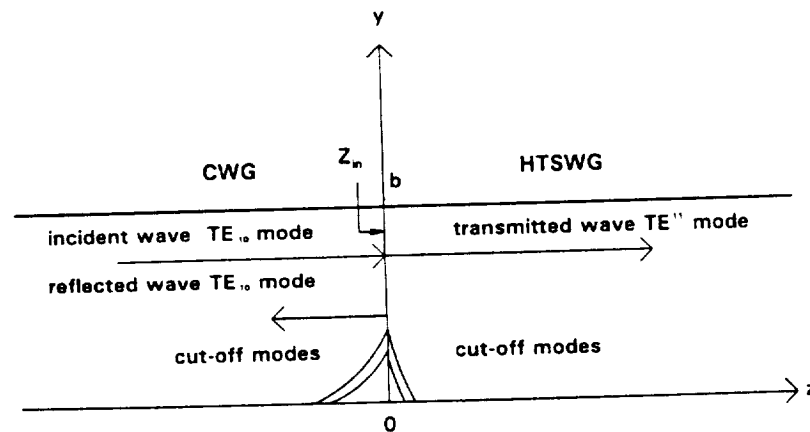


Figure 1. Wave scattering from a rectangular CWG and HTSWG junction at  $z=0$ .

Received 18 October 1993; accepted 12 November 1993.

<sup>†</sup>Department of Electrical Engineering, Howard University, Washington, DC 20059, U.S.A.

travelling from the CWG ( $z < 0$ ) to its HTSWG transition interface (at  $z = 0$ ), in the positive  $z$ -direction with  $\exp(j\omega t)$  time dependence. Although the dimensions of the CWG and HTSWG are the same, the higher-order mode  $TE^{pq}$  ( $p > 1, q \geq 1$ ) (Wang *et al.* 1994) are excited near the transition interface in the HTSWG section ( $z > 0$ ) because of the different waveguides. The CWG dominant mode  $TE_{10}$  is reflected and the higher modes  $TE_{mn}$  ( $m \neq 1, n \neq 0$ ) are excited in the CWG as a result of the different characteristic impedances of the dominant modes in the HTSWG and CWG. Analysis of HTSWG is given briefly in §2. In §3, we consider the reflection coefficient, characteristic impedance and equivalent inductance due to the HTSWG transition when one, two, three or four modes exist in the HTSWG.

## 2. Analysis of high- $T_c$ SC waveguides

A theoretical analysis for HTSWG has been presented by Wang *et al.* (1994) in details based on HTSC electromagnetic theory and the Meissner boundary condition. It can be shown that the field component expressions for the dominant mode  $TE^{11}$  in HTSWG are given as follows:

$$H_z = H_0(B_0 \cos k_x x + \sin k_x x)(C_0 \cos k_y y + \sin k_y y) \quad (1)$$

$$H_x = \frac{j\beta k_x}{k_c^2} H_0(B_0 \sin k_x x - \cos k_x x)(C_0 \cos k_y y + \sin k_y y) \quad (2)$$

$$H_y = \frac{j\beta k_y}{k_c^2} H_0(B_0 \cos k_x x + \sin k_x x)(C_0 \sin k_y y - \cos k_y y) \quad (3)$$

$$E_x = \frac{j\omega\mu_0 k_y}{k_c^2} H_0(B_0 \cos k_x x + \sin k_x x)(C_0 \sin k_y y - \cos k_y y) \quad (4)$$

$$E_y = \frac{j\omega\mu_0 k_x}{k_c^2} H_0(B_0 \sin k_x x + \cos k_x x)(C_0 \cos k_y y + \sin k_y y) \quad (5)$$

where  $\mu_0$  is the permeability of the material which is assumed to be that of free space;  $H_0$  is an unknown coefficient depending on excitations;  $B_0 = k_x \lambda_L$  and  $C_0 = k_y \lambda_L$  are proportionality parameters, but they are different for different modes and penetration depth. The wave factor in the form of  $\exp(j\omega t - \gamma z)$  is assumed;  $k_c$  is the cut-off wavenumber, the real part  $\alpha$  of the propagation constant  $\gamma$  is the attenuation constant, the imaginary part  $\beta = 2\pi/\lambda_g$  is the phase constant,  $\lambda_g$  is the waveguide wave length and  $\omega$  is the angular frequency;  $k_x$  and  $k_y$  are the wavenumbers of the  $TE^{11}$  mode along the  $x$  and  $y$  axes, respectively. Note that the superscripts 11 for the dominant mode in the HTSWG have been suppressed in these and following expressions for convenience, unless stated otherwise. It is worth noting that when considering the HTSWG, because the non-integer mode indexes are determined by solving two transcendental equations of dispersion relations (Wang *et al.* 1994) which are derived from the Meissner boundary condition on the four walls, in order to avoid any risk of confusion with the commonly used  $TE_{mn}$ , we use superscripts to designate the modes in HTSWG, i.e.  $TE^{pq}$ . Here the pair  $^{pq}$  bears

no relationship to the wavenumbers. We choose  $p=1$ ,  $q=1$  for the dominant mode only for convenience.

The wave impedance  $Z^{pq}$  of the  $TE^{pq}$  mode in the HTSWG is defined as

$$Z^{pq} = \frac{E_x}{H_y} = -\frac{E_y}{H_x} = \frac{\omega\mu_0}{\beta^{pq}} \quad (6)$$

where

$$\beta^{pq} = \frac{2\pi}{\lambda_g^{pq}} = (k_0^2 - [(k_x^{pq})^2 + (k_y^{pq})^2])^{1/2} \quad (7)$$

### 3. Reflection coefficient and characteristic impedance

For convenience, the transition interface is assumed to be located at  $z=0$ . Conditions are imposed such that all the waveguide modes except the  $TE_{10}$  mode ( $z<0$ ) and  $TE^{11}$  mode ( $z>0$ ) are below cut-off by suitably choosing some operating frequency. The cut-off modes required for matching the boundary conditions at  $z=0$  are  $TE_{mn}$  modes in the CWG. An incident  $TE_{10}$  wave of unit amplitude is considered. Its reflected wave has amplitude  $\Gamma$  and all the higher-order modes are set up by the transition interface. A transmitted wave  $TE^{11}$  of unknown amplitude  $a^{11}$  is set-up by the interface in the HTSWG on the right-hand side. Therefore, based on the mode-matching technique, the boundary conditions to be satisfied at the junction or transition interface are as follows: the tangential electric field  $E_x$  and magnetic field  $H_x$  must be both continuous, i.e.

$$(1 + \Gamma) \frac{a}{\pi} \sin \frac{\pi}{a} x + \sum_{m=1}^{\infty} \sum_{n=0}^{\infty} \frac{m\pi}{ak_{cmn}^2} a_{mn} \sin \frac{m\pi}{a} x \cos \frac{n\pi}{b} y \\ = \frac{k_x^{pq}}{(k_c^{pq})^2} a^{pq} (-B_0 \sin k_x^{pq} x + \cos k_x^{pq} x) (C_0^{pq} \cos k_y^{pq} y + \sin k_y^{pq} y) \quad (8)$$

$$(\Gamma - 1) \frac{\beta_{10} a}{\pi} \sin \frac{\pi}{a} x + \sum_{m=1}^{\infty} \sum_{n=0}^{\infty} \frac{m\pi \beta_{mn}}{ak_{cmn}^2} a_{mn} \sin \frac{m\pi}{a} x \cos \frac{n\pi}{b} y \\ = \frac{\beta^{pq} k_x^{pq}}{(k_c^{pq})^2} a^{pq} (B_0^{pq} \sin k_x^{pq} x - \cos k_x^{pq} x) (C_0^{pq} \cos k_y^{pq} y + \sin k_y^{pq} y) \quad (9)$$

where  $\Sigma'$  means that when  $m=1$  and  $n=0$ , the unknown coefficient  $a_{mn}=0$  or  $a_{10}=0$ ,  $a$  and  $b$  are the waveguide width and height, respectively. Subscripts 10 and  $mn$  denote the quantities of CWG and superscripts  $pq$  refer to quantities of HTSWG.

Using the well-known orthogonality property of the wave functions for the CWG, by multiplying the CWG wave functions and integrating on both sides of each of the two equations we obtain from eqns (8) and (9)

$$h_0(1 + \Gamma) + h(mn)a_{mn} = \sum_{p=1}^{\infty} \sum_{q=1}^{\infty} a^{pq} F(mn, pq) \quad (10)$$

$$\frac{h_0(\Gamma - 1)}{z_{10}} + \frac{h(mn)}{z_{mn}} a_{mn} = - \sum_{p=1}^{\infty} \sum_{q=1}^{\infty} \frac{a^{pq}}{z^{pq}} F(mn, pq) \quad (11)$$

For the HTSWG, when using a similar orthogonality property (see the Appendix for the proof), one can obtain from eqns (8) and (9) by multiplying the HTSWG wave functions and integrating on both sides of each of the two equations

$$g_0(pq)(1 + \Gamma) + \sum_{m=1}^{\infty} \sum_{n=0}^{\infty} a_{mn} g(mn, pq) = a^{pq} f(pq) \quad (12)$$

$$\frac{g_0(pq)(\Gamma - 1)}{z_{10}} + \sum_{m=1}^{\infty} \sum_{n=0}^{\infty} \frac{a_{mn}}{z_{mn}} g(mn, pq) = -\frac{a^{pq}}{z^{pq}} f(pq) \quad (13)$$

where  $z_{10}$  is the wave impedance of dominant mode  $TE_{10}$ ,  $z_{mn}$  and  $a_{mn}$  are the wave impedances and amplitudes of higher-order modes in the CWG;  $z^{pq}$  and  $a^{pq}$  are the wave impedance and amplitude of mode  $TE^{pq}$  in the HTSWG, respectively. Other quantities are known and given below

$$h_0 = \frac{ab}{2} \quad (14)$$

$$h(mn) = \frac{\pi b m}{4k_{cmn}^2} \quad (15)$$

$$F(mn, pq) = \frac{m\pi k_y^{pq}}{a} \left[ \frac{1 + (-1)^m (B_0^{pq} \sin k_x^{pq} a - \cos k_x^{pq} a)}{\left(\frac{m\pi}{a}\right)^2 - (k_x^{pq})^2} \right] \left[ \frac{1 + (-1)^n (C_0^{pq} \sin k_y^{pq} b - \cos k_y^{pq} b)}{(k_x^{pq})^2 - \left(\frac{n\pi}{b}\right)^2} \right] \quad (16)$$

$$g_0(pq) = \frac{\pi}{a} \left[ \frac{1 + \cos k_x^{pq} a - B_0^{pq} \sin k_x^{pq} a}{\left(\frac{\pi}{a}\right)^2 - (k_x^{pq})^2} \right] \left[ \frac{1 - \cos k_y^{pq} b + C_0^{pq} \sin k_y^{pq} b}{k_y^{pq}} \right] \quad (17)$$

$$g(mn, pq) = \frac{m\pi k_y^{pq}}{a} \left[ \frac{1 + \cos k_x^{pq} a - B_0^{pq} \sin k_x^{pq} a}{\left(\frac{m\pi}{a}\right)^2 - (k_x^{pq})^2} \right] \left[ \frac{1 - \cos k_y^{pq} b + C_0^{pq} \sin k_y^{pq} b}{(k_y^{pq})^2 - \left(\frac{n\pi}{b}\right)^2} \right] \quad (18)$$

$$f(pq) = \frac{ab k_x^{pq}}{(4k_c^{pq})^2} \quad (19)$$

In order to solve (10)–(13) for input impedance and reflection coefficient, etc., we use the iteration method according to the order of one, two, three or four modes in

the HTSWG. Here, only the expressions of one mode are given at the transition interface  $z=0$  (see Fig. 1). The input impedance is

$$Z_{in} = \frac{z^{-11}}{z_{10}} \quad (20)$$

and the reflection coefficient is

$$\Gamma = \frac{z^{-11} - z_{10}}{z^{-11} + z_{10}} \quad (21)$$

where  $Z^{11}$  is the wave impedance of the dominant mode  $TE^{11}$  in the HTSWG. The magnitude and argument of the complex reflection coefficient  $\Gamma$ , with incidence from the CWG, are plotted in Fig. 2 as functions of frequency when one, two, three or four modes are considered. All magnitude and argument curves show similar behaviour. Note that the reflection coefficient magnitude  $\Gamma$  approaches unity when the frequency approaches the cut-off frequency. Above the cut-off frequency a decreasing value of  $\Gamma$  implies a real power flow into the HTSWG. As more modes in the HTSWG are considered,  $|\Gamma|$  and  $\angle\Gamma$  converge to the dashed curves. Since the characteristic impedances in the two different waveguides are quite different, this

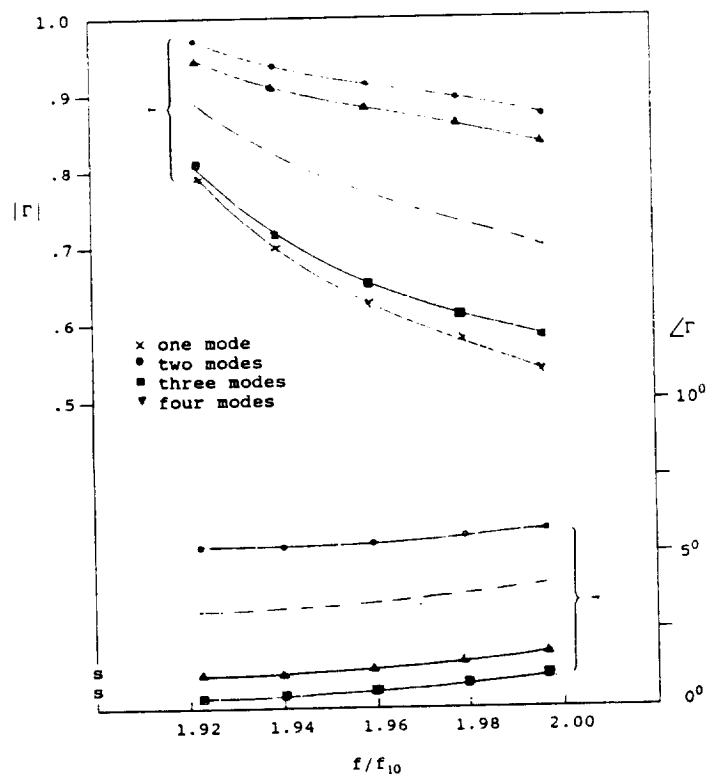


Figure 2. Magnitude and argument of reflection coefficient  $\Gamma$  as a function of frequency. ( $a = 2b = 2.29$  cm,  $\lambda_L = 3.6 \times 10^{-7}$  m,  $f_{10} = 6.55$  GHz,  $f'' = 12.6$  GHz,  $BW = 6.05$  GHz.)

type of variation of  $\Gamma$  is similar to that described by Safaui-Naina and Macphire (1982). In Fig. 3,  $Z_{in}$  is plotted against the frequency. It should be noted that  $Z_{in}$  and  $\Gamma$  are both real quantities when only one mode is considered in the HTSWG. Similarly, the dashed curves are the results when sufficient modes in the HTSWG are considered. It is estimated that 20 modes in the HTSWG will give exact results.

As shown in Fig. 4, the equivalent inductance decreases with frequency. This is due to the superconducting nature of the HTSWG and is independent of the dimension-variation type of discontinuities.

In conclusion, it is found that the transition from a conventional to superconducting waveguide gives rise to large reflection ( $\approx 0.9$  near  $f_{10}$  and decreasing almost linearly with frequency). It is suggested that transformers or other devices for matching are required.

## Appendix

### *Proof of orthogonality of the HTSWG wave functions*

Let  $u$  and  $v$  ( $u \neq v$ ) be arbitrary eigenfunctions in the HTSWG obeying the Helmholtz equation and the Meissner boundary conditions. We obtain

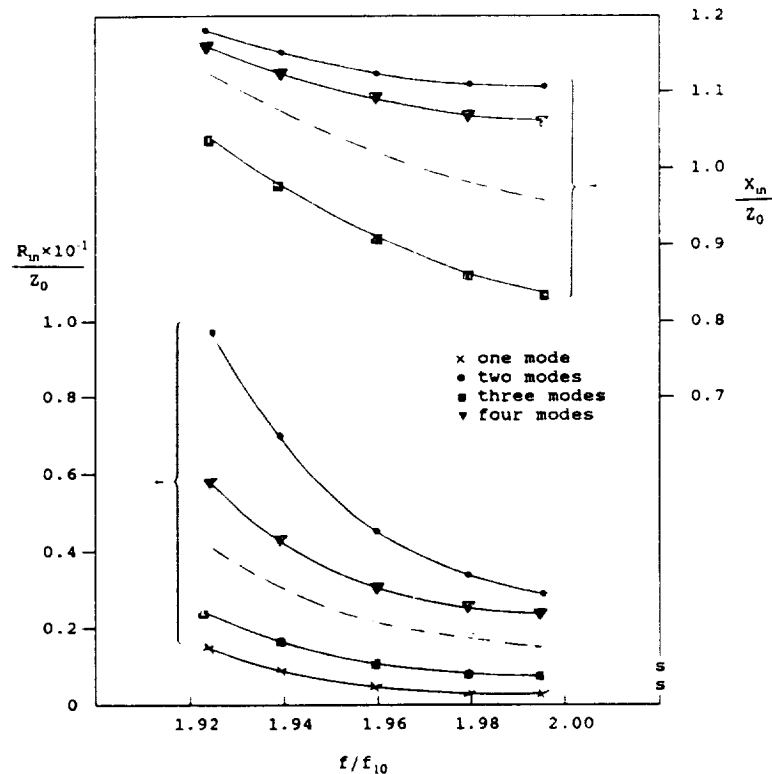


Figure 3. Input impedance  $Z_{in} = R_{in} + jX_{in}$  as function of frequency. ( $a = 2b = 2.29$  cm,  $\lambda_L = 3.6 \times 10^{-7}$  m,  $f_{10} = 6.5$  GHz,  $f'' = 12.6$  GHz,  $BW = 6.05$  GHz.)

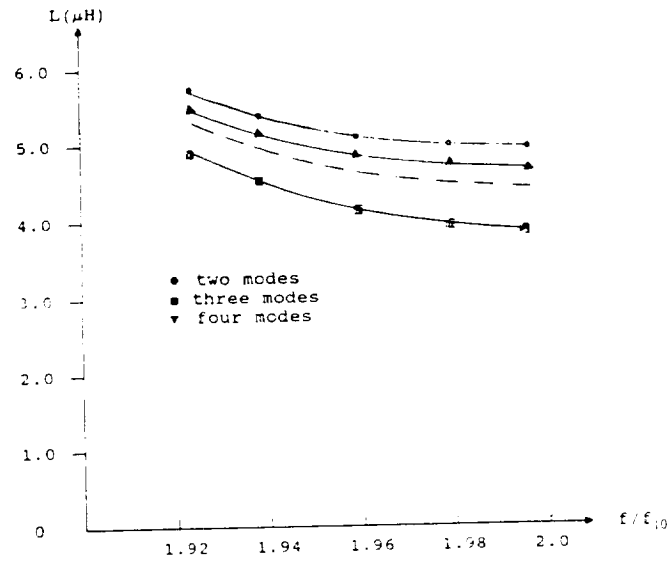


Figure 4. Input inductance as function of frequency. ( $a=2b=2.29$  cm,  $\lambda_L=3.6 \times 10^{-2}$  m,  $f_{10}=6.55$  GHz,  $f''=12.6$  GHz,  $BW=6.05$  GHz.)

$$\nabla_T^2 u + k_c^2 u = 0 \quad (\text{A } 1)$$

$$\frac{\partial u}{\partial n} - \frac{1}{\lambda_L} u = 0 \quad \text{at } x=0, x=a; y=0, y=b \quad (\text{A } 2)$$

$$\nabla_T^2 v + k_d^2 v = 0 \quad (\text{A } 3)$$

$$\frac{\partial v}{\partial n} - \frac{1}{\lambda_L} v = 0 \quad \text{at } x=0, x=a; y=0, y=b \quad (\text{A } 4)$$

then

$$\oint_1 \left( v \frac{\partial u}{\partial n} - u \frac{\partial v}{\partial n} \right) + (k_c^2 - k_d^2) \int_0^a \int_0^b uv \, dx \, dy = 0 \quad (\text{A } 5)$$

By using Green's theorem, it follows that

$$\int_0^a \int_0^b [v(\nabla_T^2 + k_c^2)u - u(\nabla_T^2 + k_d^2)v] \, dx \, dy = 0 \quad (\text{A } 6)$$

From the Meissner boundary condition, we obtain the following relation:

$$\oint_1 \left( \frac{vu}{\lambda_L} - \frac{uv}{\lambda_L} \right) dl + (k_c^2 - k_d^2) \int_0^a \int_0^b uv \, dx \, dy = 0 \quad (\text{A } 7)$$

that is

$$(k_c^2 - k_d^2) \int_0^a \int_0^b uv \, dx \, dy = 0 \quad (\text{A } 8)$$

Generally speaking,  $k_c \neq k_d$ , and we obviously have

$$\int_0^a \int_0^b uv \, dx \, dy = 0 \quad (\text{A } 9)$$

hence the modal wave functions for the HTSWG are orthogonal.

#### ACKNOWLEDGMENTS

This work was supported by NASA grant NAG5-1049.

#### REFERENCES

- SAFAVI-NAINA, R., and MACPHIE, R. H., 1982. Scattering at rectangular-to-rectangular waveguide junctions. *IEEE Transactions Microwave Theory and Techniques*, **30**, 2061-2063.
- WANG, YEN-CHU, QIU, ZHENG AN, and YALAMANCHILI, RAJ, 1994. Meissner model of superconducting rectangular waveguides. *International Journal of Electronics*, **76**, 1151-1171.

## Meissner model of superconducting rectangular waveguides

YEN-CHU WANG<sup>†</sup>, ZHENG AN QIU<sup>†</sup> and  
RAJ YALAMANCHILI<sup>†</sup>

The propagation properties of the  $TE^{pn}$  mode and their dispersion relations in a high temperature superconductor (HTS) rectangular waveguide using the Meissner boundary conditions on all four superconducting walls are presented. In addition to recovering some previously known results, we have obtained some unique and novel results: the dominant mode for HTSWG is the  $TE^{11}$  mode (instead of the conventional  $TE_{10}$  mode) and the tangential electric field and normal magnetic field for the dominant mode  $TE^{11}$  exist on the surfaces. The expressions for electromagnetic components, surface current, attenuation coefficient, the maximum transmitted power, dispersion and wave impedance are also presented. The attenuation is found to be much smaller than that of the conventional waveguides and the dispersion is negligible. The Meissner model presented here has been proved to be valid and powerful for analysis of superconducting waveguides. For the first time, we have shown that the Meissner boundary condition is a key element in boundary value problems for superconductor electromagnetics.

### 1. Introduction

Since the advent of high temperature superconductors (HTS), many superconducting electronic devices have been sought at liquid nitrogen temperatures (Nisenoff 1985, Van Duzer and Turner 1981). Incorporating HTS materials in guided wave systems at microwave and millimetre wavebands is very promising for high speed digital (Hilbert *et al.* 1989), high frequency analogue (Hammond *et al.* 1990), waveguide and transmission line applications in microwave and millimetre-wave devices and circuits (Richard *et al.* 1992, Winters and Rose 1991, Pond and Krowne 1988). Some novel applications of HTSC transmission lines and devices have been given by Yalamanchili *et al.* (1992) and Heinen *et al.* (1991).

The advantages of using HTS at high frequencies include: firstly, very small losses, which means low-attenuation and low-noise; secondly, very small dispersion up to frequencies of several tens of GHz (Kown *et al.* 1987); thirdly, smaller device dimension; and finally the propagation delay time can be greatly reduced because of the smaller size and the shorter interconnects (El-Ghazaly *et al.* 1992).

Experimental and theoretical results have shown that HTS waveguides (HTSWG) and transmission lines exhibit significantly better performance than their identical metallic counterparts. This is because metal transmission systems have ohmic losses at microwave and millimetre-wave bands at which the conventional waveguides (CWG) have extremely high signal attenuation ( $10^4$  dB km<sup>-1</sup> at 200 GHz (Microwave System Design's Handbook 1987)), and therefore are not practical for transmission except over very short distances. The attenuation problem can be virtually eliminated through the use of HTSWG and superconducting transmission lines.

---

Received 18 October 1993; accepted 12 November 1993.

<sup>†</sup>Department of Electrical Engineering, Howard University, Washington, DC 20059, U.S.A.

The superconducting waveguides have been studied previously for low  $T_c$  superconductors ( $< 18$  K) (Alaux and Wybouw 1976, Rohner 1978, Zepp *et al.* 1977, Fabre *et al.* 1981). The modelling of the propagation process in HTS transmission lines has been dealt with by many authors, using both the two-fluid model and the Mattis-Bardeen theory (Dykaar *et al.* 1988, Lee *et al.* 1988, Lam *et al.* 1992, Lee and Barfknecht 1992). High- $T_c$  ( $T_c > 30$  K) superconductors have different properties from low- $T_c$  superconductors. This paper describes the propagation properties of transverse electric (TE) modes in HTSWG based on HTS electromagnetic theory and the Meissner boundary condition consistent with the two-fluid model. We will describe a direct approach for obtaining the general electromagnetic field component expressions, surface current distribution, maximum transmitted power, critical current and electrical field for breakdown, attenuation coefficient, dispersion properties, and wave impedance and compare them with the CWG, wherever possible. Our research confirms that the dominant mode in HTSWG is the  $TE^{11}$  (see below) mode instead of the  $TE_{10}$  mode. Another new property of HTSWG is that the tangential electric field and normal magnetic field of the  $TE^{11}$  mode are non-zero on the surfaces of walls. This property is quite different from the idealized CWG in which the tangential  $E$  and normal  $H$  on the surfaces are equal to zero.

So far the applied physics and engineering researchers' main interest in the high frequency electromagnetic properties of high  $T_c$  superconductors has been the very low attenuation of the EM waves and they have rarely been interested in other, usually more intrinsic, EM properties. This research opens up a new chapter by emphasizing one of the most important EM properties of the superconductors, i.e. the Meissner effect. It can be shown that the well-known boundary conditions for good or perfect conductors are no longer valid and they have to be modified to account for the Meissner effect or the diamagnetic property. The new boundary condition (called the Meissner boundary condition) gives rise to different field solutions hence new waveguide characteristics such as bandwidth, attenuation, current distributions, and others. This model is not only applicable to the waveguide but also to all microwave and millimetre wave engineering problems as long as superconductors, instead of normal metals, are used.

In §2, the most important dispersion relation of HTSWG is derived from the wave equation and the Meissner boundary condition. Expressions for electromagnetic field components and surface currents including the surface superconducting current  $J_{ss}$  and the surface normal current  $J_{sn}$  based on two-fluid theory are given. Various parameters of HTSWG are analysed and compared with CWG. The conclusions are given in §3. Finally detailed derivations of some formulae are given in the Appendices.

## 2. Theory

### 2.1. Wave equation and numerical solutions of cut-off wavelength

In this section, we analyse a HTS rectangular waveguide with all four walls superconducting. A rigorous formulation based on Maxwell's equations and the Meissner boundary condition is used to obtain the unique electromagnetic field properties in the HTS superconducting waveguide.

The governing wave equation (Helmholtz equation) and the Meissner boundary condition for the longitudinal magnetic field  $H_z$  of the TE mode in an air-filled HTSWG are as follows:

$$\nabla_T^2 H_z + k_c^2 H_z = 0 \quad (1)$$

$$\frac{\partial H_z}{\partial n} - \frac{1}{\lambda_L} H_z = 0 \quad \text{at } x=0, x=a; y=0, y=b \quad (2)$$

where the operator  $\nabla_T^2$  is the Laplacian operator in the transverse plane (i.e.  $xy$ -plane). Propagation in the  $z$  direction is assumed. The parameters  $a$  and  $b$  are the HTSWG width and height, respectively.  $k_c$  is the cut-off wavenumber.  $\lambda_L$  is the London penetration depth, for HTS, its values vary from  $10^{-8}$  m to  $10^{-7}$  m (Burns 1992). This parameter, which is a measure of the distance of magnetic field penetration into the superconductor, is very important not only because it can provide information about the fundamental mechanisms for superconductivity in materials but also because of its sensitivity to the quality of the superconductor near its surface. We call (2) the Meissner boundary condition. It accounts for the important Meissner effect in which the fields do not vanish abruptly from the surface of a bulk superconductor, rather, they decay exponentially into the bulk. The penetration depth  $\lambda_L$  is the characteristic decay length of the magnetic field into a superconductor. It is obvious that when  $\lambda_L \rightarrow \infty$ , the second term of the Meissner boundary condition approaches zero, the above equations reduce to the boundary condition  $(\partial H_z / \partial n) = 0$  for the CWG. Therefore, the first term of (2) is related to the properties of the idealized CWG and the secondary term is related to the properties of the HTSWG. Thus the Meissner boundary condition can be taken to be of relevance to the two-fluid SC model.

We assume that the general solution of the governing equation is as follows:

$$H_z = (A_0 \sin k_x x + A_1 \cos k_x x)(A_2 \cos k_y y + A_3 \sin k_y y) \quad (3)$$

where  $A_0, A_1, A_2, A_3$  are the unknown coefficients and none of them are equal to zero. The  $k_x$  and  $k_y$  are the unknown wavenumbers along the  $x$  and  $y$  axes, respectively.

Substituting (3) into the Meissner boundary conditions, we obtain two sets of equations for  $k_x$  and  $k_y$ ,

$$\frac{1}{\lambda_L} A_0 - k_x A_1 = 0 \quad (4a)$$

$$\left(k_x \sin k_x a - \frac{\cos k_x a}{\lambda_L}\right) A_0 - \left(k_x \cos k_x a + \frac{\sin k_x a}{\lambda_L}\right) A_1 = 0 \quad (4b)$$

$$\frac{1}{\lambda_L} A_2 - k_y A_3 = 0 \quad (5a)$$

$$\left(k_y \sin k_y b - \frac{\cos k_y b}{\lambda_L}\right) A_2 - \left(k_y \cos k_y b + \frac{\sin k_y b}{\lambda_L}\right) A_3 = 0 \quad (5b)$$

For non-trivial solution condition, the two determinants of coefficient matrix have to be equal to zero

$$\begin{vmatrix} \frac{1}{\lambda_L} & -k_x \\ k_x \sin k_x a - \frac{\cos k_x a}{\lambda_L} & -k_x \cos k_x a - \frac{\sin k_x a}{\lambda_L} \end{vmatrix} = 0 \quad (6a)$$

$$\begin{vmatrix} \frac{1}{\lambda_L} & -k_y \\ k_y \sin k_y b - \frac{\cos k_y b}{\lambda_L} & -k_y \cos k_y b - \frac{\sin k_y b}{\lambda_L} \end{vmatrix} = 0 \quad (6b)$$

Therefore, the two important dispersion relations in two transcendental equations are obtained from the above determinants as

$$\tan k_x a = \frac{2\lambda_L k_x}{(k_x \lambda_L)^2 - 1} \quad (7)$$

$$\tan k_y b = \frac{2\lambda_L k_y}{(k_y \lambda_L)^2 - 1} \quad (8)$$

The roots of these two equations describe the dispersion relations as a function of the London penetration depth and dimensions for HTSWG. A graphical method is used for solution as shown in Fig. 1 from which the cut-off features will be obtained.

Substituting (4a) and (5a) into (3), we have (see Appendix A)

$$H_z = A_0 A_2 \left( \cos k_x x + \frac{1}{k_x \lambda_L} \sin k_x x \right) \left( \cos k_y y + \frac{1}{k_y \lambda_L} \sin k_y y \right) \quad (9a)$$

or

$$H_z = A_1 A_3 (k_x \lambda_L \cos k_x x + \sin k_x x) (k_y \lambda_L \cos k_y y + \sin k_y y) \quad (9b)$$

It is obvious that  $k_x \neq 0$  and  $k_y \neq 0$  from (9b), otherwise the solution becomes trivial. Our dominant mode is designated to be TE<sup>11</sup>. Thus the dominant mode is no longer the TE<sub>10</sub> mode. This important conclusion is completely different from that of CWG in which the TE<sub>10</sub> mode is dominant. The above formula, however, does cover that of CWG in which  $H_z = H_0 \cos k_x x \cos k_y y$  when  $\lambda_L \rightarrow \infty$  as evident from (9a).

Substituting (3) into (1), we have

$$k_c^2 = k_x^2 + k_y^2 \quad (10)$$

therefore, the cut-off wavelength  $\lambda_c$  is obtained as follows

$$\lambda_c = \frac{2\pi}{k_c} \quad (11)$$

Modes	$a = 1 \text{ mm}$	$a = 2 \text{ mm}$	$a = 4 \text{ mm}$	$a = 8 \text{ mm}$
TE <sup>11</sup>	0.895 (2.0) <sup>†</sup>	1.790 (4.0)	3.579 (8.0)	7.158 (16.0)
TE <sup>21</sup>	0.708 (1.0)	1.415 (2.0)	2.829 (4.0)	5.659 (8.0)
TE <sup>31</sup>	0.555 (0.894)	1.11 (1.789)	2.219 (3.578)	4.438 (7.155)
TE <sup>12</sup>	0.486 (0.707)	0.971 (1.414)	1.941 (2.828)	3.882 (5.657)
TE <sup>22</sup>	0.448 (0.485)	0.895 (0.970)	1.790 (1.940)	3.579 (3.881)
TE <sup>13</sup>	0.329 (0.447)	0.658 (0.894)	1.316 (1.789)	2.631 (3.578)

<sup>†</sup> The figures in parentheses are the corresponding cut-off wavelengths for the first six TE<sub>mn</sub> modes in CWG.

Cut-off wavelengths for some TE<sup>pq</sup> modes ( $\lambda_L = 10^{-7} \text{ m}$ ,  $a = 2b$ ; for  $\lambda_L = 10^{-8} \text{ m}$ , there is little difference between the values).

### 2.2. Field components and surface current distributions

The field component expressions for the TE mode can be determined from the axial magnetic field  $H_z$  by means of the relations between the transverse and axial components as follows.

From (9b), let  $B_0 = \lambda_L k_x$ ,  $C_0 = \lambda_L k_y$  and  $H_0 = A_1 A_3$  for simplicity. Then the magnetic field axial component  $H_z$  becomes (see Appendix A)

$$H_z = H_0 (B_0 \cos k_x x + \sin k_x x) (C_0 \cos k_y y + \sin k_y y) \quad (12)$$

where  $H_0$  is an unknown coefficient depending on excitations,  $B_0$  and  $C_0$  are proportionality parameters, but they are different for different modes and penetration depth. The wave factor in the form of  $\exp(j\omega t - \gamma z)$  is assumed. The real part  $\alpha$  of the propagation constant  $\gamma$  is the attenuation constant, the imaginary part  $\beta$  is the phase constant and  $\omega$  is the angular frequency.

Other field components can be expressed as

$$H_x = \frac{j\beta k_x}{k_c^2} H_0 (B_0 \sin k_x x - \cos k_x x) (C_0 \cos k_y y + \sin k_y y) \quad (13a)$$

$$H_y = \frac{j\beta k_y}{k_c^2} H_0 (B_0 \cos k_x x + \sin k_x x) (C_0 \sin k_y y - \cos k_y y) \quad (13b)$$

$$E_x = \frac{j\omega\mu_0 k_y}{k_c^2} H_0 (B_0 \cos k_x x + \sin k_x x) (C_0 \sin k_y y - \cos k_y y) \quad (13c)$$

$$E_y = \frac{j\omega\mu_0 k_x}{k_c^2} H_0 (-B_0 \sin k_x x + \cos k_x x) (C_0 \cos k_y y + \sin k_y y) \quad (13d)$$

where  $\mu_0$  is the permeability of the material, assumed to be that of free space.

The wave impedance  $Z_h^{pq}$  of HTSWG is defined as

$$Z_h^{pq} = \frac{E_x}{H_y} = -\frac{E_y}{H_x} = \frac{\omega\mu_0}{\beta^{pq}} \quad (14)$$

Modes	$a = 1 \text{ mm}$	$a = 2 \text{ mm}$	$a = 4 \text{ mm}$	$a = 8 \text{ mm}$
TE <sup>11</sup>	0.895 (2.0)†	1.790 (4.0)	3.579 (8.0)	7.158 (16.0)
TE <sup>21</sup>	0.708 (1.0)	1.415 (2.0)	2.829 (4.0)	5.659 (8.0)
TE <sup>31</sup>	0.555 (0.894)	1.11 (1.789)	2.219 (3.578)	4.438 (7.155)
TE <sup>12</sup>	0.486 (0.707)	0.971 (1.414)	1.941 (2.828)	3.882 (5.657)
TE <sup>22</sup>	0.448 (0.485)	0.895 (0.970)	1.790 (1.940)	3.579 (3.881)
TE <sup>13</sup>	0.329 (0.447)	0.658 (0.894)	1.316 (1.789)	2.631 (3.578)

† The figures in parentheses are the corresponding cut-off wavelengths for the first six TE<sub>mn</sub> modes in CWG.

Cut-off wavelengths for some TE<sup>pq</sup> modes ( $\lambda_L = 10^{-7} \text{ m}$ ,  $a = 2b$ ; for  $\lambda_L = 10^{-8} \text{ m}$ , there is little difference between the values).

## 2.2. Field components and surface current distributions

The field component expressions for the TE mode can be determined from the axial magnetic field  $H_z$  by means of the relations between the transverse and axial components as follows.

From (9b), let  $B_0 = \lambda_L k_x$ ,  $C_0 = \lambda_L k_y$  and  $H_0 = A_1 A_3$  for simplicity. Then the magnetic field axial component  $H_z$  becomes (see Appendix A)

$$H_z = H_0 (B_0 \cos k_x x + \sin k_x x) (C_0 \cos k_y y + \sin k_y y) \quad (12)$$

where  $H_0$  is an unknown coefficient depending on excitations.  $B_0$  and  $C_0$  are proportionality parameters, but they are different for different modes and penetration depth. The wave factor in the form of  $\exp(j\omega t - \gamma z)$  is assumed. The real part  $\alpha$  of the propagation constant  $\gamma$  is the attenuation constant, the imaginary part  $\beta$  is the phase constant and  $\omega$  is the angular frequency.

Other field components can be expressed as

$$H_x = \frac{j\beta k_x}{k_c^2} H_0 (B_0 \sin k_x x - \cos k_x x) (C_0 \cos k_y y + \sin k_y y) \quad (13a)$$

$$H_y = \frac{j\beta k_y}{k_c^2} H_0 (B_0 \cos k_x x + \sin k_x x) (C_0 \sin k_y y - \cos k_y y) \quad (13b)$$

$$E_x = \frac{j\omega\mu_0 k_y}{k_c^2} H_0 (B_0 \cos k_x x + \sin k_x x) (C_0 \sin k_y y - \cos k_y y) \quad (13c)$$

$$E_y = \frac{j\omega\mu_0 k_x}{k_c^2} H_0 (-B_0 \sin k_x x + \cos k_x x) (C_0 \cos k_y y + \sin k_y y) \quad (13d)$$

where  $\mu_0$  is the permeability of the material, assumed to be that of free space.

The wave impedance  $Z_n^{pq}$  of HTSWG is defined as

$$Z_n^{pq} = \frac{E_x}{H_y} = -\frac{E_y}{H_x} = \frac{\omega\mu_0}{\beta^{pq}} \quad (14)$$

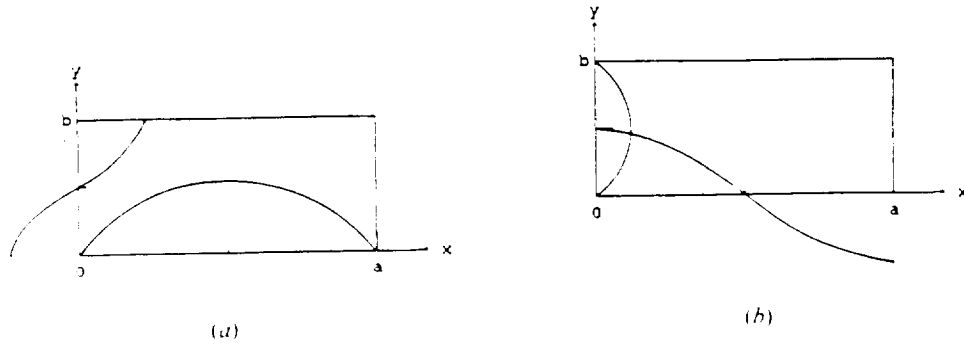


Figure 2. Distribution of electric field  $E_x$  and  $E_y$  for  $TE^{11}$  mode in a cross-section. (a)  $E_x$ ; (b)  $E_y$ .

The instantaneous field expressions for the dominant mode  $TE^{11}$  in HTSWG can be obtained as

$$H_z = H_0(B_0 \cos k_x x + \sin k_x x)(C_0 \cos k_y y + \sin k_y y) \cos(\omega t - \beta z) \quad (15a)$$

$$H_x = \frac{\beta k_x}{k_c^2} H_0(B_0 \sin k_x x - \cos k_x x)(C_0 \cos k_y y + \sin k_y y) \sin(\omega t - \beta z) \quad (15b)$$

$$H_y = -\frac{\beta k_y}{k_c^2} H_0(B_0 \cos k_x x + \sin k_x x)(C_0 \sin k_y y - \cos k_y y) \sin(\omega t - \beta z) \quad (15c)$$

$$E_x = -\frac{\omega \mu_0 k_y}{k_c^2} H_0(B_0 \cos k_x x + \sin k_x x)(C_0 \sin k_y y - \cos k_y y) \sin(\omega t - \beta z) \quad (15d)$$

$$E_y = \frac{\omega \mu_0 k_x}{k_c^2} H_0(-B_0 \sin k_x x + \cos k_x x)(C_0 \cos k_y y + \sin k_y y) \sin(\omega t - \beta z) \quad (15e)$$

$$\beta = \frac{2\pi}{\lambda_g} \quad (16)$$

where  $k_c$ ,  $\beta$ , and  $\lambda_g$  are the cut-off wavenumber, the phase constant, and the waveguide wavelength of the  $TE^{11}$  mode, respectively.  $k_x$  and  $k_y$  are the wavenumbers of the  $TE^{11}$  mode along the  $x$  and  $y$  axes, respectively. Note that the superscripts 11 for the dominant mode have been suppressed here and below unless otherwise stated.

The above equations (15d) and (15e) demonstrate obviously that due to  $B_0$  and  $C_0$  being very small, the space distribution of the electric field  $E_y$  of the  $TE^{11}$  mode is proportional significantly to  $\cos k_x x \sin k_y y$ , which means that the tangential electric fields exist on the surfaces ( $x=0$  and  $x=a$ ) of HTSWG and has maximum at  $y \approx b/2$ . The space distribution of the electric field  $E_x$  is proportional mainly to  $\sin k_x x \cos k_y y$ , which also means that the tangential electric fields exist on the surfaces ( $y=0$  and  $y=b$ ) of HTSWG and are a maximum at  $x \approx a/2$ . The unique and novel property of the finite electric field tangential components on the surfaces of HTSWG was obtained first, which is completely different from that of a perfectly conducting CWG since, for  $H_x \neq 0$  and for a finite surface impedance at microwave and millimetre wavelength, the tangential components of  $E$  on the walls are finite. For details of the field distributions see Fig. 2.

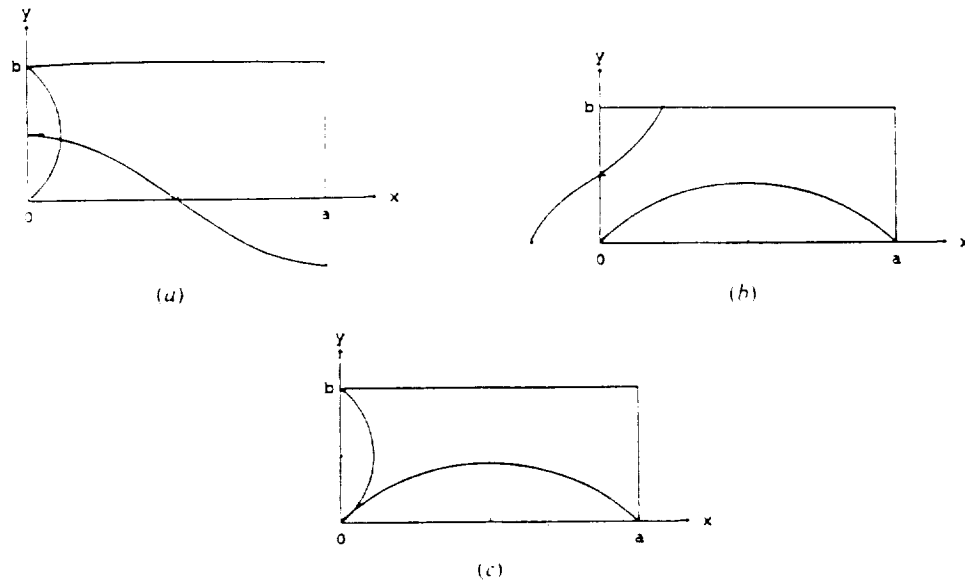


Figure 3. Distribution of magnetic field  $H_x$ ,  $H_y$  and  $H_z$  for  $TE^{11}$  mode in a cross-section. (a)  $H_x$ ; (b)  $H_y$ ; (c)  $H_z$ .

The above equations (15a), (15b) and (15c) demonstrate obviously that as  $B_0$  and  $C_0$  are very small, the space distribution of the magnetic field  $H_y$  of  $TE^{11}$  mode is significantly proportional to  $\sin k_x x \cos k_y y$ , which means that the tangential magnetic field is very small on the surfaces ( $x=0$  and  $x=a$ ) of HTSWG and normal magnetic fields exist at surfaces of  $y=0$  and  $y=b$ . The space distribution of the magnetic field  $H_x$  is proportional mainly to  $\cos k_x x \sin k_y y$ , which means that the tangential magnetic field is also very small on the surfaces of  $y=0$  and  $y=b$  of HTSWG and the normal magnetic field exists on the surfaces of  $x=0$  and  $x=a$ . On the other hand, due to  $H_z \propto \sin k_x x \sin k_y y$ , the magnitudes of the tangential magnetic fields are negligible on all four surfaces. Details of field distributions are given in Fig. 3. The above results demonstrate that the magnetic field lines are not continuous in HTSWG (Orlando and Delin 1991), which is in agreement with the Meissner effect, but the magnetic flux density  $\mathbf{B}$  is continuous in and out of HTSWG walls because  $\mathbf{B} = \mu_0(\mathbf{H} + \mathbf{M})$  ( $\mathbf{M}$  is the magnetization density in the walls and is not equal to zero). This also is a unique property in HTSWG, which does not exist in CWG.

The London equations and the two-fluid model are used to investigate the current distribution. The total conduction current density consists of the superconducting current density  $\mathbf{J}_s$  and the normal electron density  $\mathbf{J}_n$  based on the two-fluid model. This model assumes that the conducting electrons in the HTSWG walls are divided into two categories. We use a different method to describe their distribution. The surface superconducting current  $\mathbf{J}_{ss}$  due to superelectrons is calculated based on the London relation and appropriate boundary condition first. Then the normal surface current  $\mathbf{J}_{sn}$  due to normal electrons and the losses are calculated using the approximate resistive boundary condition and the perturbation approach.

The superconducting current  $\mathbf{J}_s$  in four isolated walls model in which each wall is considered as a simply-connected superconductor using thin film substrate and can be given as

$$\mathbf{J}_s = -\frac{1}{\Lambda} \mathbf{A} \quad (17a)$$

This equation is called the London relation, where  $\Lambda = \mu_0 \lambda_L^2$ .  $\mathbf{A}$ , in units of Tesla-meter, is the vector potential in HTSWG. Let the vector potential inside the air-filled hollow region in the waveguide be  $\mathbf{A}_a$ . It satisfies the following equations.

$$\nabla \times \mathbf{A}_a = \mathbf{B} \quad (17b)$$

$$\mathbf{E} = \frac{k^2 \mathbf{A}_a + \nabla \nabla \cdot \mathbf{A}_a}{j\omega \mu_0 \epsilon_0} \quad (17c)$$

Thus London relation guarantees that the vector potential is a 'real field' that is definitely specified. Equation (17c) is called the Lorentz gauge, which gives rise to the relation between electric field  $\mathbf{E}$  and vector potential  $\mathbf{A}_a$  in the air region.

Before solving the current distribution problem, it is important to determine the boundary conditions at a boundary between the two media (here the superconducting medium and the air). The boundary condition on the tangential components of fields ( $\mathbf{J}_s$  and  $\mathbf{A}_a$ ) for the simply-connected SC is

$$\mathbf{J}_{st} = -\frac{1}{\Lambda} \mathbf{A}_{at} \quad (18)$$

where the subscript 'at' denotes the component tangential to the boundary in the air or the applied field region, the subscript 'st' denotes the component of supercurrent density tangential to the boundary in the HTS. Note that  $\mathbf{J}_{st}$  is the bulk current. Once  $\mathbf{A}_a$  is known, the current density  $\mathbf{K}_{st}$ , and surface supercurrent density  $\mathbf{J}_{st}$  are readily calculated. The solution satisfying (17b) and (17c) is obtained from  $\mathbf{B}$  as follows

$$A_{az} = A_0 (B_0 \sin k_x x + \cos k_x x) (C_0 \sin k_y y + \cos k_y y) \quad (19a)$$

$$A_{ax} = \frac{jA_0 k_x}{\beta} (B_0 \cos k_x x - \sin k_x x) (C_0 \sin k_y y + \cos k_y y) - \frac{\mu_0 k_y}{k_c^2} H_0 (B_0 \cos k_x x + \sin k_x x) (C_0 \sin k_y y - \cos k_y y) \quad (19b)$$

$$A_{ay} = \frac{jA_0 k_y}{\beta} (B_0 \sin k_x x + \cos k_x x) (C_0 \cos k_y y - \sin k_y y) + \frac{\mu_0 k_x}{k_c^2} H_0 (B_0 \sin k_x x - \cos k_x x) (C_0 \cos k_y y + \sin k_y y) \quad (19c)$$

The surface supercurrent distributions on the isolated walls are obtained (see Appendix B) as follows

$y=0$  plane:

$$\begin{aligned} \mathbf{J}_{ssf} &= J_{ssx} \mathbf{a}_x + J_{ssz} \mathbf{a}_z \\ &\approx -\frac{\lambda_L}{\Lambda} \left[ \frac{\mu_0 k_y}{k_c^2} H_0 (B_0 \cos k_x x + \sin k_x x) + \frac{j A_0 k_x}{\beta} (B_0 \cos k_x x - \sin k_x x) \right] \mathbf{a}_x \\ &\quad - \frac{A_0 \lambda_L}{\Lambda} (B_0 \sin k_x x + \cos k_x x) \mathbf{a}_z \end{aligned} \quad (20 a)$$

$y=b$  plane:

$$\begin{aligned} \mathbf{J}_{ssf} &= J_{ssx} \mathbf{a}_x + J_{ssz} \mathbf{a}_z \\ &\approx \frac{\lambda_L}{\Lambda} \left[ \frac{\mu_0 k_y}{k_c^2} H_0 (B_0 \cos k_x x + \sin k_x x) + \frac{j A_0 k_x}{\beta} (B_0 \cos k_x x - \sin k_x x) \right] \mathbf{a}_x \\ &\quad + \frac{A_0 \lambda_L}{\Lambda} (B_0 \sin k_x x + \cos k_x x) \mathbf{a}_z \end{aligned} \quad (20 b)$$

$x=0$  plane:

$$\begin{aligned} \mathbf{J}_{ssf} &= J_{ssy} \mathbf{a}_y + J_{ssz} \mathbf{a}_z \\ &\approx -\frac{\lambda_L}{\Lambda} \left[ -\frac{\mu_0 k_x}{k_c^2} H_0 (C_0 \cos k_y y + \sin k_y y) + \frac{j A_0 k_y}{\beta} (C_0 \cos k_y y - \sin k_y y) \right] \mathbf{a}_y \\ &\quad - \frac{A_0 \lambda_L}{\Lambda} (C_0 \sin k_y y + \cos k_y y) \mathbf{a}_z \end{aligned} \quad (20 c)$$

$x=a$  plane:

$$\begin{aligned} \mathbf{J}_{ssf} &= J_{ssy} \mathbf{a}_y + J_{ssz} \mathbf{a}_z \\ &\approx \frac{\lambda_L}{\Lambda} \left[ -\frac{\mu_0 k_x}{k_c^2} H_0 (C_0 \cos k_y y + \sin k_y y) + \frac{j A_0 k_y}{\beta} (C_0 \cos k_y y - \sin k_y y) \right] \mathbf{a}_y \\ &\quad + \frac{A_0 \lambda_L}{\Lambda} (C_0 \sin k_y y + \cos k_y y) \mathbf{a}_z \end{aligned} \quad (20 d)$$

where  $J_{ssx}$ ,  $J_{ssy}$  and  $J_{ssz}$  are surface supercurrent magnitudes on the walls along the  $x$ ,  $y$  and  $z$  directions, respectively. We consider here that the superconducting current decays exponentially in the walls, therefore the current is mainly carried by the superconductor surface adjacent to the air in the HTSWG. It is easy to see that the surface supercurrent and bulk current are very large because the amplitude of  $\mathbf{J}_{ssf}$  is proportional to  $1/\lambda_L$  ( $\Lambda = \mu_0 \lambda_L^2$ ) which is about the order of  $10^7$ . All high- $T_c$  materials are type II superconductors. In the Meissner phase, we assume that the critical field  $H_{c1} \approx 7.7$  to  $385 \text{ A m}^{-1}$  (depending on temperature) for HTS sample  $\text{YBa}_2\text{Cu}_3\text{O}_y$  (88.2k,  $H$ - $c$  axis) (Wu and Sridhar 1990), therefore  $H_0 \approx 13$  to  $660 \text{ A m}^{-1}$ , then the theoretical values of supercurrent density are estimated to be about  $10^{6-8} \text{ A cm}^{-2}$  which is in excellent agreement with other data (Burns 1992, Heinen *et al.* 1990, Miranda *et al.* 1991, Levenson *et al.* 1991). The distribution of surface supercurrent of HTSWG is shown in Fig. 4. (It should be noted that the

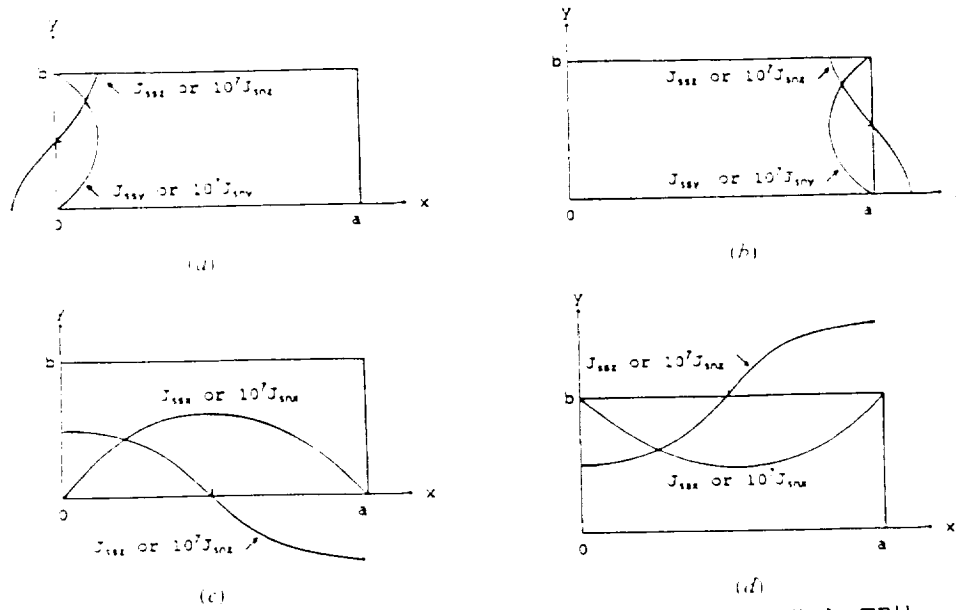


Figure 4. Distribution of surface supercurrent and normal current on walls for  $TE_{11}$  mode in a cross-section: (a)  $x=0$  plane; (b)  $x=a$  plane; (c)  $y=0$  plane; (d)  $y=b$  plane.

distributions of the real and imaginary parts of the surface supercurrent of HTSWG are same.)

The surface normal current distribution at its boundaries can be obtained using approximate resistive boundary condition  $\mathbf{n} \times \mathbf{H} = \mathbf{J}_{sn}$  (Senior 1975) as given by

on the  $y=0$  plane:

$$\begin{aligned} \mathbf{J}_{sn} &= J_{snz} \mathbf{a}_z + J_{snx} \mathbf{a}_x \\ &= -\frac{j\beta k_x}{k_c^2} H_0 C_0 (B_0 \sin k_x x - \cos k_x x) \mathbf{a}_z + H_0 C_0 (B_0 \cos k_x x + \sin k_x x) \mathbf{a}_x \end{aligned} \quad (21a)$$

on the  $y=b$  plane:

$$\begin{aligned} \mathbf{J}_{sn} &= J_{snz} \mathbf{a}_z + J_{snx} \mathbf{a}_x \\ &= \frac{j\beta k_x}{k_c^2} H_0 (B_0 \sin k_x x - \cos k_x x) (C_0 \cos k_y b + \sin k_y b) \mathbf{a}_z \\ &\quad - H_0 (B_0 \cos k_x x + \sin k_x x) (C_0 \cos k_y b + \sin k_y b) \mathbf{a}_x \end{aligned} \quad (21b)$$

on the  $x=0$  plane:

$$\begin{aligned} \mathbf{J}_{sn} &= J_{snz} \mathbf{a}_z + J_{sny} \mathbf{a}_y \\ &= -\frac{j\beta k_y}{k_c^2} H_0 B_0 (C_0 \sin k_y y - \cos k_y y) \mathbf{a}_z + H_0 B_0 (C_0 \cos k_y y + \sin k_y y) \mathbf{a}_y \end{aligned} \quad (21c)$$

on the  $x = a$  plane:

$$\begin{aligned} \mathbf{J}_{sn} &= J_{snz} \mathbf{a}_z + J_{sny} \mathbf{a}_y \\ &= \frac{j\beta k_y}{k_c^2} H_0 (B_0 \cos k_x a - \sin k_x a) (C_0 \sin k_y y - \cos k_y y) \mathbf{a}_z \\ &\quad - H_0 (B_0 \cos k_x a + \sin k_x a) (C_0 \cos k_y y + \sin k_y y) \mathbf{a}_y \end{aligned} \quad (21d)$$

where  $J_{snx}$ ,  $J_{sny}$  and  $J_{snz}$  are the surface normal current magnitudes on the walls along the  $x$ ,  $y$  and  $z$  directions, respectively. It is easy to see that the distribution is the same as that of the surface supercurrents. The losses of HTSWG come from the surface normal current flowing through the small surface impedance. It is predictable that the losses are very small because factors  $B_0$  and  $C_0$  are very small. The distribution of surface normal current of HTSWG is shown in Fig. 4.

### 2.3. Attenuation coefficient

The attenuation (caused by the surface normal current) based on the two-fluid model in HTSWG walls can be calculated by the perturbation technique as given by (see Appendix C)

$$\alpha^{pq} \approx \frac{P_L(z)}{2P_{in}} = R_s \frac{3k_x^2 k_y^2 \beta^2 + k_c^4 (k_x^2 + 2k_y^2)}{b\omega\mu_0\beta k_c^2} \quad (22)$$

For the  $TE^{11}$  mode,  $a = 2$  mm,  $b = 1$  mm,  $k_x = 2\pi/4.0017$  mm,  $k_y = 2\pi/2.001$  mm,  $k_c = 2\pi/1.79$  mm, substituting into (22), we have approximately

$$\alpha^{11} \approx 2.2 \times 10^{-4} R_s \lambda_L^2 \frac{f_c \left[ 0.36 + \left( \frac{f_c}{f} \right)^2 \right]}{\left( 1 - \left( \frac{f_c}{f} \right)^2 \right)^{1/2}} \text{ dB km}^{-1} \quad (23)$$

where  $f_c$  is the cut-off frequency of the  $TE^{11}$  mode,  $R_s$  is the surface resistance of the HTSWG walls in ohms. The unit of  $\lambda_L$  is the millimetre. Note that the attenuation is not only proportional to  $f_c^3$  because  $R_s \propto f^2$  (Romanofsky and Bhasin 1991), but is also proportional to  $\lambda_L^2$ . The relation curve of the attenuation coefficient  $\alpha$  versus the frequency  $f$  is shown in Fig. 5 where  $R_s = 5.0 \times 10^{-2} f^2 \Omega$  and  $a = 2b = 2$  mm.

The losses in HTS waveguides are generated from two sources: superconductor loss and dielectric loss. Typical superconducting waveguides used in microwave and millimetre-wave circuits use low-loss dielectrics or free space, so the dominant loss mechanism is the superconductor loss. This kind of loss is caused by the current of normal electrons in superconducting bulk based on the two-fluid model theory. The paired superconducting electrons are dissipationless because they cannot be scattered without breaking pairs. The microwave surface resistance of superconducting films has been found to be as low as the order of micro-ohms. These surface resistance values are lower than those for Cu at the same temperature by a factor of several tens. Such a surface resistance gives a small power loss. For example,  $R_s = 116 \text{ m}\Omega$  (77k) at 58.6 GHz (Heinen *et al.* 1990),  $\lambda_L = 10^{-7}$  m, the attenuation coefficients are found to be about  $1.1 \times 10^{-2} \text{ dB km}^{-1}$ , which is much smaller than that of CWG (see Fig. 5). If the penetration depth  $\lambda_L = 3.6 \times 10^{-7}$  m for the case of

conduction along the *c*-axis and the surface resistance is equal to 10.3 mΩ (60k) at 14.567 GHz (How *et al.* 1992), the attenuation coefficient is found to be  $9.3 \times 10^{-3}$  dB km<sup>-1</sup>.

2.4. Phase velocity, group velocity and phase dispersion

Superconductors have a frequency-independent penetration depth to the terahertz range that determines field penetration into the material rather than a frequency-dependent skin depth as for normal conductors. This means that superconductors introduce practically no dispersion into a microwave circuit. Dispersion in HTSWG, if any, is due to the frequency dependence in attenuation which has been shown to be negligible because of the very small attenuation coefficient. The dispersion caused by frequency dependence of the phase velocity is almost the same as for the CWG. The phase velocity  $v_p$  and the group velocity  $v_g$  of the TE<sup>11</sup> mode can be shown to be given by

phase velocity

$$v_p = \frac{\omega}{\beta} = \frac{c}{\left(1 - \left(\frac{f_c}{f}\right)^2\right)^{1/2}} \tag{24}$$

group velocity

$$v_g = \frac{d\omega}{d\beta} = c \left(1 - \left(\frac{f_c}{f}\right)^2\right)^{1/2} \tag{25}$$

where *c* is the speed of light in free space.

Our work shows that the phase velocity  $v_p$  of the HTS waveguide for the dominant TE<sup>11</sup> is slightly smaller (about 0.1%) than that of conventional waveguides with the same dimensions and frequency because  $f_c$  is smaller than that of the CWG. Therefore, the dispersion produced for the same geometry is practically the

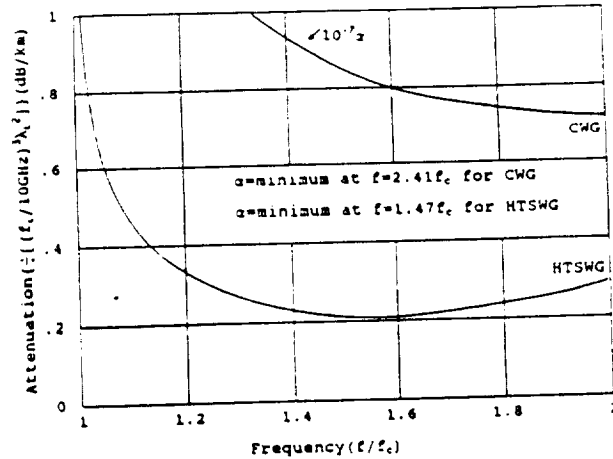


Figure 5. Attenuation due to wall losses versus frequency.  $\lambda_L = 10^{-7}$  m.

same. In summary, the signal distortion due to dispersion in the HTS waveguide is reduced dramatically because it has no dispersion due to attenuation.

### 2.5. Maximum transmitted power (dominant mode)

The maximum transmitted power in HTS waveguide is given by (see Appendix D)

$$P_{\max} = \frac{ab}{8\eta_0} |E_{\max}| \left(1 - \left(\frac{f_c}{f}\right)^2\right)^{1/2} \quad (26)$$

where  $\eta_0$  is the intrinsic impedance of the medium inside the waveguide and  $|E_{\max}|$ , the magnitude of the electric field intensity is given by

$$|E_{\max}| = |H_0| \frac{\omega\mu_0}{k_c} \quad (27)$$

In the Meissner phase, the maximum electric field intensity and power in HTSWG are smaller than that of CWG (29 kV/cm and 11 kW). For example, they are about 60 V/cm, 13 mW for  $H_{c1} \approx 77 \text{ mA cm}^{-1}$  and  $3 \text{ kV cm}^{-1}$ , 32 W for  $H_{c1} \approx 3.85 \text{ A cm}^{-1}$ , respectively. It is clear from eqns (26) and (27) that the transmitted power and maximum  $E$  are dependent on the London penetration depth ( $k_c \propto 1/\lambda_L$ ). The larger the London penetration depth, the larger is the transmitted power and maximum  $E$ . It should be noted that the penetration depth also increases with temperature, which means that more power is carried by the HTS waveguide.

### 3. Conclusions

A theoretical analysis for the HTS rectangular waveguide is presented. It is based on HTS electromagnetic theory and the Meissner boundary condition. The important implications of this paper are: firstly, the bandwidth of the HTS rectangular waveguide is only 1:27:1 which is less than that of a conventional metallic waveguide with the same dimensions; secondly, the tangential electric field and normal magnetic field of the TE<sup>11</sup> mode are finite on the inner surfaces of walls, which demonstrate another quite different property between the HTSWG and the idealized CWG; thirdly, the magnetic field lines are not continuous in HTSWG, which is the result of the Meissner effect; fourthly, because the surface supercurrents are very large and the surface normal currents are very small (the attenuation is very small), the attenuation coefficient of the HTSWG is smaller than that of the CWG by about  $10^4$ - $10^7$  times for different surface resistance and penetration depth. Also, the dispersion caused by attenuation is negligible. This is also quite different from the CWG; fifthly, in the Meissner phase, the maximum electrical field intensity and transmitted power are smaller than that of the CWG because the critical field  $H_{c1}$  is very small; sixthly, the dispersion is negligible compared with the conventional waveguide, as there is no dispersion due to attenuation; and finally, the wave impedance  $Z_{\text{HTS}}^*$  has the same expression as the CWG.

Superconducting waveguides distinguish themselves from normal metal waveguides in the microwave and millimetre-wave bands. Firstly, much lower surface resistance can be obtained with superconductors, giving rise to much lower loss. Secondly, the superconductors have a frequency-independent penetration depth that determines the field penetration into the material rather than the frequency-

same. In summary, the signal distortion due to dispersion in the HTS waveguide is reduced dramatically because it has no dispersion due to attenuation.

### 2.5. Maximum transmitted power (dominant mode)

The maximum transmitted power in HTS waveguide is given by (see Appendix D)

$$P_{\max} = \frac{ab}{8\eta_0} E_{\max}^2 \left( 1 - \left( \frac{f_c}{f} \right)^2 \right)^{1/2} \quad (26)$$

where  $\eta_0$  is the intrinsic impedance of the medium inside the waveguide and  $E_{\max}$ , the magnitude of the electric field intensity is given by

$$E_{\max} = H_{c1} \frac{\omega\mu_0}{k_c} \quad (27)$$

In the Meissner phase, the maximum electric field intensity and power in HTSWG are smaller than that of CWG (29 kV/cm and 11 kW). For example, they are about 60 V/cm, 13 mW for  $H_{c1} \approx 77 \text{ mA cm}^{-1}$  and  $3 \text{ kV cm}^{-1}$ , 32 W for  $H_{c1} \approx 3.85 \text{ A cm}^{-1}$ , respectively. It is clear from eqns (26) and (27) that the transmitted power and maximum  $E$  are dependent on the London penetration depth ( $k_c \propto 1/\lambda_L$ ). The larger the London penetration depth, the larger is the transmitted power and maximum  $E$ . It should be noted that the penetration depth also increases with temperature, which means that more power is carried by the HTS waveguide.

### 3. Conclusions

A theoretical analysis for the HTS rectangular waveguide is presented. It is based on HTS electromagnetic theory and the Meissner boundary condition. The important implications of this paper are: firstly, the bandwidth of the HTS rectangular waveguide is only 1:27:1 which is less than that of a conventional metallic waveguide with the same dimensions; secondly, the tangential electric field and normal magnetic field of the  $\text{TE}^{11}$  mode are finite on the inner surfaces of walls, which demonstrate another quite different property between the HTSWG and the idealized CWG; thirdly, the magnetic field lines are not continuous in HTSWG, which is the result of the Meissner effect; fourthly, because the surface supercurrents are very large and the surface normal currents are very small (the attenuation is very small), the attenuation coefficient of the HTSWG is smaller than that of the CWG by about  $10^4$ - $10^7$  times for different surface resistance and penetration depth. Also, the dispersion caused by attenuation is negligible. This is also quite different from the CWG; fifthly, in the Meissner phase, the maximum electrical field intensity and transmitted power are smaller than that of the CWG because the critical field  $H_{c1}$  is very small; sixthly, the dispersion is negligible compared with the conventional waveguide, as there is no dispersion due to attenuation; and finally, the wave impedance  $Z_h^{pq}$  has the same expression as the CWG.

Superconducting waveguides distinguish themselves from normal metal waveguides in the microwave and millimetre-wave bands. Firstly, much lower surface resistance can be obtained with superconductors, giving rise to much lower loss. Secondly, the superconductors have a frequency-independent penetration depth that determines the field penetration into the material rather than the frequency-

dependent skin depth characterizing normal conductors. This means that superconductors introduce no dispersion into a microwave and millimetre-wave system. Based on these unique characteristics, the HTS waveguide is reasonably attractive for several applications.

This paper has reported that the Meissner model presented here has been proved to be valid and powerful for a more rigorous analysis of superconducting electromagnetic waveguides than those previously attempted which only considered the surface resistance. It should be noted that the Meissner condition has fully accounted for the EM property of an SC surface in the microwave and millimetre-wave bands although it is only indirectly related to the attenuation or surface impedance which is due to the presence of both superconducting and normal electrons, as in the two-fluid model. This is the first successful attempt to model the propagation characteristics of HTSWG using the Meissner boundary condition. We have shown that the Meissner boundary condition is a key element in boundary value problems in superconductor electromagnetics without which its intrinsic electromagnetic properties will not be complete.

This paper has discussed only the case of four isolated SC walls (thus four simply connected SCs) in order to simplify the calculation of the surface current. In the future the case of doubly connected SC waveguide with all four walls as one piece of SC will be considered wherein the surface current will be seen to depend on the magnetic flux quanta passing through the waveguide. Also the anisotropic resistivity effect on the SC waveguide propagation as well as the scattering properties will be presented.

## Appendix A

### *Axial magnetic field $H_z$*

From (4a) and (5a), two relations can be obtained as follows

$$A_0 = k_x \lambda_L A_1 \quad (\text{A } 1 \text{ a})$$

$$A_2 = k_y \lambda_L A_3 \quad (\text{A } 1 \text{ b})$$

Substituting above two equations into the general solution (3), we have

$$\begin{aligned} H_z &= \left( A_0 \cos k_x x + \frac{A_0}{k_x \lambda_L} \sin k_x x \right) \left( A_2 \cos k_y y + \frac{A_2}{k_y \lambda_L} \sin k_y y \right) \\ &= A_0 A_2 \left( \cos k_x x + \frac{1}{k_x \lambda_L} \sin k_x x \right) \left( \cos k_y y + \frac{1}{k_y \lambda_L} \sin k_y y \right) \\ &= A_1 A_3 (\lambda_L k_x \cos k_x x + \sin k_x x) (\lambda_L k_y \cos k_y y + \sin k_y y) \\ &= H_0 (B_0 \cos k_x x + \sin k_x x) (C_0 \cos k_y y + \sin k_y y) \end{aligned} \quad (\text{A } 2)$$

where  $H_0 = A_1 A_3$ ,  $B_0 = k_x \lambda_L$ ,  $C_0 = k_y \lambda_L$ .

## Appendix B

### *Calculation of surface superconducting current*

$y=0$  plane:

From (18), we have

$$J_n = J_{ix} = -\frac{1}{\Lambda} A_{ix} \quad (\text{B } 1)$$

Therefore, the surface currents can be obtained based on the Meissner effect as follows

$$\begin{aligned} J_{ssx} &= \int_{-r}^0 J_{ix} \exp(y/\lambda_L) dy \\ &= \frac{\mu_0 k_y}{\Lambda k_c^2} H_0 (B_0 \cos k_x x + \sin k_x x) \int_{-r}^0 (C_0 \sin k_y y - \cos k_y y) \exp(y/\lambda_L) dy \\ &\quad - \frac{j A_0 k_x}{\Lambda \beta} (B_0 \cos k_x x - \sin k_x x) \int_{-r}^0 (C_0 \sin k_y y + \cos k_y y) \exp(y/\lambda_L) dy \\ &= -\frac{\mu_0 k_y}{\Lambda k_c^2} H_0 (B_0 \cos k_x x + \sin k_x x) \left[ \frac{\lambda_L + C_0 \lambda_L^2 k_y}{1 + (\lambda_L k_y)^2} \right] \\ &\quad - \frac{j A_0 k_x}{\Lambda \beta} (B_0 \cos k_x x - \sin k_x x) \left[ \frac{\lambda_L - C_0 \lambda_L^2 k_y}{1 + (\lambda_L k_y)^2} \right] \end{aligned} \quad (\text{B } 2)$$

$$\begin{aligned} J_{ssz} &= -\frac{A_0}{\Lambda} (B_0 \sin k_x x + \cos k_x x) \int_{-r}^0 (C_0 \sin k_y y + \cos k_y y) \exp(y/\lambda_L) dy \\ &= -\frac{A_0}{\Lambda} (B_0 \sin k_x x + \cos k_x x) \left[ \frac{\lambda_L - C_0 \lambda_L^2 k_y}{1 + (\lambda_L k_y)^2} \right] \end{aligned} \quad (\text{B } 3)$$

Because  $C_0$  and  $\lambda_L$  are very small, we have

$$J_{ssx} \approx -\frac{\mu_0 k_y \lambda_L}{\Lambda k_c^2} H_0 (B_0 \cos k_x x + \sin k_x x) + \frac{j A_0 k_x \lambda_L}{\Lambda \beta} (B_0 \cos k_x x - \sin k_x x) \quad (\text{B } 4)$$

$$J_{ssz} \approx -\frac{A_0 \lambda_L}{\Lambda} (B_0 \sin k_x x + \cos k_x x) \quad (\text{B } 5)$$

$y = b$  plane:

$$\begin{aligned} J_{ssx} &= \int_b^x J_{ix} \exp(-(y-b)/\lambda_L) dy \\ &= \frac{\mu_0 k_y}{\Lambda k_c^2} H_0 (B_0 \cos k_x x + \sin k_x x) \int_0^x (C_0 \sin k_y y - \cos k_y y) \exp(-(y-b)/\lambda_L) dy \\ &\quad - \frac{j A_0 k_x}{\Lambda \beta} (B_0 \cos k_x x - \sin k_x x) \int_b^x (C_0 \sin k_y y + \cos k_y y) \exp(-(y-b)/\lambda_L) dy \\ &= \frac{\mu_0 k_y}{\Lambda k_c^2} H_0 (B_0 \cos k_x x + \sin k_x x) \left[ \frac{(C_0 \lambda_L + \lambda_L^2 k_y) \sin k_y b + (C_0 \lambda_L^2 k_y - \lambda_L) \cos k_y b}{1 + (\lambda_L k_y)^2} \right] \end{aligned} \quad (\text{B } 6)$$

$$\begin{aligned} J_{ssz} &= -\frac{A_0}{\Lambda} (B_0 \sin k_x x + \cos k_x x) \int_b^x (C_0 \sin k_y y + \cos k_y y) \exp(-(y-b)/\lambda_L) dy \quad (\text{B } 7) \\ &= -\frac{A_0}{\Lambda} (B_0 \sin k_x x + \cos k_x x) \left[ \frac{(C_0 \lambda_L - \lambda_L^2 k_y) \sin k_y b + (C_0 \lambda_L^2 k_y + \lambda_L) \cos k_y b}{1 + (\lambda_L k_y)^2} \right] \end{aligned}$$

Because  $C_0$  and  $\lambda_L$  are very small, and  $\cos k_y b \approx -1$ , then

$$J_{ssz} \approx \frac{\mu_0 k_y \lambda_L}{\Lambda k_c^2} H_0 (B_0 \cos k_x x + \sin k_x x) + \frac{j A_0 k_x \lambda_L}{\Lambda \beta} (B_0 \cos k_x x - \sin k_x x) \quad (\text{B } 8)$$

$$J_{ssz} = \frac{A_0 \lambda_L}{\Lambda} (B_0 \sin k_x x + \cos k_x x) \quad (\text{B } 9)$$

Similarly, we have  $J_{ssy}$  and  $J_{ssz}$  on the  $x=0$  and  $x=a$  planes,  $x=0$  plane:

$$J_{ssy} = \frac{\mu_0 k_x}{\Lambda k_c^2} H_0 (C_0 \cos k_y y + \sin k_y y) \left[ \frac{B_0 \lambda_L^2 k_x + \lambda_L}{1 + (\lambda_L k_x)^2} \right] - \frac{j A_0 k_y}{\Lambda \beta} (C_0 \cos k_y y - \sin k_y y) \left[ \frac{\lambda_L - B_0 \lambda_L^2 k_x}{1 + (\lambda_L k_x)^2} \right] \quad (\text{B } 10)$$

$$J_{ssz} = -\frac{A_0}{\Lambda} (C_0 \sin k_y y + \cos k_y y) \left[ \frac{\lambda_L + B_0 \lambda_L^2 k_x}{(\lambda_L k_x)^2 + 1} \right] \quad (\text{B } 11)$$

Because  $B_0$  and  $\lambda_L$  are very small, we have

$$J_{ssy} \approx \frac{\mu_0 k_x \lambda_L}{\Lambda k_c^2} H_0 (C_0 \cos k_y y + \sin k_y y) - \frac{j A_0 k_y \lambda_L}{\Lambda \beta} (C_0 \cos k_y y - \sin k_y y) \quad (\text{B } 12)$$

$$J_{ssz} \approx -\frac{A_0 \lambda_L}{\Lambda \beta} [C_0 \sin k_y y + \cos k_y y] \quad (\text{B } 13)$$

$x=a$  plane:

$$J_{ssy} \approx -\frac{\mu_0 k_x \lambda_L}{\Lambda k_c^2} H_0 (C_0 \cos k_y y + \sin k_y y) + \frac{j A_0 k_y \lambda_L}{\Lambda \beta} (C_0 \cos k_y y - \sin k_y y) \quad (\text{B } 14)$$

$$J_{ssz} \approx \frac{A_0 \lambda_L}{\Lambda \beta} (C_0 \sin k_y y + \cos k_y y) \quad (\text{B } 15)$$

## Appendix C

### Calculation of attenuation coefficient

Using the commonly accepted formula for power in waveguide electromagnetic theory, it is easy to show that transmitted power or the time-average power flowing through a cross-section of HTSWG for the TE<sup>20</sup> mode may be expressed as:

$$\begin{aligned}
P_{in} &= \frac{1}{2} R_s \int_0^a \int_0^b \mathbf{E} \cdot \mathbf{H}^* \cdot \mathbf{a}_z \, dx dy \\
&= \frac{1}{2} R_s Z_h^{pq} \int_0^a \int_0^b (H_x H_x^* - H_y H_y^*) \, dx dy \\
&= \frac{\beta^2 k_x^2}{2k_z^4} |H_0|^2 Z_h^{pq} \int_0^a \int_0^b (B_0 \sin k_x x - \cos k_x x)^2 (C_0 \cos k_y y + \sin k_y y)^2 \, dx dy \\
&\quad - \frac{\beta^2 k_y^2}{2k_z^4} |H_0|^2 Z_h^{pq} \int_0^a \int_0^b (B_0 \cos k_x x + \sin k_x x)^2 (C_0 \sin k_y y - \cos k_y y)^2 \, dx dy \\
&= \frac{\beta^2}{2k_z^4} |H_0|^2 \left\{ k_x^2 \left[ \frac{a}{2} (1 + B_0^2) + \frac{1 - B_0^2}{4k_x} \sin 2k_x a + \frac{B_0}{k_x} \sin^2 k_x a \right] \right. \\
&\quad \left[ \frac{b}{2} (1 + C_0^2) - \frac{1 - C_0^2}{4k_y} \sin 2k_y b - \frac{C_0}{k_y} \sin^2 k_y b \right] \\
&\quad + k_y^2 \left[ \frac{a}{2} (1 + B_0^2) - \frac{1 - B_0^2}{4k_x} \sin 2k_x a - \frac{B_0}{k_x} \sin^2 k_x a \right] \\
&\quad \left. \left[ \frac{b}{2} (1 + C_0^2) - \frac{1 - C_0^2}{4k_y} \sin 2k_y b + \frac{C_0}{k_y} \sin^2 k_y b \right] \right\} Z_h^{pq} \quad (C1)
\end{aligned}$$

In order to calculate the time-average power loss caused by the surface normal current in the walls per unit length, we must consider all four walls. Owing to  $\mathbf{J}_{sn}(y=0) = -\mathbf{J}_{sn}(y=b)$ ,  $\mathbf{J}_{sn}(x=0) = -\mathbf{J}_{sn}(x=a)$ , the total power loss is then double the sum of the losses in the walls at  $x=0$  and  $y=0$ . We have

$$P_L(z) = 2[P_L(z)]_{x=0} + 2[P_L(z)]_{y=0} \quad (C2)$$

where

$$\begin{aligned}
[P_L(z)]_{y=0} &= \frac{1}{2} \int_0^a |J_{sn}(y=0)|^2 \, dx \\
&= \frac{1}{2} R_s \int_0^a \left[ \frac{\beta^2 k_x^2}{k_z^4} |H_0|^2 C_0^2 (B_0 \sin k_x x - \cos k_x x)^2 \right. \\
&\quad \left. + |H_0|^2 C_0^2 (B_0 \cos k_x x + \sin k_x x)^2 \right] \, dx \\
&= \frac{1}{2} R_s |H_0|^2 C_0^2 \left\{ \frac{\beta^2 k_x^2}{k_z^4} \left[ \frac{a}{2} (1 + B_0^2) + \frac{1 - B_0^2}{4k_x} \sin 2k_x a + \frac{B_0}{k_x} \sin^2 k_x a \right] \right. \\
&\quad \left. + \left[ \frac{a}{2} (1 + B_0^2) - \frac{1 - B_0^2}{4k_x} \sin 2k_x a - \frac{B_0}{k_x} \sin^2 k_x a \right] \right\} \quad (C3)
\end{aligned}$$

$$\begin{aligned}
[P_L(z)]_{x=0} &= \frac{1}{2} \int_0^a |J_{zn}(x=0)|^2 dy \\
&= \frac{1}{2} R_s \int_0^a \left[ \frac{\beta^2 k_y^2}{k_c^4} |H_0|^2 B_0^2 (C_0 \sin k_y y - \cos k_y y)^2 \right. \\
&\quad \left. + |H_0|^2 B_0^2 (C_0 \cos k_y y + \sin k_y y)^2 \right] dy \\
&= \frac{1}{2} R_s |H_0|^2 B_0^2 \left\{ \frac{\beta^2 k_y^2}{k_c^4} \left[ \frac{b}{2} (1 + C_0^2) + \frac{1 - C_0^2}{4k_y} \sin 2k_y b + \frac{C_0}{k_y} \sin^2 k_y b \right] \right. \\
&\quad \left. + \left[ \frac{b}{2} (1 + C_0^2) - \frac{1 - C_0^2}{4k_y} \sin 2k_y b - \frac{C_0}{k_y} \sin^2 k_y b \right] \right\} \quad (C4)
\end{aligned}$$

Owing to  $\sin 2k_x a$ ,  $\sin^2 k_x a$ ,  $\sin 2k_y b$ ,  $\sin^2 k_y b$ ,  $B_0$  and  $C_0$  being very small, the higher small terms are ignored and we have

$$P_{in} \approx \frac{ab}{8} |H_0|^2 \frac{\beta^2 Z_n^{pq}}{k_c^2} = \frac{ab}{8} |H_0| \eta_0 \frac{\left(1 - \left(\frac{f_c}{f}\right)^2\right)^{1/2}}{\left(\frac{f_c}{f}\right)} \quad (C5)$$

where  $Z_n^{pq}$  is the wave impedance of  $TE^{pq}$  mode.

Substituting (C3) and (C4) into (C2) and omitting the higher small terms, we have

$$\begin{aligned}
P_L(z) &= \frac{1}{2} a R_s (|H_0| C_0)^2 \left(1 + \frac{\beta^2 k_x^2}{k_c^2}\right) + \frac{1}{2} b R_s (|H_0| B_0)^2 \left(1 + \frac{\beta^2 k_y^2}{k_c^2}\right) \\
&= \frac{1}{2} R_s |H_0|^2 \lambda_L^2 \left\{ a \left[ \left(\frac{\beta k_x k_y}{k_c^2}\right)^2 + k_y^2 \right] + b \left[ \left(\frac{\beta k_x k_y}{k_c^2}\right)^2 + k_x^2 \right] \right\} \quad (C6)
\end{aligned}$$

Therefore the attenuation constant of  $TE^{pq}$  mode can be obtained as follows ( $a=2b$ ):

$$\alpha^{pq} = \frac{P_L(z)}{2P_{in}} = R_s \lambda_L^2 \frac{3k_x^2 k_y^2 \beta^2 + k_c^4 (k_x^2 + 2k_y^2)}{b \omega \mu_0 \beta k_c^2} \quad (C7)$$

For the dominant  $TE^{11}$  mode,  $a=2$  mm,  $b=1$  mm,  $k_x=2\pi/4.0017$  mm,  $k_y=2\pi/2.001$  mm,  $k_c=2\pi/1.79$  mm, substituting into (C7), we have approximately

$$\alpha^{11} \approx 2.2 \times 10^{-4} R_s \lambda_L^2 \frac{f_c \left[ 0.36 + \left(\frac{f_c}{f}\right)^2 \right]}{\left(1 - \left(\frac{f_c}{f}\right)^2\right)^{1/2}} \quad (C8)$$

where  $\lambda_L$  is the London penetration depth in millimetres.

## Appendix D

Calculation of maximum power

$$\begin{aligned} E_{\max}^2 &= E_v^2 + |E_v^-|^2 = H_0^2 \left[ k_v^2 \left( \frac{\omega \mu_0}{k_c^2} \right)^2 + k_v^2 \left( \frac{\omega \mu_0}{k_c^2} \right)^2 \right] \\ &= H_0^2 \left( \frac{\omega \mu_0}{k_c} \right)^2 \end{aligned} \quad (\text{D } 1)$$

where  $E_{\max}$  is the maximum electric field for breakdown.

From (D 1) we have

$$H_0^2 = E_{\max}^2 \frac{k_c^2}{(\omega \mu_0)^2} = E_{\max}^2 \left( \frac{\lambda_c}{\lambda_0} \right)^2 \eta_0^2 \quad (\text{D } 2)$$

Substitution of (D 2) into (C 5) yields

$$P_{\max} \approx \frac{ab}{8\eta_0} E_{\max}^2 \left( 1 - \left( \frac{\lambda_c}{\lambda_0} \right)^2 \right)^2 \quad (\text{D } 3)$$

### ACKNOWLEDGMENT

This work was supported by NASA Grant No. NAG5-1049.

### REFERENCES

- ALAUX, A., and WYBOUW, M., 1976, Propagation of even (EH) mode in superconducting elliptic waveguide. *Canadian Journal of Physics*, **54**, 1488-1492.
- BURNS, G., 1992, *High-Temperature Superconductivity, an Introduction* (New York: Academic Press).
- DYKAAR, D. R., SOBOLEWSKY, R., CHWALEK, J. M., WHITAKER, J. F., HSIANG, T. Y., and MOUROU, G. A., 1988, High-frequency characterization of thin-film Y-Ba-Cu oxide superconducting transmission lines. *Applied Physics Letter*, **52**, 1444-1446.
- EL-GHAZALY, S. M., HAMMOND, R. B., and ITOH, T., 1992, Analysis of superconducting microwave structures: application to microstrip lines. *IEEE Transactions on Microwave Theory and Techniques*, **40**, 499-507.
- FABRE, G., WICK, A., and ZEPP, G., 1981, Propagation of an electromagnetic wave on the surface of a conductor or superconductor with a circular cross-section. *Canadian Journal of Physics*, **59**, 902-913.
- HAMMOND, R. B., NEGRETE, G. V., SCHMIDT, M. S., MOSKOWITZ, M. J., EDDY, M. M., STROTHER, D. D., and SKOGLUND, D. L., 1990, Superconducting Tl-Ca-Ba-Cu-O thin film microstrip resonator and its power handling performance at 77k. *IEEE MTT-S International Microwave Symposium Digest 1990*, Dallas, Texas, pp. 867-870.
- HEINEN, V. O., BHASIN, K. B., and LONG, K. J., 1990, Emerging applications of high-temperature superconductors for space communications. Solid State Technology Branch of NASA Lewis Research Center Third Annual Digest, pp. 101-109, June 1990-June 1991.
- HEINEN, V. O., SOKOLOSKI, M. M., ARON, P. R., and BHASIN, K. B., 1991, NASA space applications of high-temperature superconductors. Solid State Technology Branch of NASA Lewis Research Center Fourth Annual Digest, pp. 143-149, June 1991-June 1992.
- HILBERT, C., GIBSON, D., and HERRELL, D., 1989, A comparison of lossy and superconducting interconnect for computers. *IEEE Transactions on Electron Devices*, **36**, 1830-1839.
- HOW, H., SEED, R. G., VITTORIA, C., CHRISSEY, D. B., HORWITZ, J. S., CAROSELLA, C., and FOLEN, V., 1992, Microwave characteristics of high  $T_c$  superconducting coplanar

- waveguide resonator. *IEEE Transactions on Microwave Theory and Techniques*, **40**, 1668-1672.
- KOWN, O., LANGLEY, B., PEASE, R., and BEASLEY, M., 1987, Superconductors as very high-speed system-level interconnects. *IEEE Electron Device Letters*, **8**, 582-585.
- LAM, C.-W., SHEEN, D. M., ALI, S. M., and OATES, D. E., 1992, Modeling the nonlinearity of superconducting strip transmission lines. *IEEE Transactions on Applied Superconductors*, **2**, 58-66.
- LEE, G. S., and BARFKNECHT, A. T., 1992, Geometric and material dispersion in Josephson transmission lines. *IEEE Transactions on Applied Superconductors*, **2**, 67-73.
- LEE, L. H., ALI, S. M., and LYONS, W. G., 1992, Full-wave characterization of high- $T_c$  superconducting transmission lines. *IEEE Transactions on Applied Superconductors*, **2**, 49-57.
- LEVENSON, L. L., STAN, M., and BHASIN, K. B., 1990, Properties of large area  $\text{ErBa}_2\text{Cu}_3\text{O}_{7-x}$  thin films deposited by ionized cluster beams. Solid State Technology Branch of NASA Lewis Research Center Third Annual Digest, pp. 127-130, June 1990-June 1991.
- MIRANDA, F. A., GORDON, W. L., BHASIN, K. B., and WARNER, J. D., 1990, Millimeter-wave surface resistance of laser-ablated  $\text{YBa}_2\text{Cu}_3\text{O}_{7-x}$  superconducting films. Solid State Technology Branch of NASA Lewis Research Center Third Annual Digest, pp. 149-151, June 1990-June 1991.
- NISENOFF, M., 1988, Superconducting electronics: current status and future prospects. *Cryogenics*, **28**, 47-56.
- ORLANDO, T. P., and DELIN, K. A., 1991, *Foundations of Applied Superconductivity* (Reading, Mass: Addison-Wesley).
- POND, J. M., and KROWNE, C. M., 1988, Slow-wave properties of superconducting microstrip transmission lines. *IEEE MTT-S International Microwave Symposium Digest 1988*. New York, pp. 449-452.
- RICHARD, M. A., BHASIN, K. B., GILBERT, C., METZLER, S., KOEPF, G., and CLASPY, P. C., 1992, Performance of a four-element Ka-band high-temperature superconducting microstrip antenna. *IEEE Microwave Guided Wave Letters*, **2**, 143-145.
- ROHNER, P. G., 1978, Possibility of low loss transmitting of RF-power with superconducting waveguide cables. *Kerntechnik*, **20**, 489-493.
- ROMANOVSKY, R. R., and BHASIN, K. B., 1992, High temperature superconductor analog electronics for millimeter-wavelength communications. Solid State Technology Branch of NASA Lewis Research Center Fourth Annual Digest, pp. 137-142, June 1991-June 1992.
- SENIOR, T. B. A., 1975, Half plane edge diffraction. *Radio Science*, **10**, 645-650.
- The Microwave System Designers Handbook*, fifth edition, Microwave System News and Communications Technology, Vol. 17 (California: EW Communications, July 1987).
- VAN DUZER, T., and TURNER, C. W., 1981, *Principles of Superconductive Devices and Circuits* (New York: Elsevier).
- WINTERS, J. H., and ROSE, C., 1991, High- $T_c$  superconductor waveguides: theory and applications. *IEEE Transactions on Microwave Theory and Techniques*, **39**, 617-623.
- WU, DONG HO, and SRIDHAR, S., 1990, Pinning forces and lower critical fields in  $\text{YBa}_2\text{Cu}_3\text{O}_7$  crystals: temperature dependence and anisotropy. *Physics Review Letter*, **65**, 2074-2077.
- YALAMANCHILI, R., QIU, Z. A., and WANG, Y. C., 1992, Review of microwave distributed superconducting vortex-flow transistor amplifier. *International Journal of Electronics*, **73**, 585-604.
- ZEPP, G., WICK, A., and FABRE, G., 1977, Influence of curvature in superconducting waveguides with circular cross-section. *Canadian Journal of Physics*, **55**, 1551-1560.

## Single-index summation procedure for calculating antenna input impedance

RAJ C. YALAMANCHILI and JAMES W. HALL  
Howard University, Department of Electrical Engineering  
2300 6th Street, N.W.  
Washington, D.C. 20059, U.S.A.  
E-mail : jhall@cldc.howard.edu  
Fax : (202) 806 - 5258

Using the cavity model and Green's functions, equations are derived to express the input impedance of a rectangular patch microstrip antenna as a sum over a single integer index. It is shown that the computer execution time for calculating the input impedance is greatly reduced using the single sum approach rather than the popular double sum approach, without sacrificing accuracy. Double sum solutions were found to take at least twice as long to perform as those of the single sum solutions. The validity of the theoretical results was verified by comparing them with experimental results.

### Notation

$x_p$	x-coordinate of probe location
$y_p$	y-coordinate of probe location
$\nabla_t^2$	transverse Laplacian operator
$k_o$	free space wavenumber
$k$	rectangular-patch (cavity) wavenumber
$k_{mn}$	cavity modal wavenumber
$j$	$(-1)^{1/2}$
$E_z$	z-directed electric field confined within the cavity

# Single-index summation for calculating antenna input impedance

RAJ C. YALAMANCHILI and JAMES W. HALL  
Howard University, Department of Electrical Engineering  
2300 6th Street, N.W.  
Washington, D.C. 20059, U.S.A.  
E-mail : jhall@cldc.howard.edu  
Fax : (202) 806 - 5258

Using the cavity model and Green's functions, equations are derived to express the input impedance of a rectangular patch microstrip antenna as a sum over a single integer index. It is shown that the computer execution time for calculating the input impedance is greatly reduced using the single sum approach rather than the popular double sum approach, without sacrificing accuracy. Double sum solutions were found to take at least twice as long to perform as those of the single sum solutions. The validity of the theoretical results was verified by comparing them with experimental results.

## Notation

$x_p$	x-coordinate of probe location
$y_p$	y-coordinate of probe location
$\nabla_t^2$	transverse Laplacian operator
$k_0$	free space wavenumber
$k$	rectangular-patch (cavity) wavenumber
$k_{mn}$	cavity modal wavenumber
$j$	$(-1)^{1/2}$
$E_z$	z-directed electric field confined within the cavity

$E_{I}$	single-sum cavity electric field for $y \geq y_p$
$E_{II}$	single-sum cavity electric field for $y \leq y_p$
$J$	probe (source) current density
$J_z$	z-directed probe (source) current density
$\omega$	cavity angular frequency
$\omega_{mn}$	modal cavity angular frequency
$\mu_0$	permeability of free space
$I_0$	Amplitude of z-directed current density (source)
$\delta(x-x_p)$	Dirac-delta function used to model x-directed current density contribution at probe location
$\delta(y-y_p)$	Dirac-delta function used to model y-directed current density contribution at probe location
$a_{mn}$	complex modal constant associated with the z-directed electric field
$\psi_{mn}$	modal function associated with the z-directed electric field
$a$	patch length
$b$	patch width
$\epsilon(m)$	Neumann number (= 1 if $m = 0$ , = 2 if $m \neq 0$ )
$\epsilon(n)$	Neumann number (= 1 if $n = 0$ , = 2 if $n \neq 0$ )
$Z$	probe impedance
$Z_{DS}$	double-sum cavity impedance
$Z_{SS}$	single-sum cavity impedance
$Z_{in,DS}$	double-sum cavity input impedance at probe location
$Z_{ant,SS}$	double-sum cavity input impedance at probe location
$f_m(x)$	x-dependent single-sum electric field modal function
$g_m(x)$	x-dependent single-sum electric field modal function
$A_m, B_m$	complex constants associated with $f_m(x)$

$\beta$	real constant associated with $f_m(x)$
H	magnetic field intensity
$H_x$	x-component of magnetic field intensity
$f_+(y)$	single-sum sinusoidal function for $y > y_p$
$f_-(y)$	single-sum sinusoidal function for $y < y_p$
$C_m, D_m$	complex constants associated with $f_+(y)$
$E_m, F_m$	complex constants associated with $f_-(y)$
$A_m, A'_m$	complex constants associated with $g_m(y)$
$\gamma (= \gamma_m)$	single-sum propagation constant
$\bar{a}_x$	x-directed unit vector
$\bar{n}$	inward-directed unit vector normal to cavity wall
$\Omega$	ohms

## 1. Introduction

Several authors have produced fine work concerning microstrip antennas and their various properties, such as input impedance, Q-losses, radiation, etc. (Carver and Mink 1981, Howell 1975, Pozar 1982, Agrawal and Bailey 1977, Dereyd and Lind 1979, Deshpande and Bailey 1982, Watkins 1973, Lo, *et al.* 1977). Many previous works (James and Hall 1981, Lo *et al.* 1979, and Richards *et al.* 1981) have used the cavity model analysis to derive the electric field and input impedance of various microstrip antenna configurations. Usually, the plane of the microstrip is viewed as one geometric region, with length  $a$  and width  $b$ . This approach provides quantities which depend on double-summation solutions summed over two integer indices. Other authors (Chadha, *et al.* 1981, Alhargan *et al.* 1991) have used reduced single summation techniques to find Green's functions for microstrip circular disk and annular ring configurations. In this paper, the rectangular-patch microstrip antenna is analyzed and theoretical and experimental data are directly compared.

By viewing the plane of the microstrip patch as being two separate regions, I and II, bordered by the ordinate of the antenna's thin-probe coordinate,  $y = y_p$ , the electric field and the input impedance can be expressed in terms of solutions which are summed over only one integer index. This single-sum approach greatly reduces execution time, as compared to the double sum approach.

The execution times are compared, and the efficiency of the single-sum approach is demonstrated.

## 2. Theory

### 2.1. *The cavity model*

Authors Lo, Solomon, Richards and Harrison (1979, 1981) developed an analysis of microstrip antennas by modelling them using a lossy cavity bounded by electric walls on the top and bottom, with magnetic walls on the sides.

Figure 1 is the physical representation of a cavity model. The model applies to thin-substrate microstrip antennas whose substrate thickness is  $\leq 1\%$  of a free space wavelength. Fields underneath the top conductor (patch) and above the ground plane are determined by the cavity model such that the electric fields in the antenna structure and the input impedance at the probe position can be determined.

The cavity model assumes that the magnitudes of the tangential magnetic field components at the edges of the patch are negligible, implying a high-impedance condition at the boundary. This condition is equivalent to modelling the perimeter of the patch with magnetic walls. The electromagnetic field components within the cavity are obtained by solving the appropriate Maxwell's Equations within the cavity, subject to the appropriate boundary conditions. It is assumed that the electric fields within the patch are z-directed and invariant with respect to z, due to the presence of a thin substrate.

### 2.2. *Double-sum approach*

#### 2.2.1. *Electric field derivation*

The z-directed electric fields under the patch due to a z-directed current source (probe) must obey the

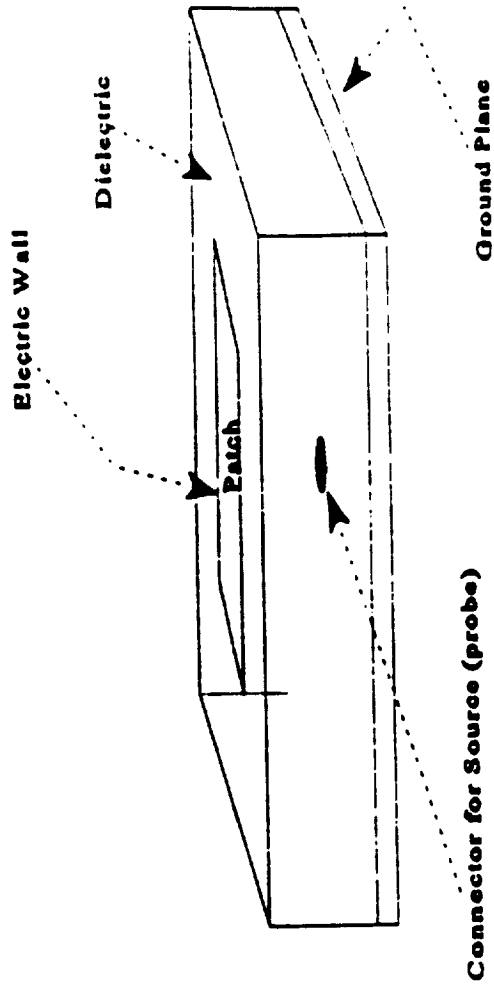


**Figure 1 Basic Rectangular Patch Microstrip Antenna Structure**

inhomogeneous Helmholtz Equation :

$$(\nabla_t^2 + k^2) E_z = j\omega\mu (\vec{J} \cdot \vec{z}) = j\omega\mu_0 J_z \quad (1)$$

where,  $J_z$  is the z-directed current density on the probe. Since such probes are usually very thin with respect to the excitation frequency, delta functions have to be used to describe the current density :

$$J_z = I_0 \delta(x-x_p) \delta(y-y_p) \quad (2)$$

where,  $(x_p, y_p)$  is the coordinate of the probe position on the patch. Assuming  $E_z$  can be expanded in terms of a Generalized Fourier Series,

$$E_z = \sum_{m=0}^{\infty} \sum_{n=0}^{\infty} a_{mn} \Psi_{mn}(x, y) \quad (3)$$

where,  $a_{mn}$  is a constant, and  $\Psi_{mn}(x,y) = E_0 \cos(m\pi x/a) \cos(n\pi y/b)$ , such that  $E_0 = V_0/d$  is constant,  $d$  = substrate thickness, and the  $\Psi_{mn}$ 's represent modal solutions to the homogeneous form of (1). Substituting (3) into (1),

$$\sum_{m=0}^{\infty} \sum_{n=0}^{\infty} a_{mn} (k^2 - k_{mn}^2) \Psi_{mn} = j\omega\mu_0 I_0 \delta(x-x_p) \delta(y-y_p) \quad (4)$$

where,  $k_{mn}^2 = (m\pi x/a)^2 + (n\pi x/b)^2$ . Multiplying both sides by  $\Psi_{mn}^*(x,y)$  and integrating from  $x = 0$  to  $x = a$ , and  $y = 0$  to  $y = b$ , over  $dS = dx dy$ , the z-directed double-sum form of the electric field under the patch becomes :

$$E_z = \left( \frac{j\omega\mu_0 I_0}{ab} \right) \sum_{m=0}^{\infty} \sum_{n=0}^{\infty} \frac{\cos\left(\frac{m\pi x}{a}\right) \cos\left(\frac{m\pi x_p}{a}\right) \cos\left(\frac{n\pi y}{b}\right) \cos\left(\frac{n\pi y_p}{b}\right) \epsilon(m) \epsilon(n)}{(k^2 - k_{mn}^2)} \quad (5)$$

The Neumann numbers  $\epsilon(m)$  and  $\epsilon(n)$  are, in general, represented as :

$\epsilon(\mu) = [ 1, \mu = 0 ; 2, \mu \neq 0 ]$ , and  $k^2 = k_0^2 \epsilon_r (1 - j\delta)$ . The amplitude coefficient from (4) is :

$$a_{mn} = \frac{j\omega \mu_0 \langle J_z, \Psi_{mn} \rangle}{\langle \Psi_{mn}, \Psi_{mn} \rangle (k^2 - k_{mn}^2)} \quad (6)$$

Here , the inner product is defined as :

$$\langle f(x,y), g(x,y) \rangle = \iint_S f(x,y) g^*(x,y) dS \quad (7)$$

and  $\langle \Psi_{mn}, \Psi_{mn} \rangle = (a b) / (\epsilon(m) \epsilon(n))$ .

### 2.2.2. Input impedance

Since  $E_z$  is assumed to be invariant to  $z$ , the impedance at the probe position is :

$$Z = \frac{V}{I} = \frac{- \int_0^d \vec{E}_{probe} \cdot d\vec{l}}{I_0} = \frac{-d E_z (x_p, y_p)}{I_0} \quad (8)$$

where,  $I_0$  is the probe current. However, the effect of the probe reactance,  $X_f$ , must be accounted for in order to obtain the overall input impedance at the probe position :

$$X_f = \frac{\eta_0}{\sqrt{\epsilon_r}} \tan [\sqrt{\epsilon_r} k_0 t] \quad (9)$$

where  $t$  is the probe thickness and  $\eta_0$  is the free space impedance.

Evaluating  $E_z$  at  $x = x_p$ ,  $y = y_p$ , from (5) gives :

$$E_z = \frac{j\omega\mu_0 I_0}{ab} \sum_{m=0}^{\infty} \sum_{n=0}^{\infty} \frac{\cos\left(\frac{m\pi x}{a}\right)\cos\left(\frac{m\pi x_p}{a}\right)\cos\left(\frac{n\pi y}{b}\right)\cos\left(\frac{n\pi y_p}{b}\right)\epsilon(m)\epsilon(n)}{[k_{\text{eff}}^2 - k_{mn}^2]} \quad (10)$$

Therefore,

$$Z_{DS} = \frac{-j\omega\mu_0 d c^2}{ab\epsilon_r} \sum_{m=0}^{\infty} \sum_{n=0}^{\infty} \frac{\cos\left(\frac{m\pi x}{a}\right)\cos\left(\frac{m\pi x_p}{a}\right)\cos\left(\frac{n\pi y}{b}\right)\cos\left(\frac{n\pi y_p}{b}\right)\epsilon(m)\epsilon(n)}{[\omega_{mn} - (1 - j/Q_{TOT})\omega^2]} \quad (11)$$

where,  $k_{\text{eff}}^2 = \epsilon_r(1 - \delta_{\text{eff}})k_0^2$  and  $\delta = \delta_{\text{eff}} = 1/Q_{TOT}$ . Therefore, the input impedance seen at the probe is :

$$Z_{m,DS} = Z_{DS} + jX_f \quad (12)$$

where, "DS" refers to double sum.

### 2.3. Single-sum approach

#### 2.3.1. Electric field derivation

Referring to figure 2, the patch is divided into two geometric regions: region I, where  $y > y_p$  and region II, where  $y < y_p$ . Solutions, for the electric field must be obtained for each region, in accordance with the inhomogeneous Helmholtz equation (equation (1)). It is assumed that :

$$E_z = f(x)g(y) = \sum_{m=0}^{\infty} f_m(x)g_m(y) \quad (13)$$

where,  $f$  and  $g$  depend on the modal index  $m$  ( $m = 0, 1, 2, \dots$ ), and

$$f_m(x) = A_m \cos(\beta x) + B_m \sin(\beta x) \quad (14)$$

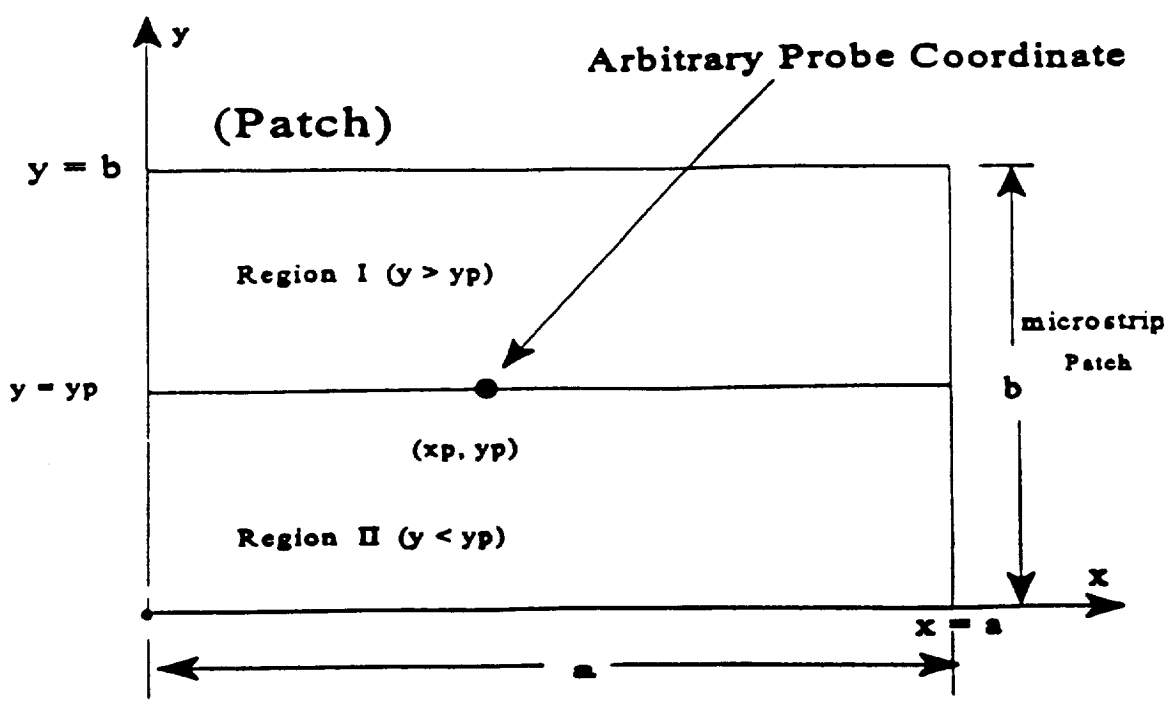


Figure 2 Two-Region , Single-Sum Patch Area

with  $A_m$  and  $B_m$  being complex constants. The required boundary conditions are :

$$\vec{n} \times \vec{H} \Big|_{\text{on magnetic walls}} = 0 \quad (15)$$

Enforcing the boundary conditions at  $x = 0$  and at  $x = a$  gives :

$$E_z = \sum_{m=0}^{\infty} A_m \text{Cos} \left( \frac{m\pi x}{a} \right) g_m(y) \quad (16)$$

Substitution of (16) into (1) , after multiplying each side of the new equation by  $\text{Cos}(m\pi x/a)$  , and integrating from  $x=0$  to  $x=a$  , gives :

$$\left[ \frac{\partial^2}{\partial y^2} - \left( \frac{m\pi}{a} \right)^2 + k^2 \right] g_m(y) = j\omega\mu_0 I_0 \frac{\varepsilon(m)}{a} \text{Cos} \left( \frac{m\pi x_p}{a} \right) \delta ( y - y_p ) \quad (17)$$

The Green's functions solutions  $g_m(y)$  in the  $y$ -direction are continuous at the  $y = y_p$  boundary. However, the derivatives at this boundary are not equal due to a jump condition from the probe excitation. From Felson *et al.* 1993, the components of the Green's functions in regions I and II can be expressed as :

$$g_m(y) = A_m f_+(y) f_-(y_p) , \quad y > y_p \quad \text{region I} \quad (18)$$

$$g_m(y) = A_m f_-(y) f_+(y_p) , \quad y < y_p \quad \text{region II} \quad (19)$$

where,  $f_+(y)$  and  $f_-(y)$  are functions belonging to regions I and II , respectively.

Assuming sinusoidal variation ,

$$f_+(y) = C_m \text{Cos}(\gamma y) + D_m \text{Sin}(\gamma y) , \quad y \geq y_p \quad (20)$$

$$f_z(y) = E_m \cos(\gamma y) + F_m \sin(\gamma y), \quad y \leq y_p \quad (21)$$

for  $C_m$ ,  $D_m$ ,  $E_m$  and  $F_m$  as complex constants. Using the Maxwell equation, which relates the curl of the electric field vector to the magnetic fields, gives :

$$-j\omega\mu H_x = \sum_{m=0}^{\infty} A_m \cos\left(\frac{m\pi x}{a}\right) \frac{\partial g_m(y)}{\partial y} \quad (22)$$

The boundary conditions

$$\vec{n} \times H_x \vec{a}_x \Big|_{y=0, b} = 0 \quad (23)$$

yield  $F_m = 0$ , and

$$f_z(y) = E_m \cos(\gamma y) \quad (24)$$

Letting  $A_m' = A_m E_m$ , and realizing from (23) that  $C_m = \cos(\gamma b)$  and  $D_m = \sin(\gamma b)$ , we have :

$$f_z(y) = \cos[\gamma(y-b)] \quad (25)$$

Letting the Green's functions  $g_m(y) = G_{ym}(y, y_p)$ , we have, for each respective patch region :

$$G_{y_m}(y, y_p) = A_m' \cos(\gamma y_p) \cos(\gamma(y-b)), \quad y \geq y_p, \quad \text{region I} \quad (26)$$

$$G_{y_m}(y, y_p) = A_m' \cos(\gamma y) \cos(\gamma(y_p - b)), \quad y \leq y_p, \quad \text{region II} \quad (27)$$

Note that (26) and (27) are equal at the  $y = y_p$  boundary of regions I and II.

Following the procedure outlined in Felson *et al.* 1993 to determine  $A_m'$ , we have :

$$A_m' = j\omega\mu_0 I_0 \frac{\varepsilon(m)}{a} \frac{\text{Cos} \left( \frac{m\pi x_p}{a} \right)}{\gamma \text{Sin}(\gamma b)} \quad (28)$$

Substituting (28) in (13), for the appropriate region, the single-index electric-field quantities of the microstrip antenna are :

$$E_{z_I} = \sum_{m=0}^{\infty} \frac{j\omega\mu_0 I_0 \varepsilon(m)}{a\gamma \text{Sin}(\gamma b)} \text{Cos} \left( \frac{m\pi x_p}{a} \right) \text{Cos} \left( \frac{m\pi x}{a} \right) \text{Cos}(\gamma y_p) \text{Cos}(\gamma(y-y_p)) \quad , \quad y \geq y_p \quad (29)$$

$$E_{z_{II}} = \sum_{m=0}^{\infty} \frac{j\omega\mu_0 I_0 \varepsilon(m)}{a\gamma \text{Sin}(\gamma b)} \text{Cos} \left( \frac{m\pi x}{a} \right) \text{Cos} \left( \frac{m\pi x_p}{a} \right) \text{Cos}(\gamma y) \text{Cos}(\gamma(y_p-b)) \quad , \quad y \leq y_p \quad (30)$$

The only unknown parameter that has not been dealt with so far is  $\gamma = \gamma_m$ , the single-index propagation constant. It is obtained from using either (26) or (27) for  $G_{\gamma_m}(y, y_p)$  and substituting it into the homogeneous form of (1) :

$$\left[ \frac{\partial^2}{\partial y^2} - \left( \frac{m\pi}{a} \right)^2 + k^2 \right] A_m' \text{Cos}(\gamma y) \text{Cos}(\gamma(y_p-b)) = 0 \quad (31)$$

For non-vanishing cosines ,

$$\gamma = \gamma_m = \sqrt{k^2 - \left( \frac{m\pi}{a} \right)^2} \quad (32)$$

where,  $k^2 = \epsilon_r (1 - \delta_{\text{eff}}) k_0^2$ , as defined in section 2.2.1.

### 2.3.2. Input impedance

Evaluating  $E_z$  from (29) or (30) at the probe coordinate  $(x_p, y_p)$  and substituting into (8), gives

$$Z_{SS} = - \frac{j\omega\mu_0 d}{a} \sum_{m=0}^{\infty} \frac{\epsilon(m) \cos^2\left(\frac{m\pi x_p}{a}\right) \cos(\gamma_m y_p) \cos(\gamma_m(y_p - b))}{\gamma_m \sin(\gamma_m b)} \quad (33)$$

where, "SS" refers to single-sum. Therefore,

$$Z_{mt,SS} = Z_{SS} + X_f \quad (34)$$

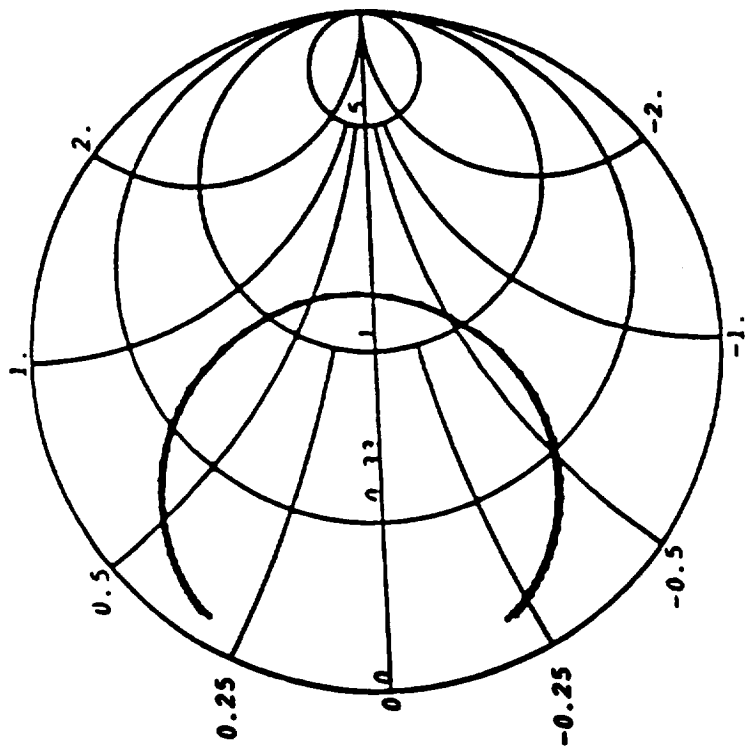
where,  $X_f$  is defined in equation (9).

### 2.4. Comparison of the single-sum and double-sum input impedance expressions

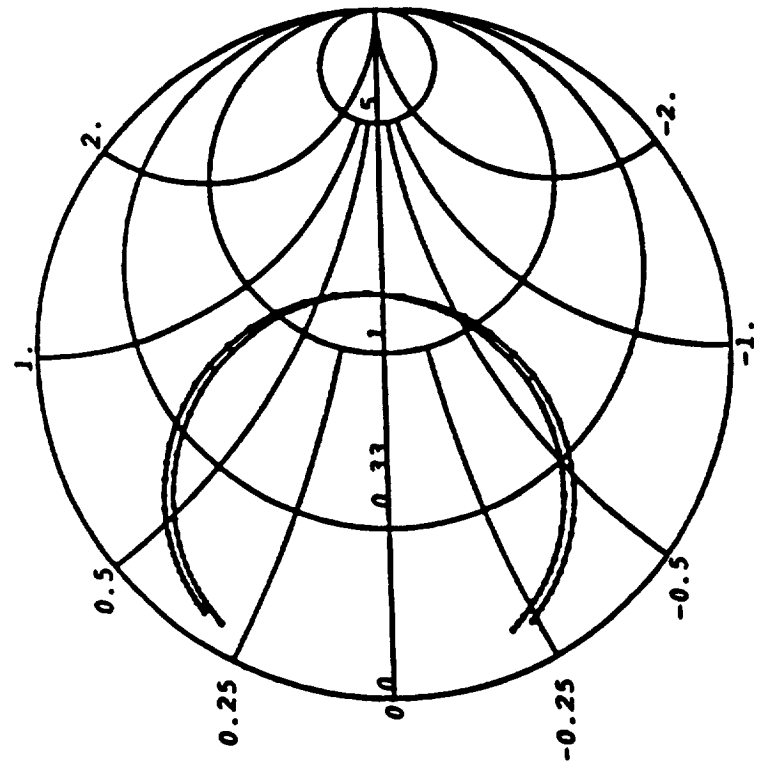
Mathematica 2.2 software was used to calculate all computer data. Sample antenna parameters chosen were  $a = 2"$ ,  $b = 1.27"$ ,  $t = 20$  mils,  $\epsilon_r = 2.33$ ,  $d = 62$  mils, with a resonant frequency of 1.93 GHz. The single sum input impedance for a probe position of  $x = 0.892"$ ,  $y = b / 2"$  was simulated to six terms only, and held fixed in that manner. One of the double sum terms was also held fixed at six terms, and the remaining sum was separately computed by limiting the upper index to 5, 10, and 20 terms, respectively. This was performed to demonstrate the congruency of the single and double sum solutions. Figures 3a-c demonstrate this congruency on computer-generated Smith Charts. It is apparent that as the non-fixed double sum term approaches 20, the two solutions begin to overlap. Therefore, the single sum solution can serve as a replacement to the double sum solution, since it not only represents the double sum solution, but it also is easier to calculate.

Table I is a computation of the execution times associated with the computer simulation of equations (12) and (34), for the antenna mentioned in the first paragraph of this section. The operating frequency

(  $\epsilon_r = 2.33$  ,  $d = 62$  mils )



(a)



(b)

Figure 3 Convergence of Single and Double-Sum Input Impedance Loci

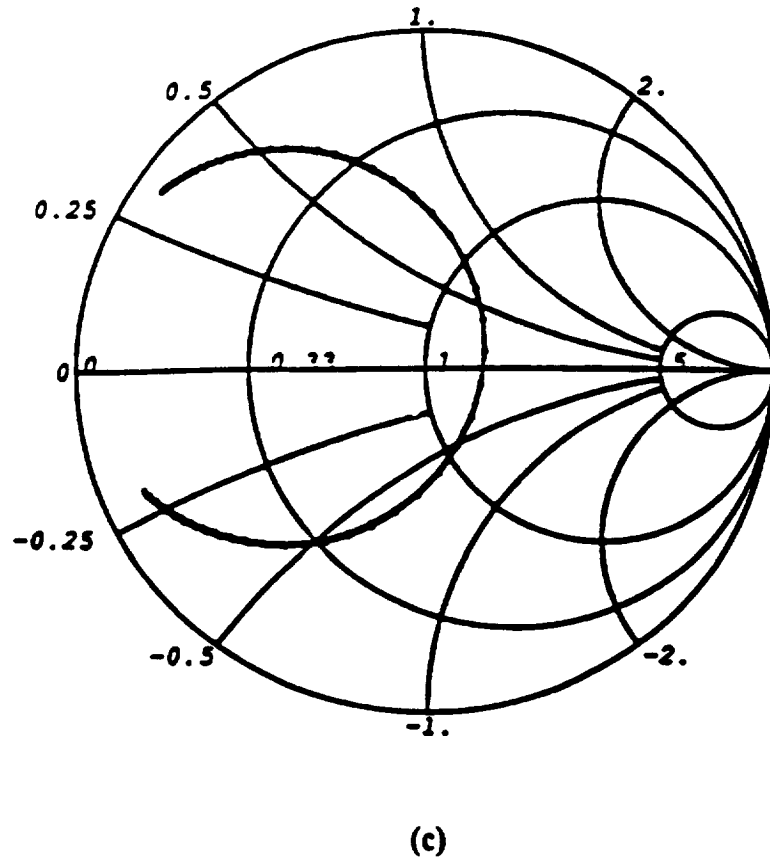


**Figure 3** Convergence of Single and Double-Sum Input Impedance Loci

**Table I - Input Impedance Execution Times for Double and Single Sum Terms**

UPPER SUM LIMIT	EXECUTION TIME (seconds)		INPUT IMPEDANCE ( $\Omega$ )		TIME RATIO
	DS	*SS	DS	*SS	
5	0.49	.22	42.04 + j 20.33	42.04 + j 20.33	2.23
10	1.59	.22	42.04 + j 22.89	42.04 + j 20.33	7.23
20	5.65	.22	42.04 + j 25.32	42.04 + j 20.33	25.70
35	17.03	.22	42.04 + j 27.33	42.04 + j 20.33	77.40
50	33.72	.22	42.04 + j 28.73	42.04 + j 20.33	15300

$\epsilon_r = 2.33, t = .02", d = .062", f = 1.93 \text{ GHz}, \delta = \delta_{\text{eff}} = 1/Q_{\text{TOT}} \approx .01$

- DS - double sum
- SS - single sum
- \* upper sum index held fixed at 5

chosen was 1.93 GHz. A reference to Table I shows that the double sum solutions take from 2 to 153 times as long to execute as compared to the single sum solutions. Again, the single sum solutions are desired for their lower computational times. A graphical display of the congruency of double and single sum solutions is shown in figure 4a. This is further evidence that the two methods provide congruent results. The same simulation procedure mentioned above was performed for a second antenna with  $\epsilon_r = 10.8$ ,  $a = 0.9$ ",  $b = 0.6$ ",  $d = .025$ ", and a probe position of  $x = 0.54$ ",  $y = b / 2$ ", at  $f = 2$  GHz. Results are shown in figure 4b, and are commensurate with those discussed above.

### 3. Experimental verification of the data

A Wiltron 360B Network Analyzer was used to test the rectangular-patch microstrip antenna for input impedance data, with respect to the  $S_{11}$  input port parameter. The Smith Chart frequencies were swept from 1.7 to 2.3 GHz. The test antenna was of patch dimensions  $a = 0.9$ ",  $b = 0.6$ " , with  $\epsilon_r = 10.8$ , and substrate thickness of  $d = .025$ ". The position of the probe was located at  $x = 0.54$ ",  $y = b/2$ " , relative to the bottom left corner (coordinate origin) of the patch. The same antenna dimensions and dielectric constant data were fed into the computer model to generate a Smith Chart. In the theoretical model, an operating frequency of 2 GHz was used, which was the marked frequency on the Network Analyzer.

Figures 5a and 5b are the theoretical and experimental versions, respectively. Usually, the main point of interest on either plot is the point which intersects the real axis, i.e., the point closest to the perfect  $50\Omega$  probe-to-coax line matching point. At 2 GHz, the unnormalized impedances of the input impedances at the probe location were  $(47.961 + j 1.891) \Omega$  and  $(47.842 + j 0.762) \Omega$  for the theoretical and experimental data, respectively, when equation (9) was used to account for an approximation of the probe reactance. However, when equation (9) was omitted from the theoretical model, the theoretical probe impedance was equal to  $(47.961 + j 2.861)$ , which is much better when compared to the experimental value. However, it should be noted that neglecting the probe analysis in theoretical modelling provides reasonably accurate values around the resonant frequency of the antenna, but it also moves the values of the theoretical input

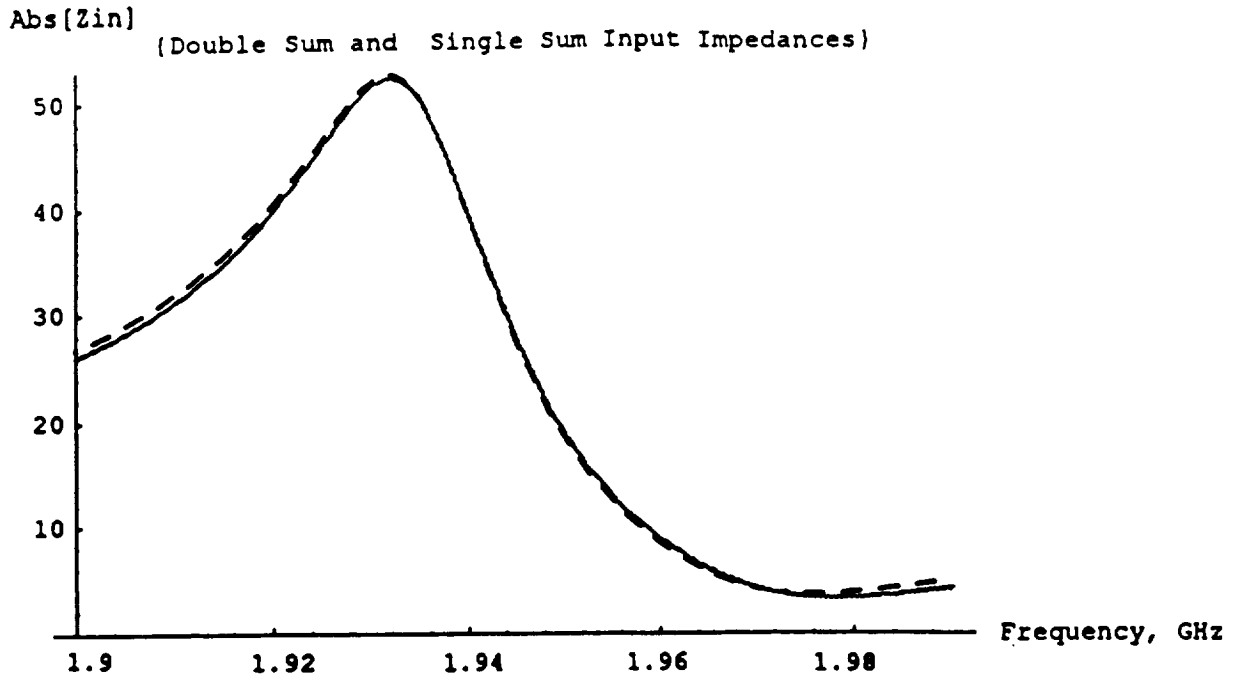


**Figure 4 - Real Part of Double and Single Sum Input Impedances**  
(a) -  $\epsilon_r = 2.33$ ,  $d = .062''$ ,  $a = 2''$ ,  $b = 1.27''$

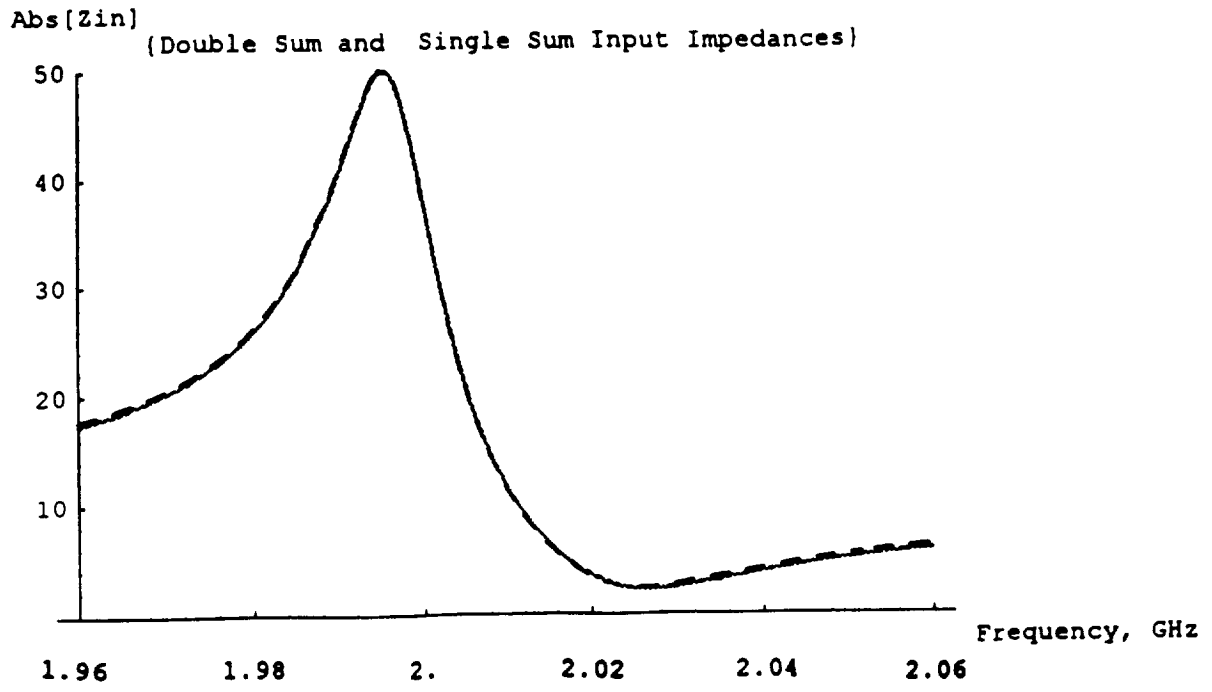


Figure 4 (b) -  $\epsilon_r = 10.8$ ,  $d = .025''$ ,  $a = .9''$ ,  $b = 0.60''$

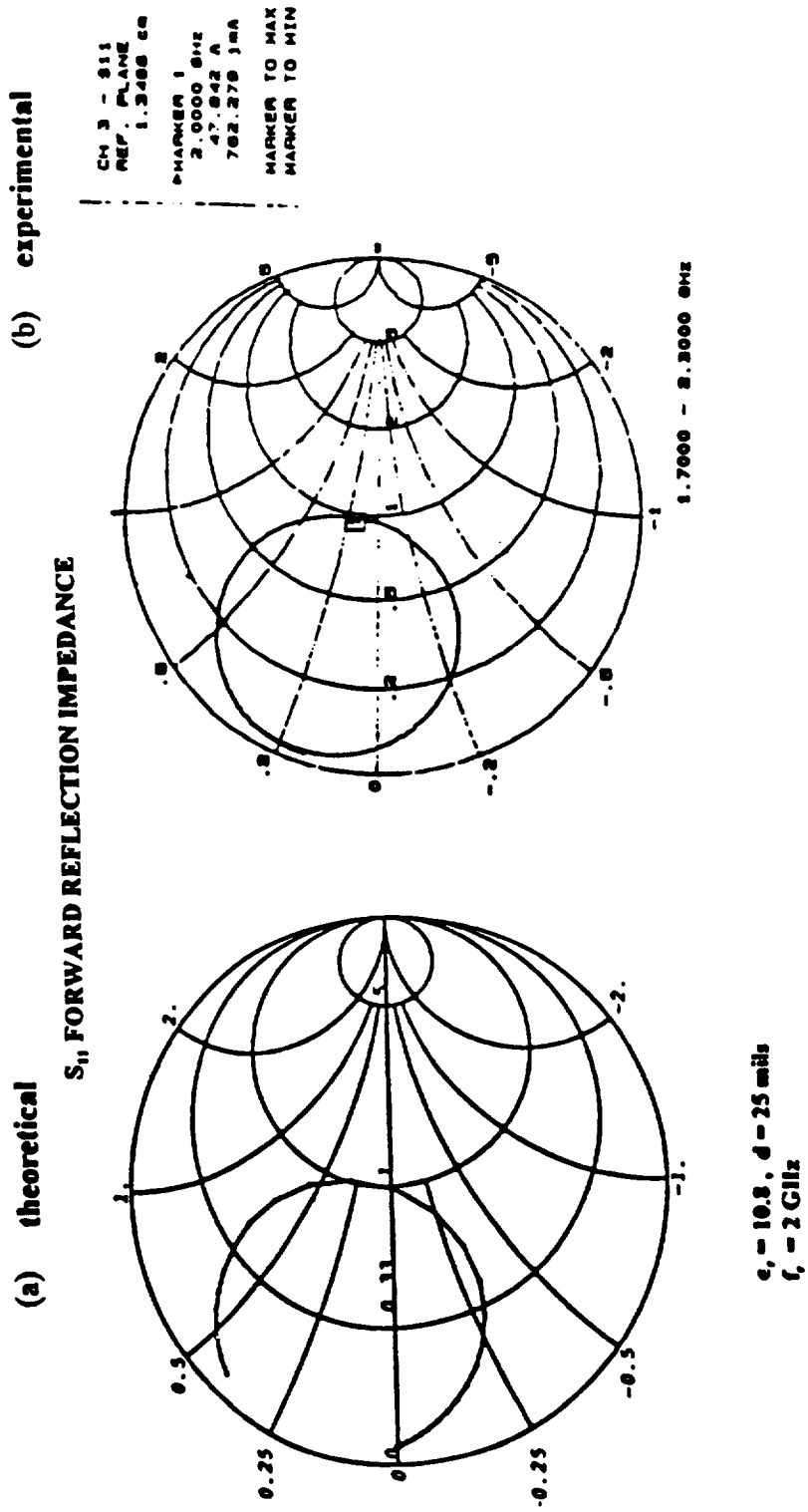


Figure 5 Theoretical Versus Experimental Data for Input Impedance Loci

impedances in a capacitive direction toward the lower half of the Smith Chart when frequencies are further away from the resonant frequency. The error associated with prediction of the imaginary part of the input impedance can be directly attributed to the fact that an approximation was used to forecast the value of the probe reactance. Only testing of the actual antenna provides the exact quantity. However, the use of equation (9) allows one to predict a more accurate value of the antenna input impedance with respect to predicting impedances over an entire given frequency span. The omission of equation (9) from the analysis has been found to cause the Smith Chart impedance data to be shifted downward. This means that the probe has a capacitive effect, which is not the actual case - its effect is an inductive one.

Both Smith Chart curves are quite similar, and the small difference in results can be attributed to the fact that the theoretical model (cavity model) neglects consideration of surface waves and backlobe radiation (under the ground plane) due to reflection caused by an input impedance mismatch. Furthermore, the theoretical analysis views the ground plane as being infinite in transverse (to  $z$ ) directions. However, good results were still obtained, since it has been found (James and Hall 1981) that surface waves are negligible for thin-substrate patch antennas. Since the matching is reasonably close to  $50\Omega$ , reflection is minimal. Therefore, the analysis used was adequate enough to predict the experimental results.

#### **4. Conclusions**

The single-summation approach used to obtain the input impedance was shown to drastically reduce computational effort, when compared to similar double-summation calculations. The real value of this procedural economy is that the reduction in computation and cost does not sacrifice the accuracy needed. Also, it should be emphasized that the double-summation approach required at least twice as much computation as that of the single-summation approach. When the double sum solutions are summed over 50 terms each, it was found that it took 153 times as long to execute as that of an equivalent single summed term.

## ACKNOWLEDGMENTS

This work was supported by NASA Grant No. 5 - 1049. The authors would like to thank Mr. Steven Weiss of the Army Research Lab in Adelphi, Maryland for his permission to use the experimental set up.

## REFERENCES

- Agrawal, P.K., and Bailey, M.C., 1977, An analysis technique for microstrip antennas, *IEEE Transactions on Antennas & Propagation*, **25**, 756-758.
- Alhargan, F. A., and Judah, S.R., 1991, Reduced form of the Green's functions for disks and annular rings. *IEEE Transactions on Microwave Theory & Techniques*, **39**, 601-604.
- Chadha, R. and Gupta, K.C., 1981, Segmentation method using impedance matrices for analysis of planar microwave circuits, *IEEE Transactions on Microwave Theory & Techniques*, **29**, 71-74 .
- Carver, K.R., and Mink, J.W., 1981, Microstrip antenna technology. *IEEE Transactions on Antennas & Propagation*, **29**, 2-24.
- Dereryd, A.G., and Lind, A.G., 1979, Extended analysis of rectangular Microstrip Resonator Antennas. *IEEE Transactions on Antennas & Propagation*, **27**, 846-849.
- Deshpande, M.D., and Bailey, M.C., 1982, Input impedance of microstrip Antennas, *IEEE Transactions on Antennas & Propagation*, **30**, 645-650.
- Felson, L.B. and Marcuvitz, N., 1993, *Radiation and Scattering of Waves* (Englewood Cliffs, N.J. : Prentice-Hall).
- Howell, J.Q., 1975, Microstrip Antennas, *IEEE Transactions on Antennas & Propagation*, **14**, 90-93.
- James, J.R., and Hall, P.S., 1981, *Antenna Theory and Design*. (London : Peter Peregrinus Ltd.).
- Lo, Y.T., Solomon, D., and Richards, W.F., 1979, Theory and experiment on microstrip antennas, *IEEE Transactions on Antennas & Propagation*, **29**, 137-145.
- Lo, Y.T., Harrison, D.D., Solomon, D., Dechamps, G.A., and Ore, F.R., Study of Microstrip Antennas, Microstrip Phased-Arrays and Microstrip Feed Networks. Electromagnetics Laboratory, Univ. of Illinois, Urbana, Contract AF19628-76-C-140, RADC-TR-77-406, pp. 1-27, December, 1977.

Pozar, D.M., 1982, Input impedance and mutual coupling of rectangular microstrip antennas, *IEEE Transactions on Antennas & Propagation*, **29**, 1191-1196.

Richards, W.F., Lo, Y.T., and Harrison, D.D. , 1981, An improved theory for microstrip antennas and applications, *IEEE Transactions on Antennas & Propagation*, **29**, 38-46.

Watkins, J., 1973, Radiation loss from open-circuited dielectric resonators, *IEEE Transactions on Microwave Theory & Techniques*, **21**, 636-639.

- Figure 1** Basic Rectangular Patch Microstrip Structure
- Figure 2** Two-Region, Single-Sum Patch
- Figure 3** Convergence of Single and Double-Sum Input Impedance Loci  
( $\epsilon_r = 2.33$ ,  $d = 62$  mils)
- Figure 4** Real Part of Double and Single Sum Input Impedances  
(a)  $\epsilon_r = 2.33$ ,  $d = .062$ ",  $a = 2$ ,  $b = 1.27$ "  
(b)  $\epsilon_r = 10.8$ ,  $d = .025$ ",  $a = .9$ ",  $b = 0.60$ "
- Figure 5** Theoretical Versus Experimental Data for Input Impedance Loci  
 $S_{11}$  Forward Reflection Impedance - ( $\epsilon_r = 10.8$ ,  $d = 25$  mils,  $f = 2$  GHz)  
(a) theoretical  
(b) experimental



## **COUPLING SINGLE-MODE FIBER TO UNIFORM AND SYMMETRICALLY TAPERED THIN-FILM WAVEGUIDE STRUCTURES USING GADOLINIUM GALLIUM GARNET**

Jagannath Gadi, Raj Yalamanchili and Mohammad Shahid  
Howard University  
Department of Electrical Engineering  
2300, 6 th Street, N.W  
Washington, DC 20059

### **Abstract**

The need for high efficiency components has grown significantly due to the expanding role of fiber optic communications for various applications. Integrated optics is in a state of metamorphosis and there are many problems awaiting solutions. One of the main problems being the lack of a simple and efficient method of coupling single-mode fibers to thin-film devices for integrated optics. In this paper, optical coupling between a single-mode fiber and a uniform and tapered thin-film waveguide is theoretically modeled and analyzed. A novel tapered structure presented in this paper is shown to produce perfect match for power transfer.

### **1. INTRODUCTION**

Integrated Optics has come a long way since early 1970's. It is poised at the threshold of making a big impact in everyday world. Integrated optics has drawn into several disciplines, such as computers and microwave integrated circuit technology resulting in new fabrication technologies. The field is now in a state of flux and there are still many problems awaiting solutions. One of the main problems being the lack of a simple and efficient method of coupling optical fiber to thin-film devices for integrated optics. Although a number of connectors are available in the market, the efficiency and reproducibility are low. In this paper, a novel uniform and symmetrically tapered structure are analyzed mathematically and the results presented.

There are certain papers published by researchers in the area of thin-film couplers that are worthy of note, in that they provide the background for the development of the proposed work and point towards issues raised by shortcomings of the previous work. Louisell [1] investigated broadband bi-directional couplers in which he showed that the phase constants and coupling coefficients vary with distance along two coupled transmission lines. Ulrich [2] has shown by analysis how light can be coupled into a thin-film by means of a prism-film coupler. Akira Ihaya [3] presented a mathematical model of a thin-film optical directional coupler consisting of a three-layered deposited glass films on the substrate, with coupling occurring between the first and the third film. Wilson and Teh[4] have shown a mathematical modeling of a tapered velocity directional coupler. Nelson [5] has theoretically

examined the coupling of single-mode optical waveguides through the use of expanding and contracting tapers. Juichi Noda et al.[6] have shown a connection between single mode fiber coupler to a Ti diffused LiNO<sub>3</sub> strip waveguide. The authors Y.Cai et al.[7]., have analyzed the coupling characteristics of a uniform structure.

## 2. THEORETICAL BACKGROUND

In this paper, we present a novel method of coupling light from a single mode fiber to two structures : Uniform and symmetrically tapered thin-film couplers. The model presented is an improved version of the uniform five layered structure presented by Y. Cai et al [7]. If a fiber is directly connected to the thin-film, as shown by Y.Cai et al [7]., it leads to a large mismatch of the field profiles at the interface and as a result, leads to loss of optical power. To overcome this optical reflection and radiation losses, they proposed a five layered structure which is shown in Figure 1. This consists of a coupling waveguide, buffer layers, thin-film layer and the substrate. To avoid mismatch of the fiber core and the coupling waveguide field profiles at the interface, the coupling waveguide dimensions are designed as 2aX2a, where 'a' is the radius of the fiber core. Guttmann et al[8]., have shown that the field distributions of the fundamental mode of the cylindrical fiber core and the garnet material waveguide differ slightly if the refractive index differences are smaller. Solgel solution is used at the interface such that any slight refractive index mismatch between the fiber core and the coupling waveguide is minimized. The buffer layer serves the purpose of coupling optical power to the thin-film waveguide of lower refractive index. Gadolinium Gallium Garnet material was used as the thin-film material because of the properties exhibited by the material. The buffer layers and the coupling waveguide are silica doped materials. The required refractive index of buffer and coupling waveguides is obtained by doping TiO<sub>2</sub> with SiO<sub>2</sub>.

The eigen mode equations of the five layered structure developed ( Figure 1 ) can be obtained by solving with  $w=g=2a$ , where :  $w$ = the height of the coupling waveguide,  $a$ = radius of the fiber core,  $n_{gg}$ =refractive index of the coupling waveguide ( Garnet material ),  $n_a$ =refractive index of the buffer layer,  $n_w$  = refractive index of the thin-film material,  $\lambda$ =wavelength of the wave ( 1.3 $\mu$ m ) and  $W$ = height of the thin-film coupling waveguide. The eigenmode equations developed by Y.Cai et al[9].,are :

$$Q_a = n_a^2 K_{gx} \tan(K_{gx} \cdot W / 2) \quad \text{----- ( 1 )}$$

$$Q_a = \sqrt{(2\pi / \lambda)^2 (n_{gg}^2 - n_a^2) - K_{gx}^2} \quad \text{----- ( 2 )}$$

$$Q_t = \frac{K_{gy} \{-1 + \sqrt{\tan^2(g \cdot K_{gy}) + 1}\}}{\tan(g K_{gy})} \quad \text{----- ( 3 )}$$

$$Q_t = \sqrt{(2\pi / \lambda)^2 (n_w^2 - n_a^2) - K_{gy}^2} \quad \text{----- ( 4 )}$$

The parameters  $k_{gx}$ ,  $Q_a$  and  $k_{gy}$ ,  $Q_t$  are the x and y components of the wavenumbers.  $K_{gx}$  and  $K_{gy}$  represent the sinusoidal variation in the x and y directions. The propagation constant of the coupling waveguide can be determined by solving equations ( 1 to 4 ).

$$\beta_{gg}^2 = \omega^2 \mu_o \epsilon_o n_{gg}^2 - K_{gx}^2 - K_{gy}^2 \quad \text{----- ( 5 )}$$

The propagation constant  $\beta_w$  of the thin-film waveguide is obtained by replacing  $n_{gg}$  with  $n_w$ ,  $w$  with  $W1$  and  $\beta_{gg}$  with  $\beta_w$  in equations( 1to5 ). The value of  $W1$  for the thin-film is so chosen such that highest power coupling occurs between the coupling waveguide and the thin-film at this value. The optimum value  $W1$  is chosen such that  $\beta_{gg} = \beta_w$  for no mismatch. The thickness of the buffer layer has a direct bearing on the power coupled from the coupling waveguide to the thin-film waveguide and an optimum value is chosen such that there is a maximum power transfer from the coupling waveguide to the thin-film waveguide. The propagation constant of the thin-film varies because of the change in value of  $w$  along the  $z$  direction. Therefore the mismatch,  $M$  depends

$$\text{on the propagation constant difference given by } M(z) = \frac{\beta_{gg} - \beta_w(z)}{2C} \quad \text{----- ( 6 )}$$

and the maximum fraction of power transferred between the coupling waveguide and the thin-film waveguide with a fixed mismatch  $M$ , is given by  $F^2 = (1 + M^2)^{-1}$  ----- ( 7 )

Application of the theory developed by Snyder et al[10] and Snyder [11], to the model analyzed in Figure 1, gives the power coupled into the thin-film for a uniform coupler as

$$P' = P F^2 \text{Sin}^2 \int_0^z (C / F) dz \quad \text{----- ( 8 )}$$

where  $P$  is the total power introduced,  $C$  the coupling coefficient between the center of the coupling waveguide and the center of the thin-film waveguide. In this paper, we present a novel uniform and symmetrically tapered structure ( Figure 2 ) where the modes of a uniform waveguide form a complete set and can propagate independently from one another, while the tapered modes are coupled together and adjust their characteristics to suit the varying transverse properties of the guiding structure as they are moving along the taper. During the process of coupling the light from the uniform coupling waveguide to the thin-film waveguide, the wave is kept in the lowest order mode. For the shape shown in this paper,( Winn and Harris [12]),the power coupled at the

$$\text{narrow end is given by } P_o = P' ( 1 - F^2 \text{Sin}^2 \int_0^z (C / F) dz ) \quad \text{----- ( 9 )}$$

In this paper while analyzing the theoretical model of the uniform and tapered coupler we made the assumption that the materials used are lossless and therefore there are no Fresnel's reflections at the interfaces and that there are no lossess at the interface of the fiber core and the coupling waveguide.

### 3. RESULTS AND DISCUSSION

The material used for the analysis of uniform and tapered couplers is Gadolinium Gallium Garnet (GGG). The coupling waveguide material used is GGG. Buffer layer material is spun silica which is doped with TiO<sub>2</sub>. Thin-film material is polymerized solgel solution of SiO<sub>2</sub> and TiO<sub>2</sub>. The refractive index of coupling waveguide,  $n_{gg} = 1.9389$  @  $\lambda = 1.3\mu\text{m}$ . The refractive index of the buffer layers is chosen, as  $n_a = 1.9340$  and the refractive index of the thin-film material,  $n_w = 1.9450$ . Figure 3 shows the plot of C versus d, where C is the coupling coefficient and d is the distance from the center of the coupling waveguide to the center of the thin-film. This equation given by Snyder [11], is

$$C = \left(\frac{V\Delta}{2\pi}\right)^{1/2} \frac{d}{\rho^2} \exp\left\{\frac{-Vd^2}{4\rho^2}\right\} \quad \text{---- (10)}$$

The refractive index of GGG versus wavelength is shown in Figure 4. The expression used to calculate the refractive index is  $n^2 - 1 = \sum_{i=1}^3 \frac{A_i \lambda^2}{(\lambda^2 - L_i^2)}$  ---- (11)

where  $A_i$  and  $L_i$  are the sellmeier coefficients, given by Wood and Nassau [13].

By solving the equations (1to5) with  $w=2a=g$ , the propagation constant  $\beta_{gg} = 9.3253804 \mu\text{m}^{-1}$  was obtained.

Figure 5 shows the propagation constant for the thin-film as a function of the film thickness  $W1$ . The propagation constant of the thin-film equals the propagation constant of the coupling waveguide when the thickness  $W1=0.886\mu\text{m}$ . The maximum coupling power is attained at  $\beta_{gg} = \beta_w = 9.3253804 \mu\text{m}^{-1}$ . Figure 6 shows the plot of coupled power versus the propagation distance for the uniform coupler of different d's for perfectly matching constants  $\beta_{gg} = \beta_w$  at thickness of thin-film  $w=0.886 \mu\text{m}$ . Figure 7 shows the power coupled for uniform and tapered couplers with respect to the distance z and the taper starts at length  $L1= 700\mu\text{m}$ , with slopes (K) of the symmetrical taper at 0.0001, 0.00009 and 0.00002. Figure 8 shows the effect of the thickness of the thin-film and the role played by the taper in the power output.

### 4. CONCLUSION

The novel structure (Figure 2) exhibits broad-bandwidth coupling characteristics and it is easy to manufacture since it does not put serious constraints on the accuracy of the coupling length of the coupler. The taper has the distinctive advantage of confining the power within the taper such that the output stays approximately near the value of the power introduced at the start of the taper. The outstanding feature of the taper is the higher efficiency as compared to the more conventional devices.

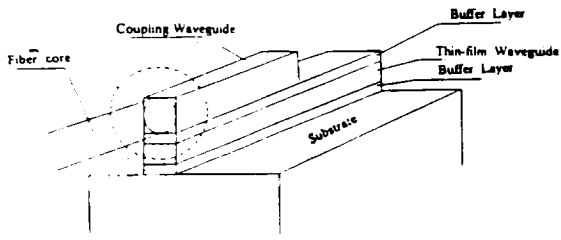


Figure 1. Schematic diagram of Single-mode fiber to thin-film waveguide using a coupling waveguide

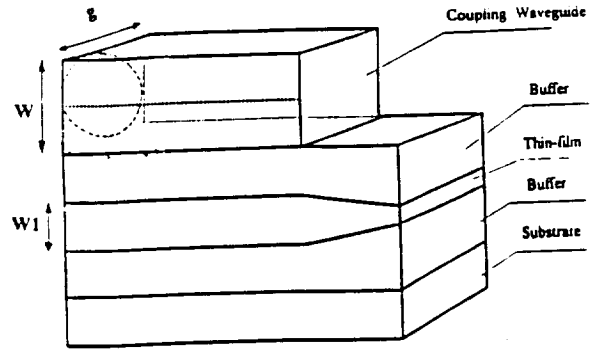


Figure 2. Schematic diagram of the proposed novel tapered structure.

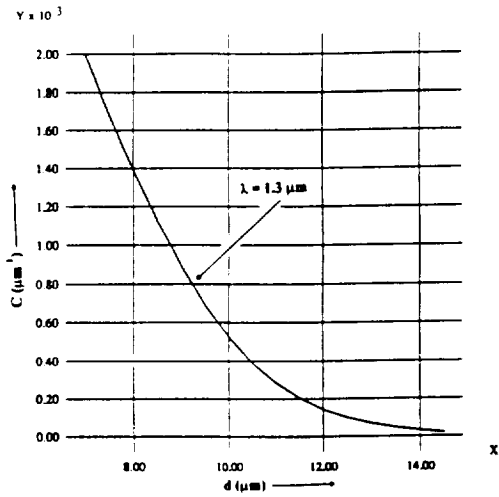


Figure 3. Coupling coefficient versus separation distance between center of coupling waveguide to center of thin-film waveguide.

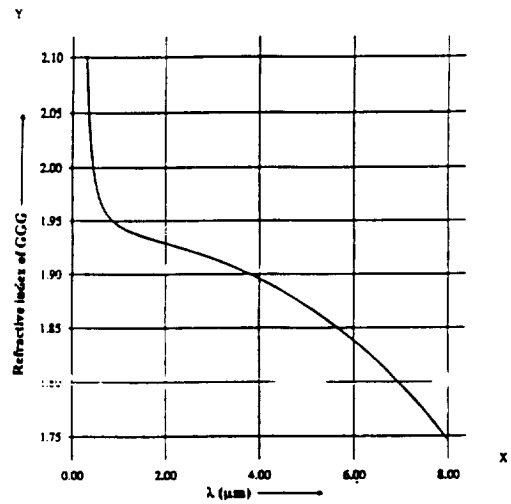


Figure 4. Refractive index of gallium garnet as a function of wavelength.

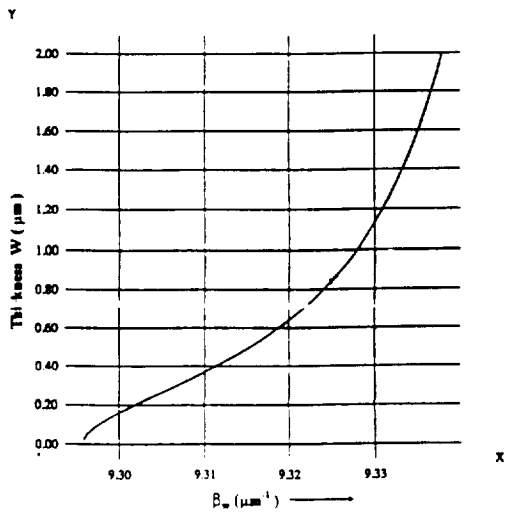


Figure 5. Propagation constants versus thickness of thin-film.

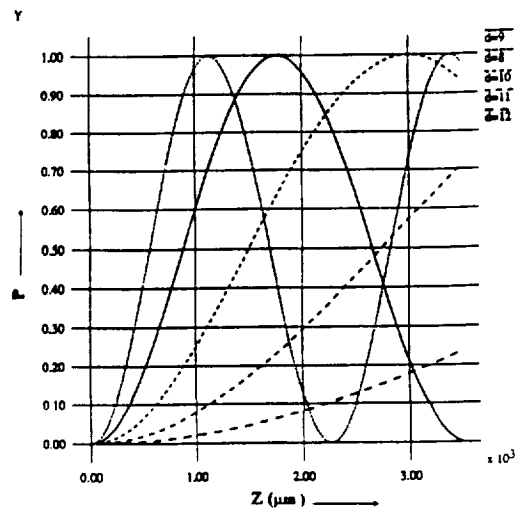


Figure 6. Plot of power coupled into thin-film versus length for various values of d.

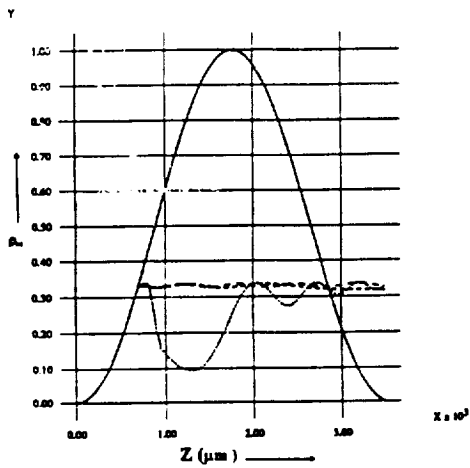


Figure 7. Comparison of uniform power and tapered power coupled into thin-film with taper at  $L_1=700 \mu\text{m}$  for different cases of  $K$  for a thin-film thickness of  $W_1=0.886 \mu\text{m}$ .

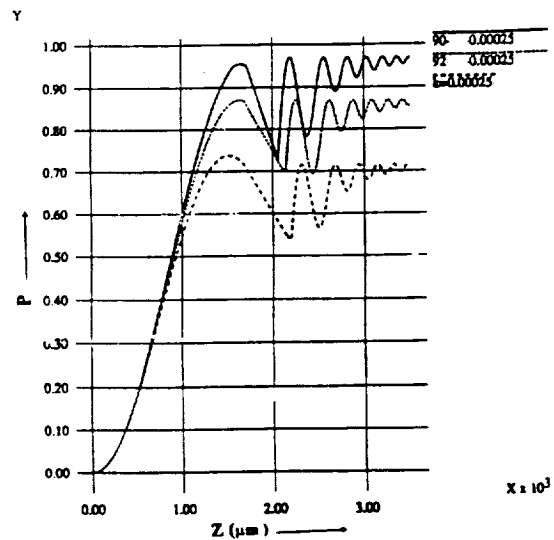


Figure 8. Plot of coupled power versus propagation distance for a taper structure with  $L_1=1700 \mu\text{m}$  and a slope  $K=0.00025$  for different thickness of thin-film.

## 5. REFERENCES

- [1]. W.H.Louisell, " Analysis of the single tapered mode coupler," The Bell system Technical Journal, pp 853-870, July 1955.
- [2]. R.Ulrich, " Theory of the prism-film coupler by plane-wave analysis", Journal of the Optical Society of America, Vol.60, No.10, pp 1337 - 1350, October 1970.
- [3]. Akira Ihaya, Hirosuka Furuta, Hideki Noda, " Thin-film optical directional coupler, " Proceedings of the IEEE, pp 470-471, April 1972.
- [4]. Michael G.F.Wilson and G.A. Teh, " Tapered optical directional coupler," IEEE transactions on microwave theory and Techniques, Vol. MTT-23, No.1, pp 85-92, January 1975.
- [5]. A.R. Nelson, " Coupling Optical Waveguides by tapers", Applied Optics, Vol.14, No 12, December 1975.
- [6]. Juichi Noda, Osamu Mikami, Makoto Minaketa, and Masaharu Fukuma, " Single-mode optical-waveguide fiber coupler," Applied optics, Vol.17, No.13, pp 2092-2096, July 1978.
- [7]. Yuanmin Cai, Tetsuya Mizumoto, and Yoshiyuki Naito, " An Effective method for coupling Single-mode fiber to Thin-film Waveguide," Vol.9, No.5, May 1991.
- [8]. J.Guttman, O.Krumpholz and E. Pfeiffer, " Optical Fiber-Stripline-Coupler", Applied Optics, Vol.14, No.5, pp 1225-1227, May 1975.
- [9]. Yuanmin Cai, Tetsuya Mizumoto, and Yoshiyuki Naito, " Analysis of the coupling waveguide system," Journal of Lightwave technology, Vol.8, No.1, pp 90 - 98, January 1990.
- [10]. A.W.Snyder and A. Ankiewicz, " Fiber couplers composed of unequal cores," Electronics letters, Vol.22, No.23, pp 1237-1238, November 1986.
- [11]. Snyder and Love, " Optical Waveguide Theory", Chapman, New York, 1988.
- [12]. Robert K. Winn and Jay H. Harris, " Coupling from multimode to single-mode linear waveguides using Horn-shaped structures," IEEE Transactions on Microwave Theory and Techniques, Vol. MTT-23, No.1, January 1975.
- [13]. Darwin L.Wood and Kurt Nassau, " Optical properties of Gadolinium Gallium Garnet", Applied Optics, Vol. 29, No.5, September 1990.

## **VI. Copy of Technical Paper Presented in Brazil**





